A Dynamical Study of Jupiter's Great Red Spot

Thesis by

Timothy Edward Dowling

In Partial Fulfillment of the Requirements
for the Degree of
Doctor of Philosophy

California Institute of Technology
Pasadena, California

1989

(submitted November 10, 1988)

To my parents, Edward and Rita

Acknowledgements

I was introduced to this project by my thesis advisor, Professor Andrew Ingersoll. I have been very fortunate to be able to work with Professor Ingersoll, whose name is synonymous with the study of Jovian dynamics. I appreciate the true sense of collaboration he instilled in our relationship, and I look forward to a continued, vigorous collaboration in the years to come.

I'm lucky to have had two excellent advisors while at Caltech, the second being my academic advisor Professor Duane Muhleman. I especially thank Professor Muhleman for the opportunity of studying the fascinating Saturnian system, using Caltech's state-of-the-art millimeter radio telescope at Owen's Valley.

I owe a great deal to my fellow graduate students. I thank Don Rudy, Jim Friedson, Randy Kirk, and Dan Wenkert for many stimulating discussions. I thank Carol Polanskey for helping me recover from a broken leg suffered late in the game, for helping with the thesis typesetting programs (Tex macros) developed by Don R. and Randy K., and for being a good friend. I also thank Arie Grossman, Dave Crisp, and Jeff Hester for many discussions, and for building and holding together the department's computer facilities. I thank fellow Ingersoll-student Richard Achterberg for stimulating discussions on Jovian dynamics, and for helping me cope with our ever-expanding computer system. I thank all the friends I've made at Caltech for helping me stay sane during my tenure here. Finally, I extend special thanks to the department's secretaries Kay, Donna, Lorna, and Rachel for their tireless assistance.

Preface

We are currently halfway between the highly successful encounters with Jupiter by the Voyager spacecraft in 1979, and the exciting Galileo orbiter-and-descent-probe mission planned for the 1990's. The beautiful and dynamic cloud patterns revealed in Jupiter's atmosphere by the Voyager cameras have allowed us to obtain high-resolution velocity data for the cloud-top level, yielding flow visualization that is the envy of any earth oceanographer. Unlike the case of the earth's oceans and atmosphere, however, we have not yet penetrated below the obscuring cloud tops to observe directly the dynamics of the deep atmosphere. Recent high-resolution observations of Jupiter at radio wavelengths, which are sensitive to the atmosphere at depth, are exciting, but ambiguities between the competing effects of variable thermal fields and variable opacities make remote sensing techniques difficult. A new, indirect approach to probing the deep atmosphere has lately emerged, based on interpreting the signatures of deep-atmospheric dynamics as expressed in the cloud tops. Examples include work on observed mesoscale waves, which may propagate upward from the deep atmosphere, features in the stratosphere that are apparently stationary with respect to the magnetic field, and hence the deep atmosphere, and the present work on the signature of deep motions in the Jovian vortices. Indirect techniques, as well as theoretical modeling, will continue to provide us with much of our understanding of the deep atmospheres of Jovian planets, until we can send in probes beneath the cloud tops.

Table of Contents

Table of Figures

List of Tables

Abstract

This work is presented in the form of two related papers. In the first paper we investigate layer thickness variations in Jupiter's atmosphere by tracking absolute vorticity ($\zeta + f$) along streamlines of the Great Red Spot (GRS) and White Oval BC. The ratio of absolute vorticity to layer thickness, called the potential vorticity, is conserved following the motion. By observing Lagrangian variations of absolute vorticity, we may infer variations in layer thickness. The data thus obtained are a useful diagnostic that will help differentiate between models of Jovian vortices. We interpret the observed layer thickness variations using a simple "1-1/2" layer model in which a thin upper weather layer, which contains the vortices, overlies a much deeper layer, which is meant to model the deep atmosphere. In this model, layer thickness variations are directly coupled to motions in the deep atmosphere, and we use the data to infer the deep motions. In the first paper we interpret the data, using the quasi-geostrophic equations. In the second paper we reinterpret the data, using the more general shallow water equations. Most current models of the GRS are cast in terms of the 1-1/2 layer model, and they start by prescribing the motions in the deep atmosphere. Here we are able to *derive* the deep motions using the same 1-1/2 layer model assumptions, up to a constant that depends on the unknown static stability of Jupiter's troposphere. None of the current prescriptions for the deep motions are in qualitative agreement with the observations over the full range of latitudes observed. We study the 1-1/2 layer model numerically, using both the derived deep motions and the prescribed deep motions of current models. Only the present model, based on observations, yields Lagrangian absolute vorticity profiles that agree with those obtained in the first paper. A model run that starts with the observed zonally averaged cloud-top winds and derived deep motions shows instability, which naturally leads to the genesis and maintenance of a large, isolated vortex similar to the GRS.

Paper 1

Potential Vorticity and Layer Thickness Variations

In regard to the depth of the water, I could not see how this could have been ascertained at all in the immediate vicinity of the vortex.

—Edgar Allan Poe, *A Descent into the Maelström*

Potential Vorticity and Layer Thickness Variations in the Flow around Jupiter's Great Red Spot and White Oval BC

Timothy E. Dowling and Andrew P. Ingersoll

Division of Geological and Planetary Sciences

California Institute of Technology

Pasadena, California 91125

Published in the *Journal of the Atmospheric Sciences*

April 15, 1988

Contribution number 4460 from the Division of Geological and Planetary Sciences, California Institute of Technology, Pasadena, California 91125.

Abstract

Layer thickness variations in Jupiter's atmosphere are investigated by treating potential vorticity as a conserved tracer. Starting with the horizontal velocity field measured from *Voyager* images, fluid trajectories around the Great Red Spot (GRS) and White Oval BC are calculated. The flow is assumed to be frictionless, adiabatic, hydrostatic, and steady in the reference frame of the vortex. Absolute vorticity is followed along each trajectory; its magnitude is assumed to vary directly as the thickness, which is defined as the mass-per-unit area between potential temperature surfaces. To the accuracy of the observations, the inferred thickness is a separable function of trajectory and latitude. The latitude dependence has positive curvature near the GRS and the Oval BC. The relative variations of thickness with respect to latitude are generally larger than the relative variations of the Coriolis parameter with respect to latitude — the beta effect. The data are a useful diagnostic that will help differentiate between models of Jovian vortices. The present analysis employs a quasi-geostrophic model in which a thin upper weather layer, which contains the vortex, is supported hydrostatically by a much deeper lower layer. In this model, the upper free surface does not contribute to the observed variation of thickness along trajectories. Such variations are due exclusively to bottom topography — flow of the deep lower layer relative to the vortex. The observations are used to infer the form of the deep zonal velocity profile vs. latitude. The magnitude of the profile depends on the unknown static stability. The principal result is the existence of horizontal shear in the deep-layer, zonal velocity profile; i.e., the lower layer is not in solid-body rotation and does not act like a flat solid surface. In this respect the data support the hypothesis of Ingersoll and Cuong (1981) concerning motions in the deep layer. However, at some latitudes the data violate Ingersoll and Cuong's criterion governing the compactness of the vortices. At these latitudes the topography allows standing Rossby waves (wakes) extending far downstream to the west. Observed wavelike features, the filamentary regions, are possibly formed by this mechanism.

1.1 Introduction

The effect of vertical structure on large-scale atmospheric flows is summarized by the principle of conservation of potential vorticity. For adiabatic, hydrostatic, frictionless flow in a stably stratified fluid, the important vertical variable is the thickness (actually the mass-per-unit area) of a layer bounded above and below by surfaces of constant potential temperature. The principle states that as a fluid parcel moves within such a layer, the ratio between the parcel's absolute vorticity and its thickness remains constant. On Jupiter, absolute vorticity is calculated directly from the horizontal wind field, which is measured by tracking clouds in *Voyager* images. The trajectories of fluid parcels are also calculated from the wind field. Therefore, by following the changes of absolute vorticity along the fluid trajectories, one can measure the shape of potential temperature surfaces in Jupiter's atmosphere.

We define potential vorticity as $(\zeta + f)/H$. Here, ζ is $\hat{\mathrm{k}} \cdot \nabla \times \mathrm{v}$, the vertical component of relative vorticity; f is planetary vorticity $2\Omega \sin\lambda$, where Ω is the planet's angular speed of rotation ($2\pi/\Omega = 9^{\mathrm{h}}55^{\mathrm{m}}29.7^{\mathrm{s}}$) and λ is planetographic latitude; H is $-\partial P/\partial\theta$, the pressure thickness ΔP per unit change in potential temperature $\Delta\theta$. This is a special form of Ertel's (1942) potential vorticity. For large-scale (hydrostatic), adiabatic, frictionless flow, it is a constant following the fluid motion (e.g., Holton, 1979; Pedlosky, 1987; Haltiner and Williams, 1980). By plotting the absolute vorticity $(\zeta + f)$ as it changes along a trajectory, one can observe the relative changes of H. By observing such profiles, we gain a detailed diagnostic that will help to differentiate between current models of Jovian vortices.

Absolute values of H cannot be determined without additional information, e.g., a measurement of temperature vs. pressure at some point along the trajectory. For Jupiter, a direct measurement of $-\partial P/\partial\theta$ is difficult. The relevant levels are hidden in the clouds, whose tops are at 0.5 to 1.0 bar, and whose bottoms are perhaps at 3

to 5 bars (e.g., Ingersoll *et al.*, 1984). Moreover, the departures of the profiles from an adiabat ($-\partial\theta/\partial P = 0$) are likely to be small. Direct estimates of $-\partial P/\partial\theta$ are sensitive to the assumed composition, rates of conversion between ortho and para hydrogen, and to errors of observation. With data now in hand, potential vorticity provides perhaps the best method of gathering information about $-\partial P/\partial\theta$ at altitudes within the clouds.

The most interesting regions are those where meridional motion is occurring, since f will then vary along the trajectories. Examples include the flow around the Great Red Spot (GRS) and the three white ovals. Both the GRS and the White Oval BC were studied during the *Voyager* encounters by Mitchell *et al.* (1981). They determined radial profiles of wind speed and vorticity on a set of concentric ellipses. Winds of order 110 to 120 m/s were found at the outer edges of both the GRS and the Oval BC. However, Mitchell *et al.*. did not determine fluid trajectories, and did not discuss the variations of tangential velocity and vorticity around the circumferences.

We have expanded on the analysis of Mitchell *et al.* in several ways. First, we infer fluid trajectories directly from the data, without assuming that the trajectories are elliptical or closed. Second, we have combined *Voyager 1* and *Voyager 2* data, and have included data taken when the spacecraft were farther from Jupiter in order to study a larger region around the GRS. Third, we have organized our data so as to bring out the variations of $(\zeta + f)$ along each trajectory.

There have been other quantitative studies of meridional motion on Jupiter. Hatzes *et al.* (1981) studied the divergence, vorticity, and oscillatory behavior of brown barges. The barges are cyclonic and are exceptions to the rule that all long–lived, compact oval spots like the GRS and the Oval BC are anticyclonic (high-pressure) regions. Mac Low and Ingersoll (1986) studied over 100 spots involved in mergings and other interactions, for spot sizes (major diameters) ranging from 500 to 7000

km. Several groups (Beebe *et al.*, 1980; Ingersoll *et al.*, 1981; Limaye *et al.*, 1982; Sromovsky *et al.*, 1982) have measured the eddy stress term $\overline{u'v'}$ and its relation to the ambient shear $d\overline{u}/dy$. These papers are discussed by Ingersoll *et al.* (1984) in their review of the dynamics of the atmospheres of Jupiter and Saturn.

The present paper is organized as follows: Section 1.2 describes the data set. Section 1.3 gives the method of data analysis — how to extract information from a set of over 2000 velocity vectors measured at irregular locations with respect to latitude and longitude. Section 1.4 describes tests that were made to evaluate the uncertainty of our results. Section 1.5 presents a test of the physical model, based on the fact that the trajectories are closed to a good approximation. Section 1.6 gives the results of the data analysis. Finally, Sections 1.7 and 1.8 discuss implications in the context of a quasi–geostrophic model similar to that of Ingersoll and Cuong (1981), in which variations of thickness along the trajectories arise from a deep zonal flow in the adiabatic layer beneath the clouds.

1.2 Data Set

The data set for the GRS consists of over 2000 velocity vectors from the *Voyager 1* and *Voyager 2* encounters. The data set for the Oval BC is just over 400 vectors from the *Voyager 1* encounter. Each vector is computed from the displacement of a feature that is visible in a pair of images separated in time. A human operator locates the feature; the program AMOS then computes the zonal and meridional velocities, taking into account the oblate spheroidal shape of the planet and the spacecraft viewing geometry (Yagi *et al.*, 1978). The error that is due to feature location is scene-dependent. In the best cases when the features are sharp and well defined, the error is about 2 pixels. The error that is due to viewing geometry (camera pointing

uncertainty) is about 2 pixels in all cases, and is the same for all points in an image (Ingersoll *et al.*, 1981).

The GRS data were derived from 10 image pairs separated in time by 10 hours and one image pair separated by 20 hours. The resolution ranged from 20 to 40 km/pixel. Most of the Oval BC data (330 out of 429 vectors) come from a single pair separated by 1.4 hours at a resolution of 10 km/pixel. The other Oval BC data come from pairs separated by 10 hours. In the best cases, the measurement error for velocity (4 pixels divided by the time interval) is 2 to 4 m/s for the GRS and 8 m/s for the Oval BC. We excluded several *Voyager 1* pairs of the GRS taken 0.5 hour apart, since these have best-case errors of order 25 m/s. For comparison, peak velocities around the GRS and the Oval BC are over 100 m/s.

Each velocity vector is assigned a latitude and longitude from the averages of the latitudes and longitudes in the two images. We define planetographic latitude λ as the angle between the local vertical and its projection onto the equatorial plane, with equatorial and polar radii R_e and R_p of 71400 and 66773 km, respectively. Planetocentric latitude λ_c is related to λ by the equation $\tan\lambda = \epsilon^2 \tan\lambda_c$, where $\epsilon = R_e/R_p$. We use longitude ϕ, defined relative to the System III coordinate system rotating with the magnetic field of Jupiter.

Figure 1.1 is a *Voyager 2* image of the GRS (FDS 20517.32). The image is labeled with planetographic latitude and System III longitude (the actual projection is a Cartesian coordinate system with planetocentric latitude and longitude in equal increments along the two axes). *Voyager 1* images of the GRS and the Oval BC are shown in Mitchell *et al.* (1981). Figure 1.2 shows the measured velocities from *Voyager 1* and *Voyager 2* presented in the reference frame of the GRS. Figure 1.3 shows sample trajectories computed from Fig. 1.2, with small dots indicating intervals of 10 hours. Figures 1.4 and 1.5 show the measured velocities and corresponding trajectories for

FIGURE 1.1 : *Voyager 2* image of the Great Red Spot (GRS) taken on July 5, 1979 (FDS 20517.32). All maps in this paper are labeled in degrees with planetographic latitude along the ordinate and System III longitude increasing westward along the abscissa. (In this image the actual projection is a Cartesian coordinate system with planetocentric latitude and longitude in equal increments along the two axes.)

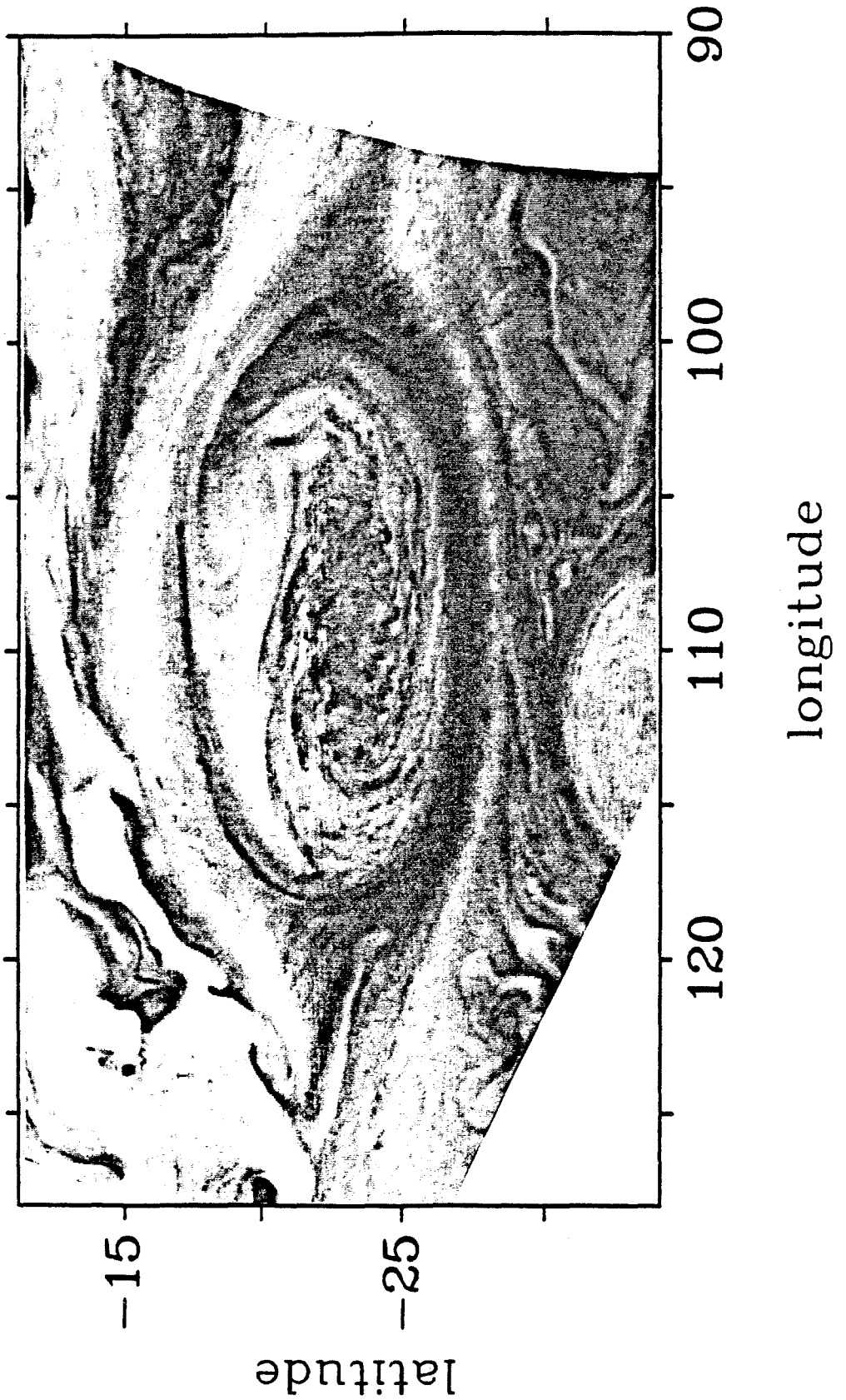
−15
−25
latitude
90
100
110
120
longitude

FIGURE 1.2 : Velocity data for the GRS. The location of each vector is marked with a dot, and the lines point downwind. The northward and eastward components of velocity are scaled equally in m/s, with 100 m/s indicated at the top left of the figure. Longitude and planetographic latitude are labeled in degrees and scaled equally, with the zero of longitude corresponding to System III on July 5, 1979.

FIGURE 1.3 : Trajectories computed for the GRS. Small dots indicate intervals of 10 hours. The averaging box used to determine the local velocity was 3° by 3° in size.

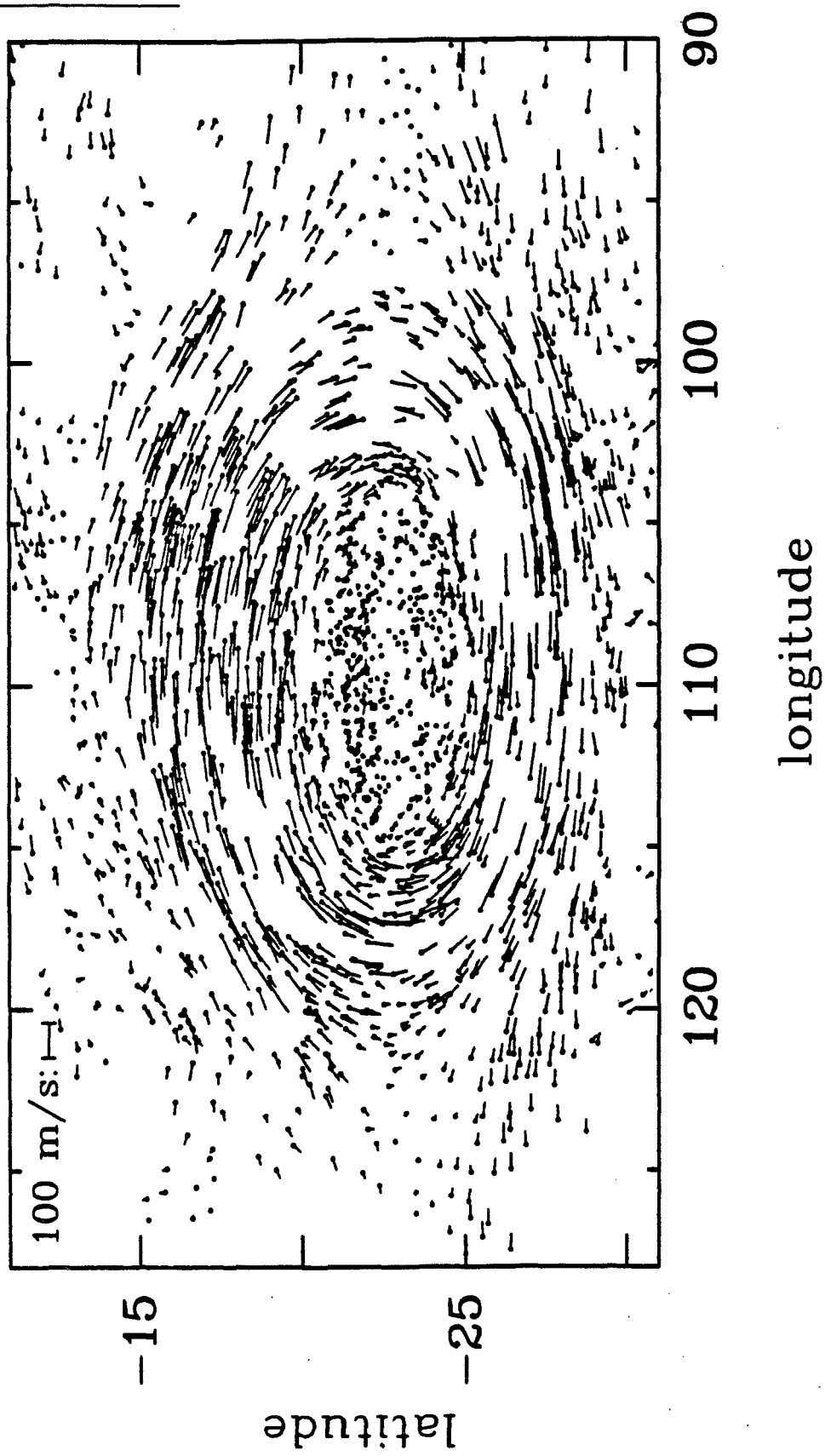
90
100
110
120
longitude
−15
−25
latitude
100 m/s

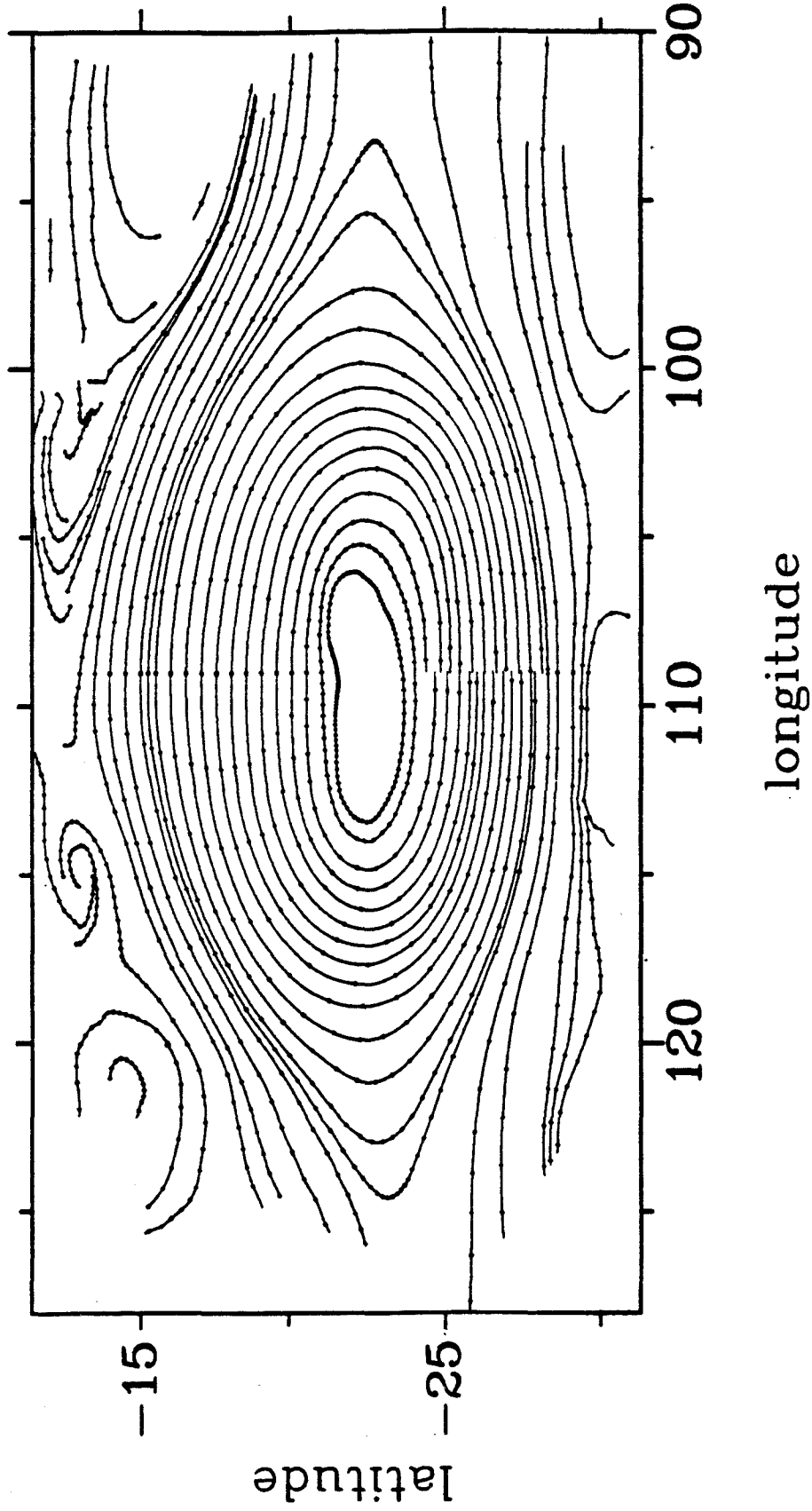
90
100
110
120
longitude
−15
−25
latitude

the Oval BC.

1.3 Method of Analysis

From the measured velocity vectors (Figs. 1.2 and 1.4), we compute vorticity, divergence, and fluid trajectories. To do this we use an averaging box $2d$ on a side, and fit the data within the box to smooth functions of the form

$$u = A_1\phi + B_1\lambda + C_1 \quad , \tag{1.1}$$

$$v = A_2\phi + B_2\lambda + C_2 \quad , \tag{1.2}$$

where u and v are eastward and northward velocity components, respectively. A least-squares fit determines the A's, B's, and C's as well as the error covariance matrix. The optimum value of the box size $2d$ is a compromise between having a large number of measured points in the box and being able to resolve small-scale structures in the flow. A minimum of 10 points per box at most locations leads to $d = 1.5°$ for the GRS and $d = 1.0°$ for the Oval BC.

Vorticity and divergence are linear functions of the velocities and velocity gradients and are therefore linear functions of the A's, B's, and C's. For an oblate spheroidal planet with $\epsilon = R_e/R_p$ the expressions involve the radii of curvature in the zonal and meridional directions, which are

$$r(\lambda) = R_e(1 + \epsilon^{-2}\tan^2\lambda)^{-1/2} \quad , \tag{1.3}$$

$$R(\lambda) = R_e\epsilon^{-2}(r/R_e\cos\lambda)^3 \quad , \tag{1.4}$$

respectively. Using the identity $\partial r/\partial\lambda = -R\sin\lambda$, we find for the vorticity ζ and the horizontal divergence $D = \nabla\cdot\mathrm{v}$,

$$\zeta = -\frac{1}{R}\frac{\partial u}{\partial\lambda} + \frac{u}{r}\sin\lambda + \frac{1}{r}\frac{\partial v}{\partial\phi} \quad , \tag{1.5}$$

FIGURE 1.4 : As in Fig. 1.2 but for the White Oval BC. The zero of longitude corresponds to System III on March 4, 1979.

FIGURE 1.5 : As in Fig. 1.3 but for the White Oval BC. The averaging box used to determine the local velocity field was 2° by 2°.

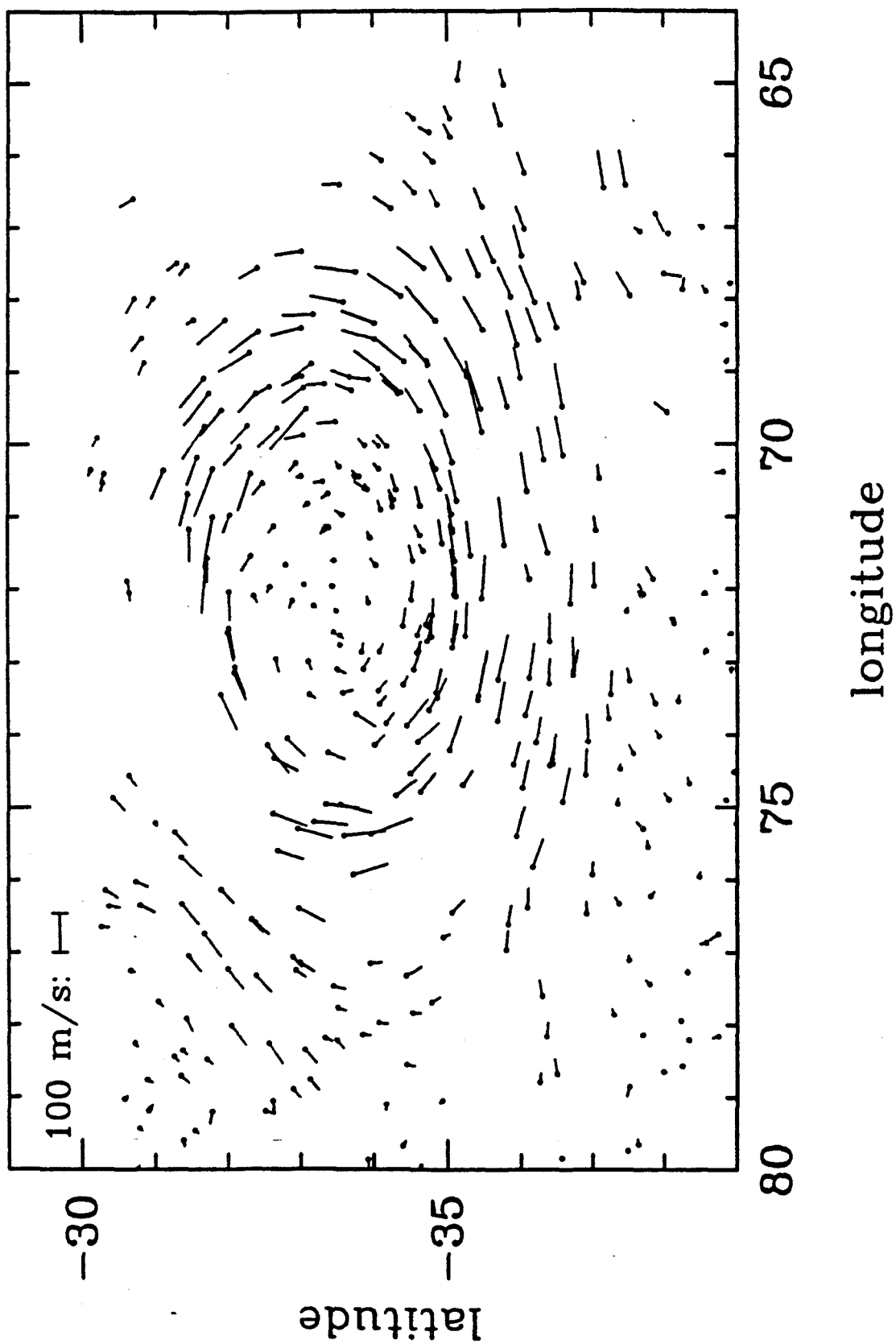
100 m/s:
−30
−35
latitude
65
70
75
80
longitude

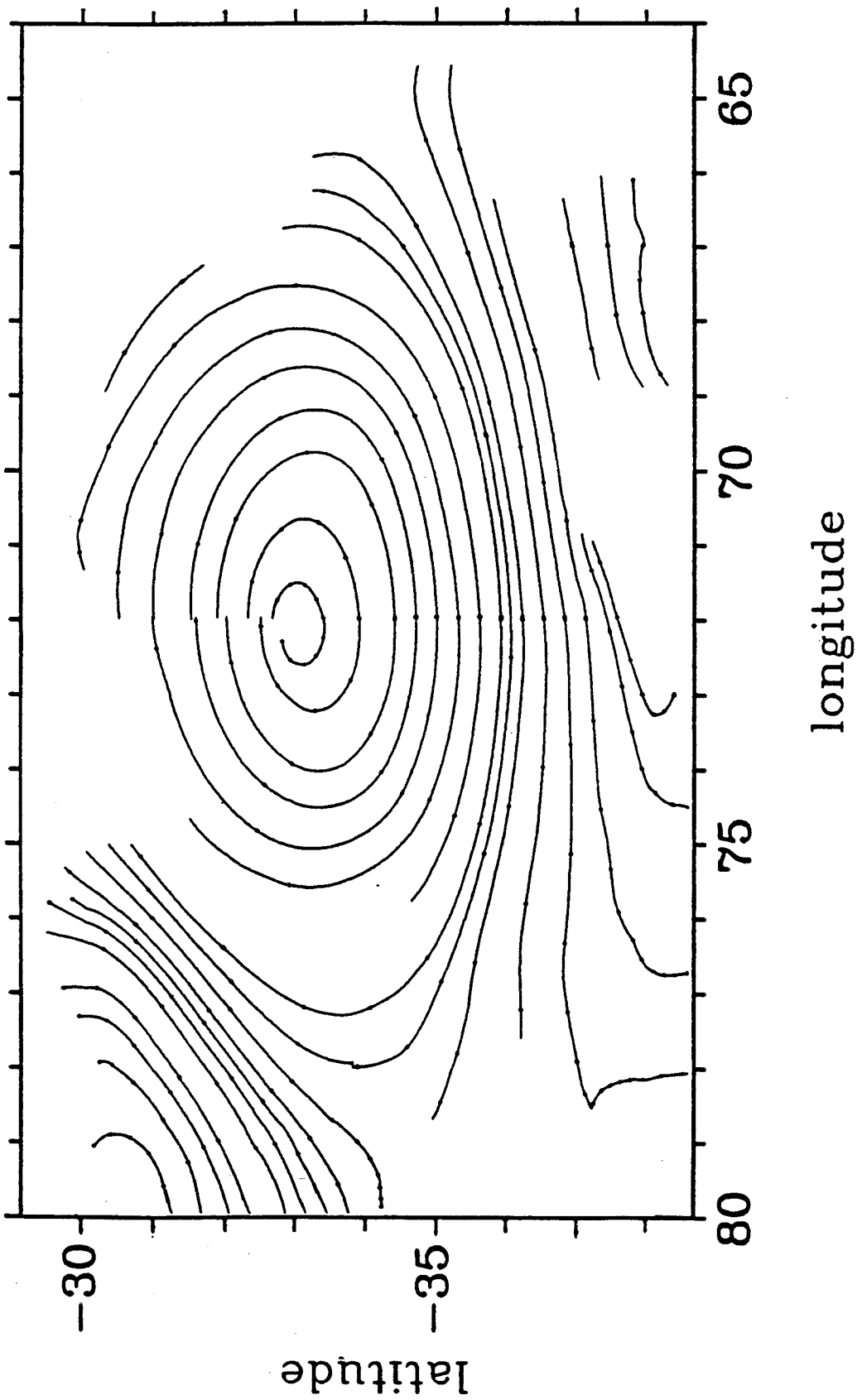
−30
−35
latitude
65
70
75
80
longitude

$$D = \frac{1}{R}\frac{\partial v}{\partial \lambda} - \frac{v}{r}\sin\lambda + \frac{1}{r}\frac{\partial u}{\partial \phi} \quad . \tag{1.6}$$

Throughout this paper we use east longitude in the equations and west longitude in the figures.

Trajectories are calculated by stepping forward in time, integrating the velocities u and v in (1.1) and (1.2) to reach the next location. The center of the box and the point on the trajectory leapfrog over each other on alternate parts of the time step. The equations to be integrated are

$$u = r\dot{\phi}, \qquad v = R\dot{\lambda} \quad . \tag{1.7}$$

Equations (1.1), (1.2), and (1.7) are written in the following form,

$$\frac{\phi_2 - \phi_1}{t_2 - t_1} = \frac{1}{r_1}\left(A_1\frac{\phi_1 + \phi_2}{2} + B_1\frac{\lambda_1 + \lambda_2}{2} + C_1\right) \quad , \tag{1.8}$$

$$\frac{\lambda_2 - \lambda_1}{t_2 - t_1} = \frac{1}{R_1}\left(A_2\frac{\phi_1 + \phi_2}{2} + B_2\frac{\lambda_1 + \lambda_2}{2} + C_2\right) \quad . \tag{1.9}$$

Equations (1.8) and (1.9) are solved for the coordinates of the new point on the trajectory (ϕ_2, λ_2), given the coordinates of the old point (ϕ_1, λ_1). The center of the box is integrated an additional half step $(t_2 - t_1)/2$ past the new point. There, new velocity vectors are collected and the least-squares program determines new values of the A's, B's, and C's. These values are substituted into (1.8) and (1.9), and the process is repeated. The time step $(t_2 - t_1)$ is chosen so that the displacement is never more than 4 percent of d. Halving the time step has no effect on the trajectories.

Figures 1.6 and 1.7 are maps of ζ and its standard deviation σ_ζ, respectively, for the GRS. Figure 1.8 is a map of D for the GRS, and Fig. 1.9 is a map of ζ for the Oval BC. These maps are made by moving the averaging box around a latitude–longitude grid. The grid spacing is 0.5°, which is 1/3 of d for the GRS and 1/2 of d for the Oval BC. Locations where there are fewer than 10 measured velocity vectors inside the

box are shown as black squares. Standard deviations σ_ζ and σ_D are computed from the error covariance matrix, assuming uncorrelated measurement errors and a perfect model ((1.1) and (1.2)). These assumptions are discussed further in the next section. The standard deviation σ_D (not shown) has the same large–scale structure as σ_ζ and approximately the same root mean square (rms) amplitude ($4.2 \times 10^{-6}\,s^{-1}$ for σ_D vs. $4.3 \times 10^{-6}\,s^{-1}$ for σ_ζ). Other standard deviations and rms amplitudes are given in Table 1.1.

Our trajectory analysis requires that the flow be steady. This requirement is approximately satisfied in the reference frames of the GRS and the Oval BC but not in System III. The transformation involves knowing the drift rates $\dot{\phi}_d$ of these objects relative to System III. The 126–day interval between the *Voyager 1* encounter and the *Voyager 2* encounter provides the time base. The simplest method is to use color or albedo to define the object (GRS or Oval BC). A better method for our purposes is to use the velocity data to define the object. Image pairs from *Voyager 1* are used to produce a velocity field by interpolating all the vectors onto the same latitude-longitude grid at one instant in time around the *Voyager 1* encounter. (The images in a pair are almost always 10 hours apart, but the *Voyager 1* pairs cover a 3- to 4-day period.) An initial guess of the drift rate is used in the interpolation. The same procedures are followed for *Voyager 2*. The displacement that minimizes the difference between the two velocity fields is computed by the method of least squares. The initial guess to the drift rate is corrected, and the procedure is repeated until it converges. The first method (albedo plus color) was used for the Oval BC, since the Oval BC velocity data are from *Voyager 1* only. The second method (velocities) was used for the GRS.

We find that the Oval BC drifted eastward relative to System III at an average rate of 0.392 ± 0.007 deg/day. The GRS drifted westward at an average rate of 0.258

FIGURE 1.6 : Relative vorticity ζ of the GRS. Light shades correspond to positive ζ (anticyclonic in southern hemisphere) and dark shades correspond to negative ζ. The vorticity was calculated every 0.5° from the least-squares fit to velocities inside a 3° by 3° box. The lightest and darkest shade (before black) equals the image mean plus and minus three image standard deviations, respectively. Black indicates less than ten data points available for computation. In this image, the image mean is $0.4 \times 10^{-6}\,\mathrm{s}^{-1}$ and the standard deviation is $19.2 \times 10^{-6}\,\mathrm{s}^{-1}$.

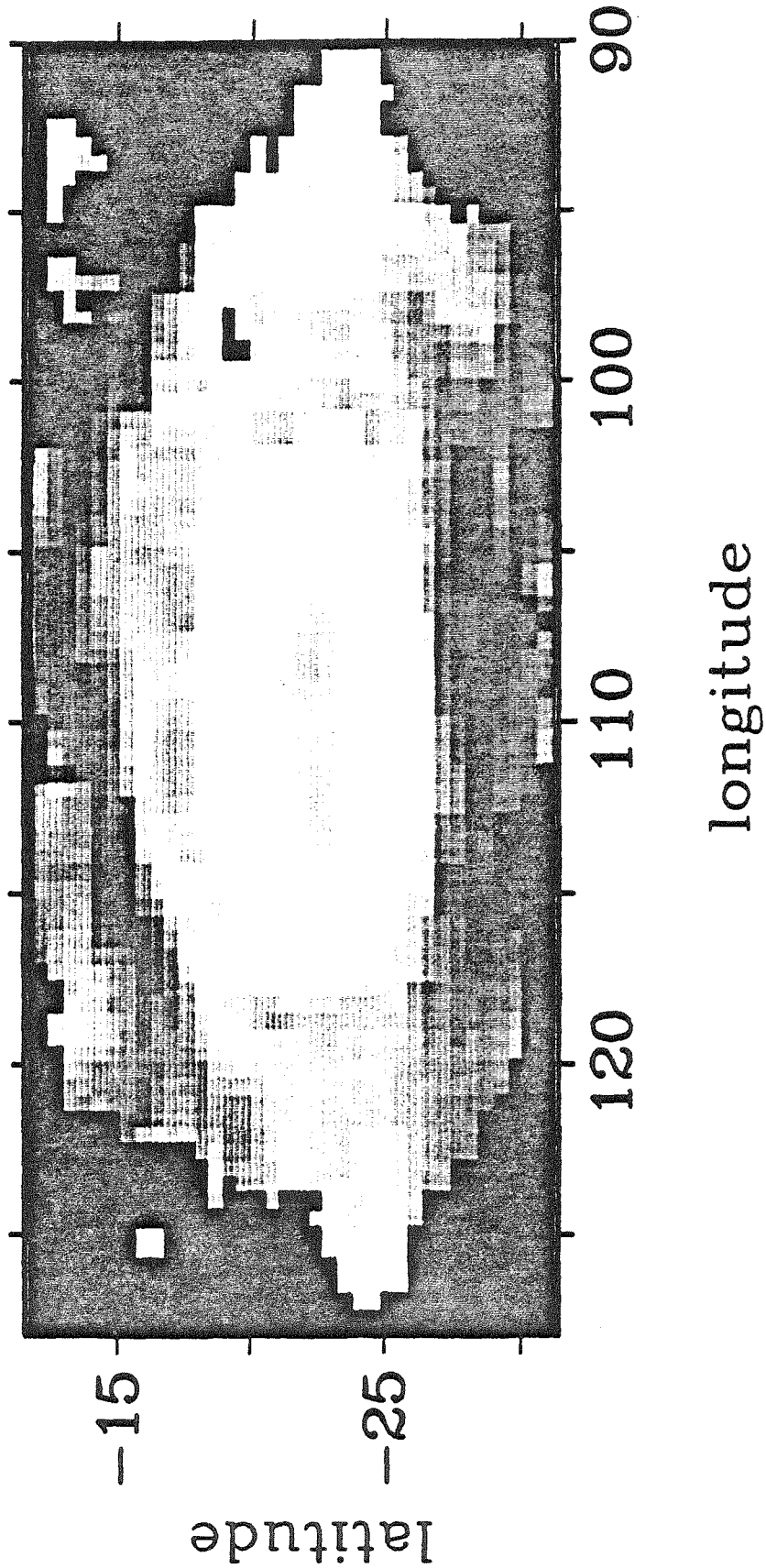
90
100
110
120
longitude
−15
−25
latitude

FIGURE 1.7 : Formal error map σ_ζ for the ζ in Fig. 1.6. The rms value of σ_ζ for this image is 4.3 $\times 10^{-6}\,s^{-1}$. The lightest shade corresponds to 9.9 $\times 10^{-6}\,s^{-1}$ and the darkest shade before black corresponds to zero.

FIGURE 1.8 : Horizontal divergence D of the GRS. The shading is as in Fig. 1.6 but with a mean of $-0.1 \times 10^{-6}\,s^{-1}$ and a standard deviation of 4.8 $\times 10^{-6}\,s^{-1}$.

FIGURE 1.9 : As in Fig. 1.6 but for the White Oval BC. The vorticity was calculated every 0.5° from the least-squares fit to velocities inside a 2° by 2° box. The shading is as in Fig. 1.6 but with a mean of 13.8 $\times 10^{-6}\,s^{-1}$ and a standard deviation of 36.6 $\times 10^{-6}\,s^{-1}$.

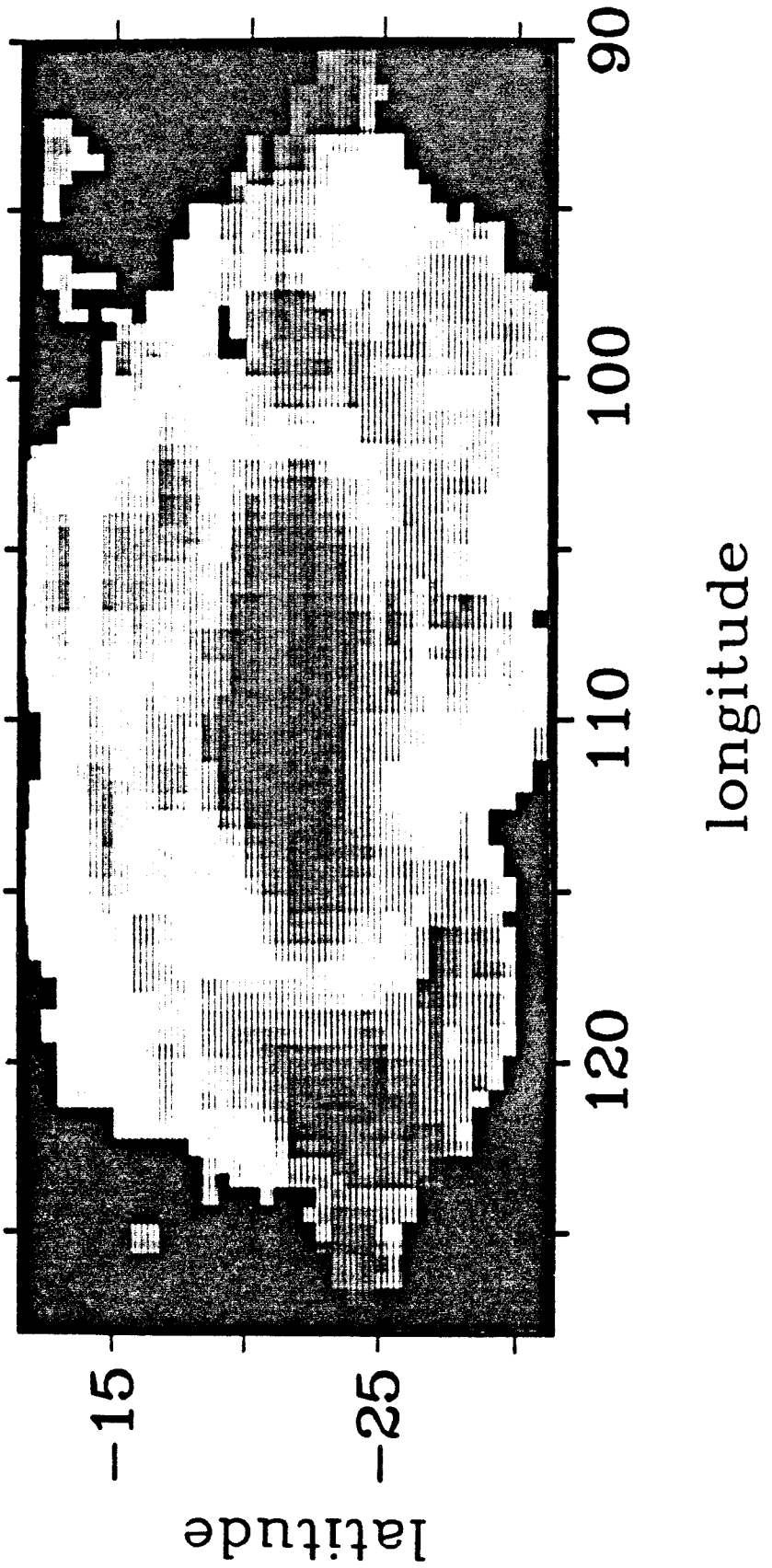
latitude
−15
−25
120
110
100
90
longitude


90
100
110
120
longitude
−15
−25
latitude

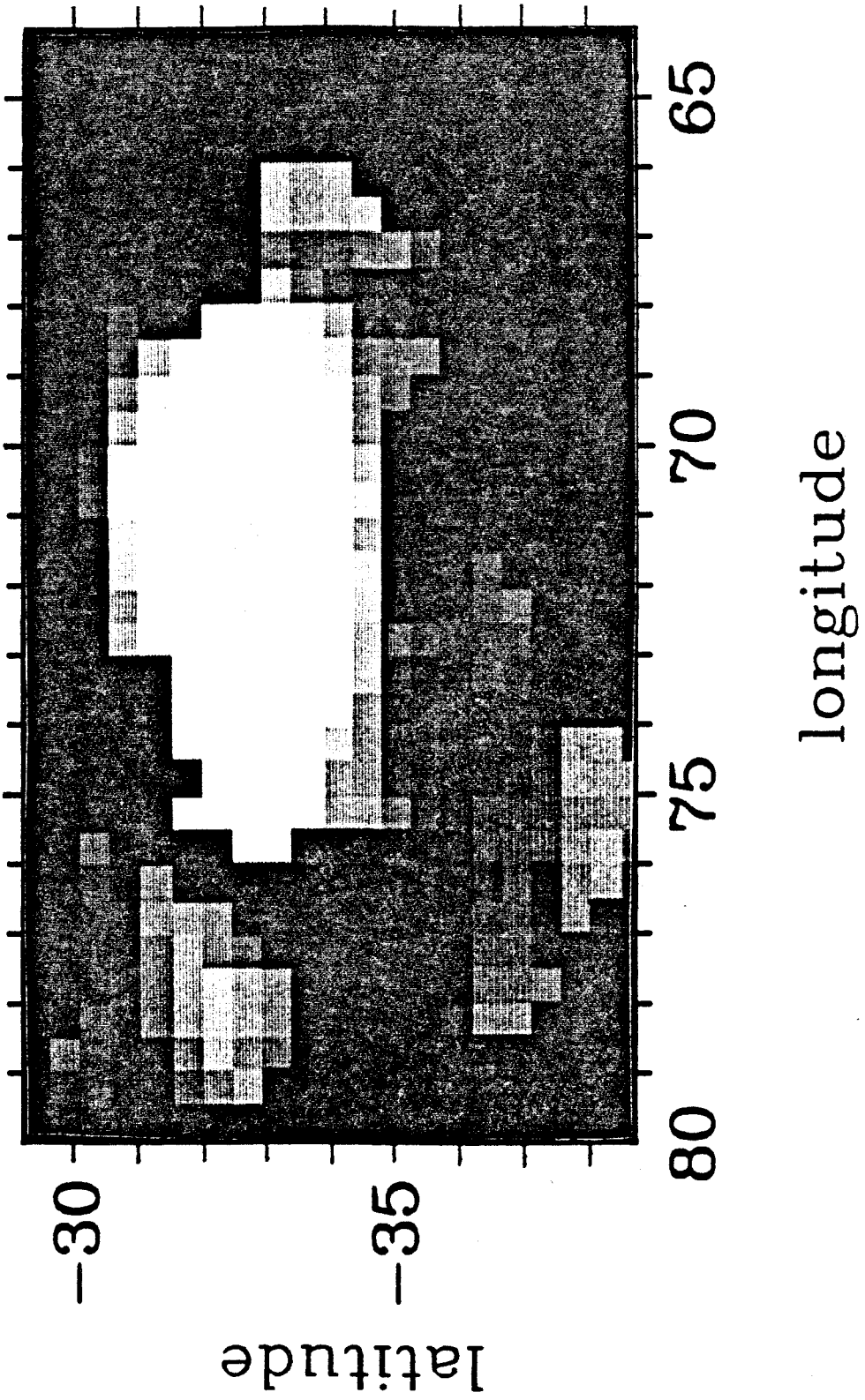
−30
−35
latitude
65
70
75
80
longitude

TABLE 1.1

Standard deviations and rms amplitudes.

Figure	Quantity	Value
1.6	GRS $\langle\zeta^2\rangle^{1/2}$	19.2
1.7	GRS σ_ζ	4.3
1.8	GRS $\langle D^2\rangle^{1/2}$	4.8
	GRS σ_D	4.2
1.9	BC $\langle\zeta^2\rangle^{1/2}$	39.1
	Synthetic $\langle\zeta^2\rangle^{1/2}$	15.9
	Synthetic σ_ζ	1.0
	Synthetic $\langle D^2\rangle^{1/2}$	1.1
1.11	Synthetic $\langle(\zeta_{\text{true}}-\zeta)^2\rangle^{1/2}$	4.1
	Random $\langle\zeta^2\rangle^{1/2}$	16.4
	Random $\langle D^2\rangle^{1/2}$	4.6
	Random σ_ζ, σ_D	4.4

Note: Units are 10^{-6} s^{-1}. The headings GRS, BC, Synthetic, and Random refer to the data in Figs. 1.2, 1.4, 1.10, and 1.12, respectively.

$\pm$ 0.001 deg/day. Since the longitude of the GRS oscillates with a 90-day period (e.g., Smith and Hunt, 1976), this average rate applies only to the time between the *Voyager* encounters. With these estimates of the drift rates, two changes were made to the original (ungridded) velocity data. First, the longitude of each vector was shifted into a single reference frame corresponding to System III on July 5, 1979, for the GRS and March 4, 1979, for the Oval BC. Second, the zonal velocity of each

vector was incremented by $-r\dot{\phi}_d$, where r is evaluated at the latitude of the vector and $\dot{\phi}_d$ is the drift rate of the GRS or the Oval BC. At the latitude of the GRS center, this velocity increment is 3.49 m/s. At the latitude of the Oval BC center, the velocity increment is -4.84 m/s. We also noticed a 0.2° latitude shift between the *Voyager 1* and *Voyager 2* velocity data. Following Limaye (1986), we attribute the shift to a problem with *Voyager 1* image navigation, and have corrected the *Voyager 1* latitudes accordingly.

1.4 Error Analysis

Errors of analysis and interpretation fall into three classes. The first class arises from the sampling strategy used to generate the wind vectors. The second class arises from measurement error and small–scale motions in Jupiter's clouds. The third class arises from the physical model, e.g., the assumption that potential temperature and potential vorticity are constant on trajectories. We assess the effects of the sampling strategy by applying it to a synthetic data set constructed from a known velocity field. Measurement error and small-scale motions are modeled by adding a random velocity to the synthetic data set. Our ability to recover the known velocity field from the synthetic data set provides an estimate of measurement error. Integral constraints provide a partial check of the physical model.

For the synthetic velocity field, we choose a simple harmonic motion with closed elliptical trajectories. The ellipses are concentric and have a constant ratio $a/b = 2.1$ of semimajor axis to semiminor axis in degrees. The latter value is from Mitchell *et al.* (1981) and is based on observations. Each ellipse, identified by its semimajor axis, has its own frequency $\omega(a)$. Thus, the coordinates $\phi(t, a)$ and $\lambda(t, a)$ of the fluid

parcel are

$$\phi(t,a) = \phi_o + a\cos\omega t \quad , \tag{1.10}$$

$$\lambda(t,a) = \lambda_o + a\left(\frac{b}{a}\right)\sin\omega t \quad . \tag{1.11}$$

The velocity field $u(\phi,\lambda)$, $v(\phi,\lambda)$ is given by

$$u(\phi,\lambda) = (\lambda_o - \lambda)r(\lambda)\left(\frac{a}{b}\right)\omega\left[a(\phi,\lambda)\right] \quad , \tag{1.12}$$

$$v(\phi,\lambda) = (\phi - \phi_o)R(\lambda)\left(\frac{b}{a}\right)\omega\left[a(\phi,\lambda)\right] \quad . \tag{1.13}$$

To make the flow resemble the observed flow around the GRS (Mitchell *et al.*, 1981), we choose

$$\omega(a) = \omega_o \frac{\left[\exp\left[-(a-a_o)^2/a_1^2\right] + a_2\right]}{(1+a_2)} \quad , \tag{1.14}$$

with $\omega_o = 1.1 \times 10^{-5}\,\mathrm{s}^{-1}$, $a_o = 8.7°$, $a_1 = 3.9°$, and $a_2 = 0.1$.

To simulate the *Voyager* observation sequence, we use the locations of the cloud features in the *Voyager* images, the same locations as those from which Fig. 1.2 was constructed. The features are displaced by increasing t in (1.10) and (1.11) by the appropriate amount, usually around 10 hours. Velocity vectors are computed from the differences in position over the finite time interval, as in the real data set. Vorticity and divergence are computed by least-squares fitting to (1.1) and (1.2).

Figure 1.10 shows the set of synthetic velocity vectors computed from (1.10)–(1.14). Despite the limitations of uneven sampling, finite differencing, and least-squares averaging, trajectories computed from this data set are near-perfect ellipses to an accuracy better than the line width. Figure 1.11 shows a map of $(\zeta_{\mathrm{true}} - \zeta)$, the difference between ζ computed analytically from (1.12) and (1.13) and ζ computed from the velocity vectors of Fig. 1.10. This error in ζ is dominated by large-scale structure. Its rms amplitude is $4.1 \times 10^{-6}\,\mathrm{s}^{-1}$. For comparison, the quantity ζ

that we are trying to measure has rms amplitudes of 19.2 $\times 10^{-6}\,s^{-1}$ for the GRS velocities (Fig. 1.2) and 15.9 $\times 10^{-6}\,s^{-1}$ for the synthetic velocities (Fig. 1.10).

Figures 1.7 and 1.11 show two parts of the same quantity, namely, the uncertainty in our measurement of ζ. Figure 1.7 shows σ_ζ for the real data set (Fig. 1.2). It measures the small–scale structure of the velocity field — structure that does not fit the model, (1.1) and (1.2), inside the averaging box. Such structure is largely absent from the synthetic data set (Fig. 1.10), as shown by the fact that σ_ζ for that data set is only 1.0 $\times 10^{-6}\,s^{-1}$ (vs. 4.3 $\times 10^{-6}\,s^{-1}$ for the real data). Figure 1.11 shows $(\zeta_{\text{true}} - \zeta)$ for the synthetic data set. It measures the effects of finite differencing (displacements over 10 hours), nonuniform spatial sampling, and least-squares averaging within the $2d \times 2d$ box. As mentioned in the preceding paragraph, the rms amplitude of the quantity shown in Fig. 1.11 is 4.1 $\times 10^{-6}\,s^{-1}$. The total uncertainty in our estimate of ζ is taken to be the rms combination of the uncertainties shown in Figs. 1.7 and 1.11. This combined error is about 6 $\times 10^{-6}\,s^{-1}$, which is 30 percent of the rms ζ and 6 percent of the total range of $(\zeta + f)$.

The residuals in the fit of u and v to (1.1) and (1.2) provide information about small–scale structure in the velocity field (Figs. 1.2 and 1.4). The rms residuals of the velocity vector are 17.5 m/s for the GRS and 18.5 m/s for the Oval BC. About 85 percent of the variance σ_v^2 is associated with the downstream component of velocity. The remainder is associated with the cross–stream component. This anisotropy is probably due to the filamentary nature of the cloud patterns (Fig. 1.1). The features are stretched out in the direction of motion and are harder to locate in that direction than in the cross–stream direction. The fact that $\langle D^2 \rangle^{1/2}$ is not significantly larger than σ_ζ or σ_D (Table 1.1) implies that the velocity errors are uncorrelated and the divergence is small. Under such circumstances, σ_ζ^2, σ_D^2, and $\langle D^2 \rangle$ should all be of order $3\sigma_v^2/(Nd^2)$, where N is the number of vectors in the averaging box of side $2d$

FIGURE 1.10 : Synthetic GRS-like velocity field. The velocities were computed by finite differencing an analytical function, (1.10)–(1.14), using the mean positions and time intervals of the GRS data. Velocities are plotted as in Fig. 1.2.

FIGURE 1.11 : The difference between the analytical vorticity ζ_{true} and the ζ recovered from the corresponding synthetic velocities in Fig. 1.10. The light and dark regions correspond to positive and negative values of $(\zeta_{\text{true}} - \zeta)$, respectively. The shading is as that in Fig. 1.6 but with a mean of $0.3 \times 10^{-6}\,\text{s}^{-1}$ and a standard deviation of $4.1 \times 10^{-6}\,\text{s}^{-1}$.

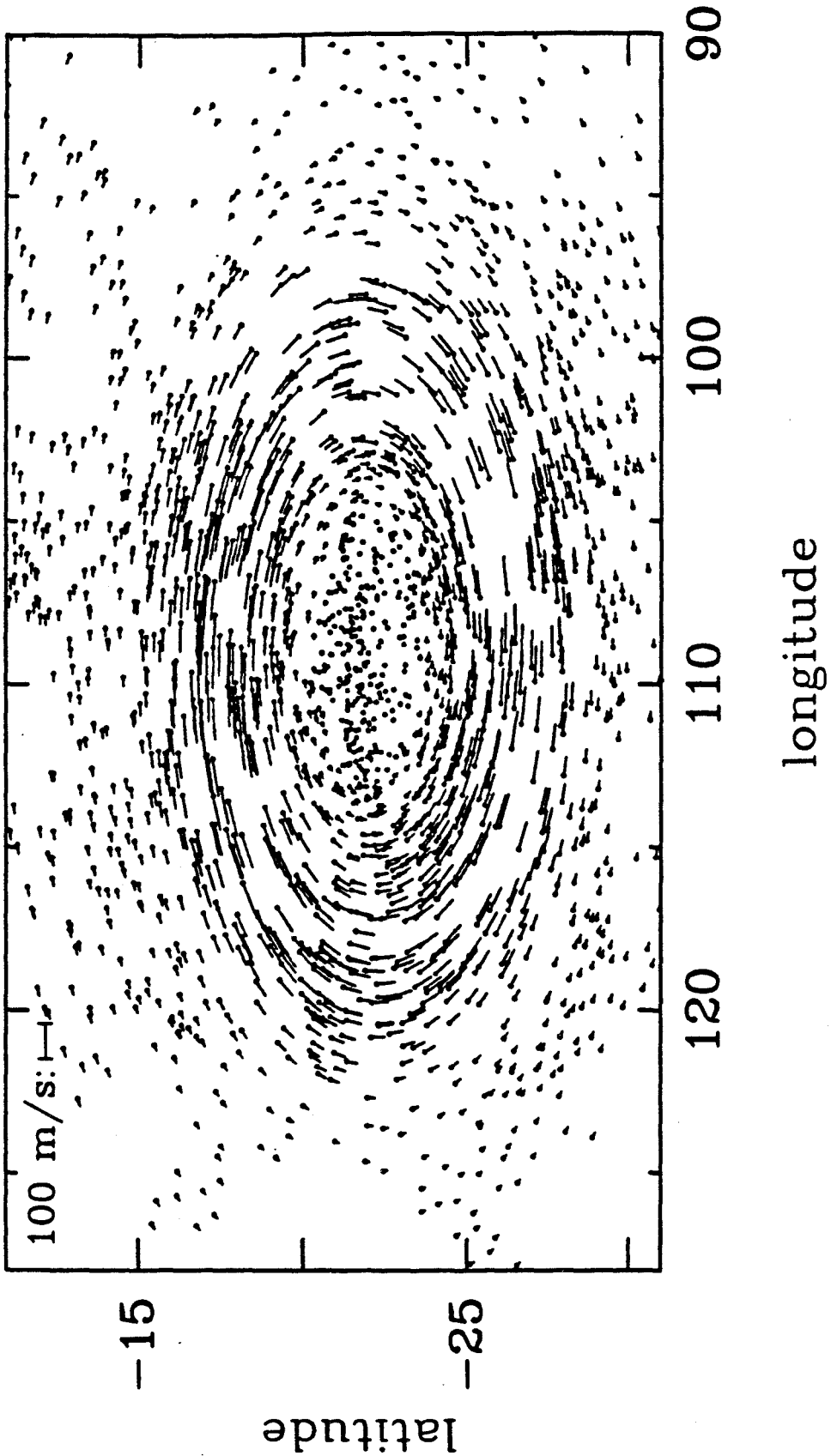
90
100
110
120
longitude
−15
−25
latitude
100 m/s


90
100
110
120
longitude
−15
−25
latitude

($\langle 1/N \rangle = 1/22$ for the GRS, $\langle 1/N \rangle = 1/14$ for the Oval BC). Substituting $\sigma_v = 17.5$ m/s, $d = 1800$ km, $N = 22$, one obtains $\sigma_\zeta \approx \langle D^2 \rangle^{1/2} \approx 3.6 \times 10^{-6}\,\mathrm{s}^{-1}$, in reasonable agreement with the numbers of the GRS data set.

Figure 1.12 shows the synthetic data set with a normally distributed random velocity added independently to each vector. The standard deviation is 16.2 m/s in the component parallel to the large–scale flow and 6.7 m/s in the perpendicular component. This data set has essentially all of the statistical properties of the GRS data set (Table 1.1) and has the same general appearance as Fig. 1.2. Adding the random velocity isotropically (12.4 m/s in each component) has a distinctly noisier appearance. We conclude that the GRS velocity errors are essentially uncorrelated, lie mostly in the downstream direction and have an rms magnitude of about 17.5 m/s. The Oval BC velocity errors are also uncorrelated and directed downstream with an rms magnitude of 18.5 m/s.

1.5 Equations and Integral Constraints

Our interpretation of the data relies on the equations of motion with potential temperature θ as a vertical coordinate (e.g., Haltiner and Williams, 1980). For large-scale (hydrostatic) flow of a stably stratified fluid ($H = -\partial P/\partial\theta > 0$), the continuity equation is

$$\frac{\partial H}{\partial t} + \nabla \cdot (\mathrm{v} H) + \frac{\partial}{\partial \theta}(\dot{\theta} H) = 0 \quad . \tag{1.15}$$

Here, v is the two–dimensional (horizontal) velocity, and $\dot{\theta}$ is the rate of change of θ following the fluid motion. For large-scale, frictionless flow, the vorticity equation is

$$\frac{\partial(\zeta + f)}{\partial t} + \nabla \cdot [\mathrm{v}(\zeta + f)] + \hat{k} \cdot \nabla \times \left(\frac{\dot{\theta} \partial \mathrm{v}}{\partial \theta} \right) = 0 \quad . \tag{1.16}$$

FIGURE 1.12 : Synthetic velocity field with noise. This is the same as Fig. 1.10, except that Gaussian noise is added to the positions used in the finite-difference velocity calculation. The standard deviation of this noise in terms of velocity is 17.5 m/s, with 85 percent of the variance associated with the downstream component and 15 percent associated with the cross-stream component. This random data set has $\sigma_\zeta \approx \sigma_D \approx \langle D^2 \rangle^{1/2} = 4.6 \times 10^{-6}\,\mathrm{s}^{-1}$, which is close to the values for the real data set (Table 1.1).

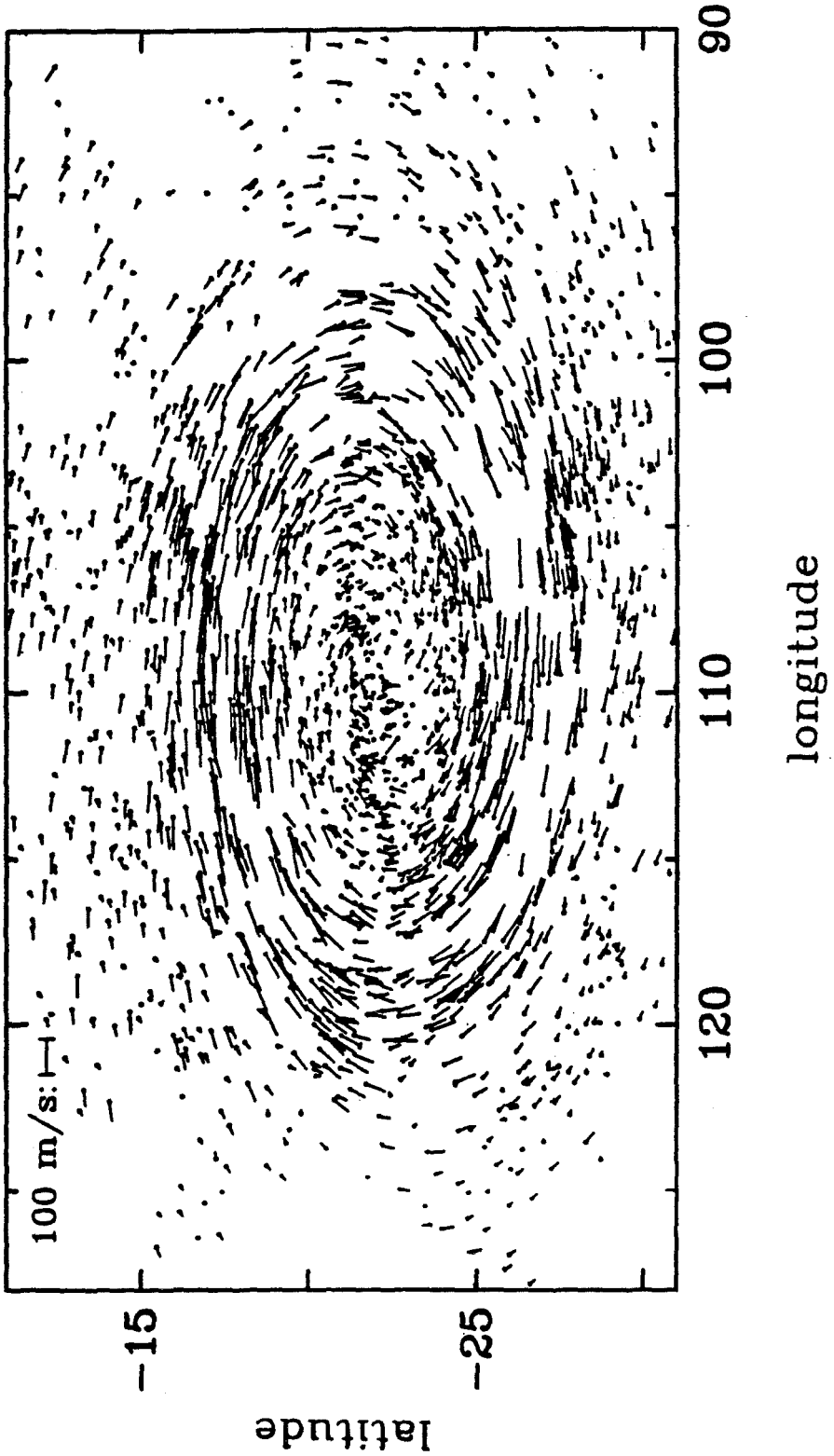
100 m/s
−15
−25
latitude
90
100
110
120
longitude

If the flow is adiabatic, then $\dot{\theta} = 0$, and the two equations may be combined to yield

$$\frac{\partial}{\partial t}\left(\frac{\zeta + f}{H}\right) + \mathrm{v} \cdot \nabla \left(\frac{\zeta + f}{H}\right) = 0 \quad . \tag{1.17}$$

Equation (1.17) is the conservation of potential vorticity for large–scale, adiabatic, frictionless flow.

One implication of the above equations with $\partial/\partial t = 0$ and $\dot{\theta} = 0$ is that every trajectory must close on itself. To see this, consider a trajectory that spirals slowly outward. Let C be one cycle of the trajectory — an almost closed loop with a short section S across the place where the ends fail to join. Integrate (1.15) over the area enclosed by $C + S$. The second term can be turned into a surface integral, and since v is parallel to C, the entire (positive definite) contribution comes from S. If $\partial/\partial t = 0$ and $\dot{\theta} = 0$, the contribution from S must vanish and the trajectories must be closed.

Since the trajectories of Figs. 1.3 and 1.5 fail to close by small amounts, we can use the above argument to estimate the possible importance of the $\partial/\partial t$ and $\dot{\theta}$ terms. The average of the second term in (1.15) over the domain is

$$|\nabla \cdot (\mathrm{v}H)| \sim \frac{v_s H_s D_s}{A_{C+S}} \quad , \tag{1.18}$$

where v_s, H_s, and D_s are velocity, thickness, and distance, respectively, across the short section S, and A_{C+S} is the area enclosed by $C + S$. If the flow were steady and adiabatic, then (1.15) would give $\nabla \cdot (\mathrm{v}H) = 0$, whence

$$H\nabla \cdot \mathrm{v} + \mathrm{v} \cdot \nabla H = \nabla \cdot (\mathrm{v}H) = 0 \quad . \tag{1.19}$$

This relation is essential for deriving (1.17), the conservation of potential vorticity. We can estimate the extent to which the relation is violated by comparing the magnitude of $\nabla \cdot (\mathrm{v}H)$ with either of the other terms in (1.19), e.g., $\mathrm{v} \cdot \nabla H$. As we shall see, H varies by its own magnitude as latitude varies by 20°. Thus

$$|\mathrm{v} \cdot \nabla H| \sim \frac{vH}{L} \quad , \tag{1.20}$$

where L is 20°. The ratio of (1.18) to (1.20) is therefore of order $D_s L/A_{C+S}$. From Fig. 1.3 we estimate $D_s \sim 0.1°$, $A_{C+S} \sim \pi \times 8° \times 3°$, and so $D_s L/A_{C+S} \sim 0.03$, which is an estimate of the fractional error in (1.19).

Most or all of the spiraling in Figs. 1.3 and 1.5 is due simply to error in the velocity measurement. Applying our trajectory algorithm to the synthetic velocity field with noise (Fig. 1.12) gives as much spiraling as in the real data set. Without noise, the synthetic data set (Fig. 1.10) gives much less spiraling than the real data set. Spiraling could also arise from poorly resolved, small-scale eddies, time-dependent motions, or motions across potential temperature surfaces. Spiraling could arise if the observed velocity vectors were from different altitudes, that is, from different potential temperature surfaces. The integrated effect of these processes is no larger than the 3 percent error in (1.19), a negligible effect. However, we cannot rule out local errors larger than the 3 percent value, provided such errors cancel out when the integral around the trajectory is taken.

Equation (1.19) can also be used to estimate the magnitude of the horizontal divergence D, since

$$D = \nabla \cdot \mathbf{v} = -\mathbf{v} \cdot \nabla \log H \sim v/L \quad , \tag{1.21}$$

where L is 20° as before. From Fig. 1.3 we estimate that the maximum meridional displacement is 1.7° in 10 hours ($v \sim 54$ m/s), whence $v/L \sim 2.4 \times 10^{-6}\,\mathrm{s}^{-1}$. Since $\log H$ increases poleward at the latitude of the GRS, we expect positive D on the east side and negative D on the west side. This large–scale pattern, which we measure indirectly by observing vorticity changes, is barely discernible in the divergence map, Fig. 1.8. In a regression analysis of the Fig. 1.8 data, the large-scale pattern implied by (1.21) shows up with 90 percent of its expected amplitude. However, the rms amplitude of the divergence in Fig. 1.8 is $4.8 \times 10^{-6}\,\mathrm{s}^{-1}$ and is apparently dominated by small–scale noise.

1.6 Results

In this section we show how $(\zeta + f)$ varies along trajectories. Such variations must be associated with variations in H, since $(\zeta + f)/H$ is constant on trajectories. The magnitude of the constant is unknown, so we will focus on relative changes, i.e., changes of $\log|\zeta + f|$. We will discuss the magnitude of the variations as well as any obvious patterns that repeat from one trajectory to the next.

Figure 1.13 shows a set of trajectories around the GRS, condensed from Fig. 1.3. The trajectories are labeled *a*–*h*. The variation of $(\zeta + f)$ around each trajectory is shown in Fig. 1.14. Latitude is used to identify position on the trajectory, the left and right sides of Fig. 1.14 referring to the left and right sides of the trajectory, respectively. The gently curving dashed line is f as a function of latitude. Each curve is offset from the one below it by $75 \times 10^{-6}\,\mathrm{s}^{-1}$. Figures 1.15 and 1.16 show a similar set of curves for the Oval BC, the trajectories for which are labeled *a*–*f*.

The first conclusion is that the relative changes of $(\zeta + f)$ vs. latitude are the same for all trajectories despite their different longitudes. That is, except for small-scale noise and a different scaling factor for each trajectory, the different curves in Fig. 1.14 could be sections of the same smooth curve. A similar statement holds for the curves of Fig. 1.16. One can compare the curves both across the figures and down the figures. In the former case one observes that on each trajectory, a parcel returns to the same value of $(\zeta + f)$ as it crosses the same latitude on the east and west ends of the oval. In the latter case one observes that parcels on different trajectories j at different longitudes ϕ experience the same relative variations of $(\zeta + f)$ as they cross the same latitude λ. The solid curves represent $\log|(\zeta + f)/f_o| = (A\lambda^2 + B\lambda + Cj)$, with the same values of A and B used for the whole figure ((1.22), below). The congruence of the curves with the data points argues that the derivatives $(\partial \log|\zeta + f|/\partial\lambda)_j$ measured at the same latitude but on different trajectories j at different longitudes

FIGURE 1.13 : Selected GRS trajectories. The trajectories shown here are a subset of those in Fig. 1.3 and are used in the potential vorticity analysis of Fig. 1.14.

FIGURE 1.14 : Absolute vorticity $(\zeta + f)$ along trajectories versus latitude, for the GRS. Each $(\zeta + f)$ profile is labeled with a letter corresponding to a trajectory in Fig. 1.13. The left and right panels correspond to the trajectory segments left (west) and right (east) of 109° longitude, respectively. For each trajectory there are three pairs of curves, and these curves are offset from the next by 75 $\times$ $10^{-6}\,s^{-1}$ in the ordinate. The heavy dots are the computed $(\zeta + f)$. The gently sloping, dashed curves are f. The solid curves are a least-squares fit to (1.22), namely, $\log[(\zeta + f)/f_o] = A\lambda^2 + B\lambda + C_j$, where λ is planetographic latitude and j is the trajectory index.

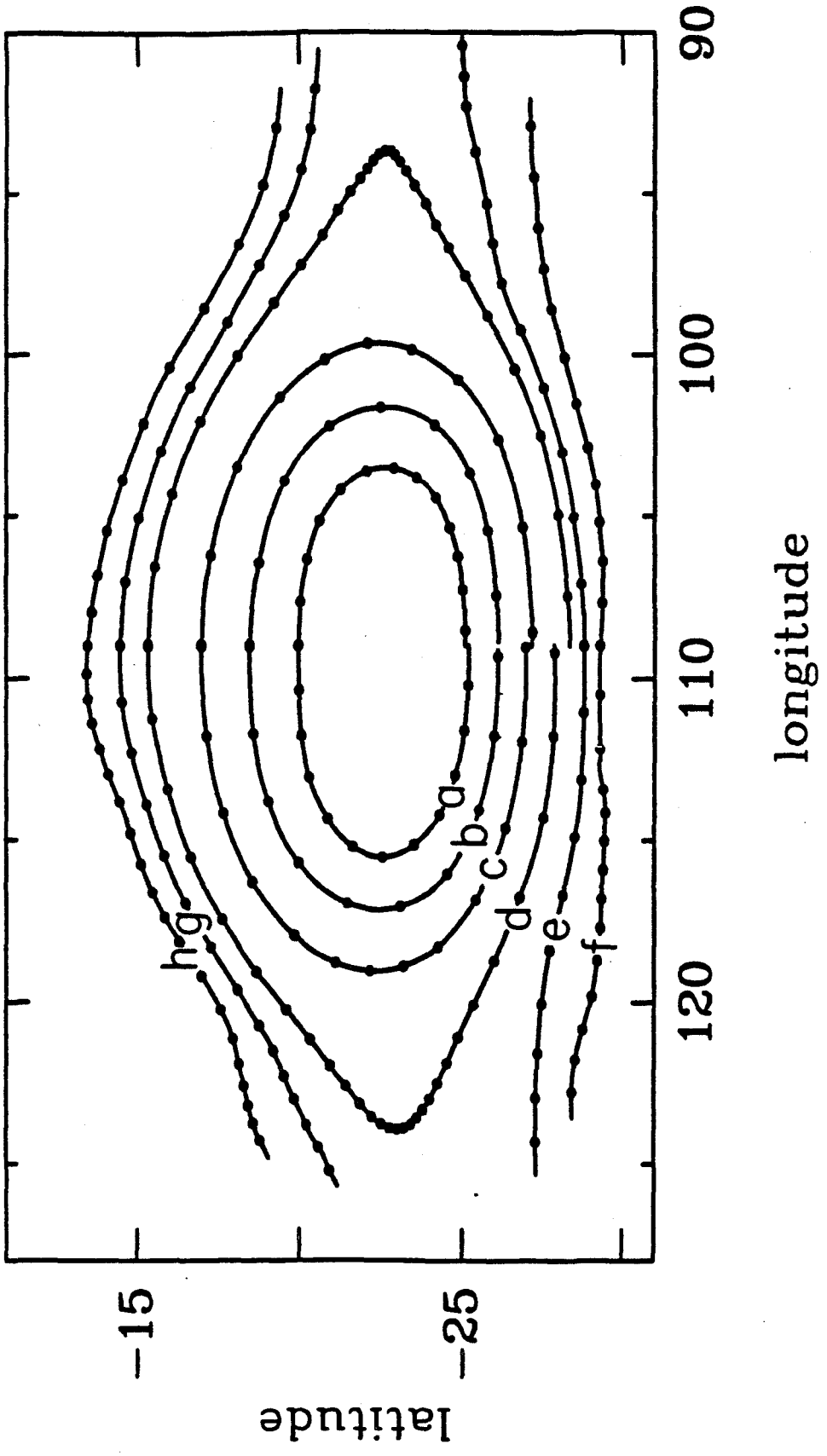
latitude
−15
−25
longitude
90
100
110
120
a
b
c
d
e
f
g
h

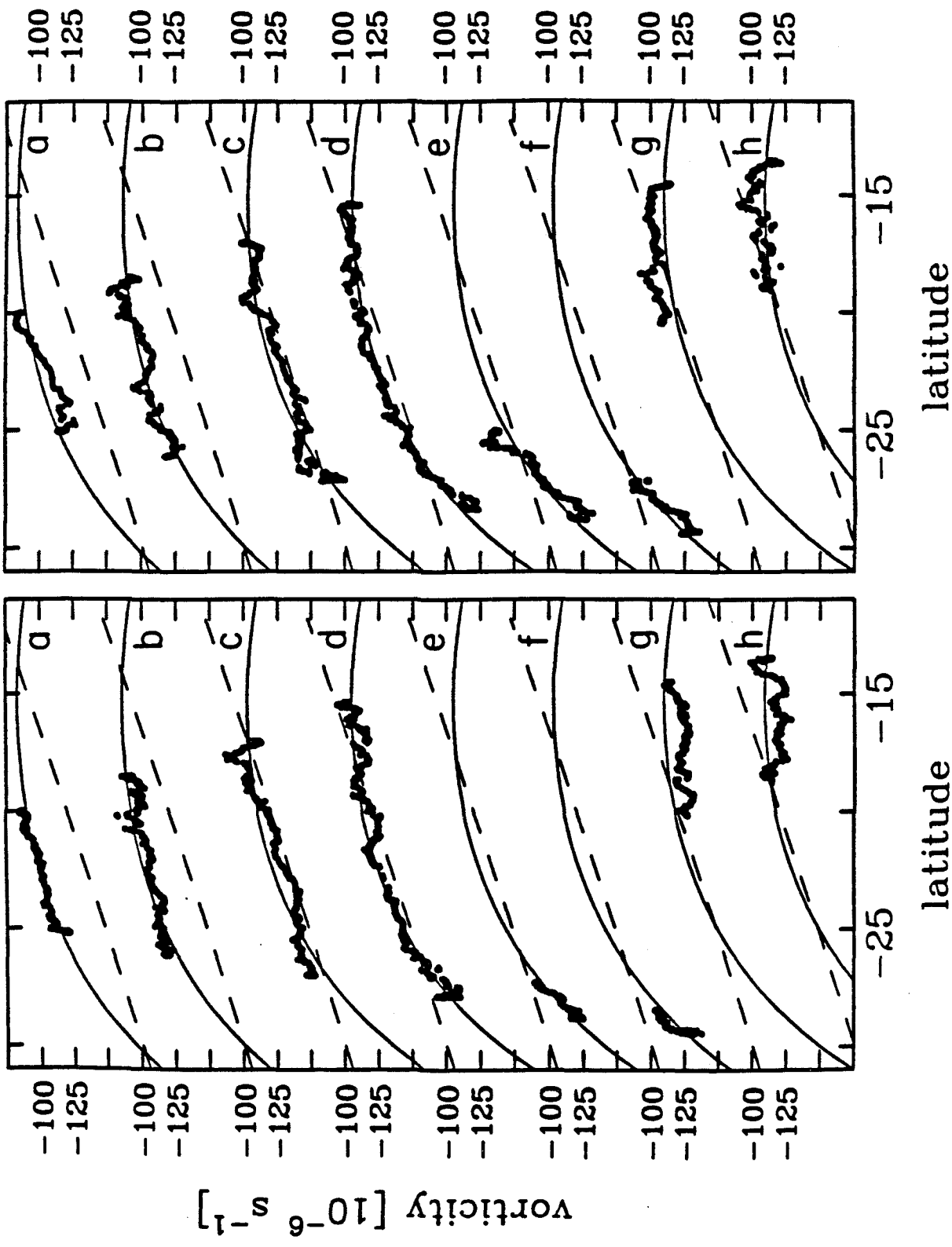
vorticity [10^{-6} s^{-1}]
−100
−125
a
b
c
d
e
f
g
h
−25
−15
latitude

FIGURE 1.15 : As in Fig. 1.13 but for the White Oval BC.

FIGURE 1.16 : As in Fig. 1.14 but for the White Oval BC. The left and right panels correspond to the trajectory segments left (west) and right (east) of 72° longitude, respectively. The curves are offset 100 $\times$ 10^{-6} s^{-1} in the ordinate.

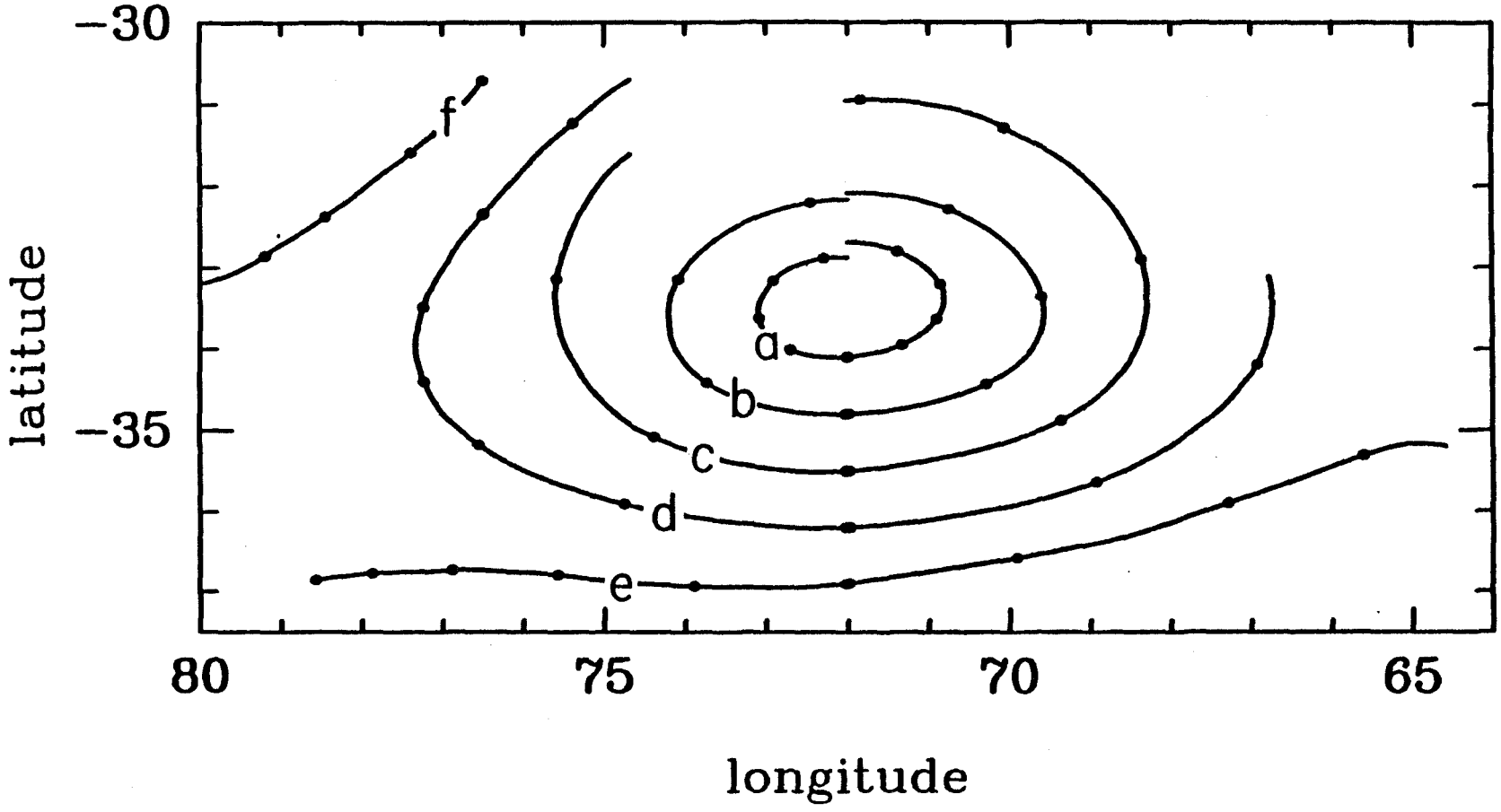
−30
−35
latitude
80
75
70
65
longitude
a
b
c
d
e
f

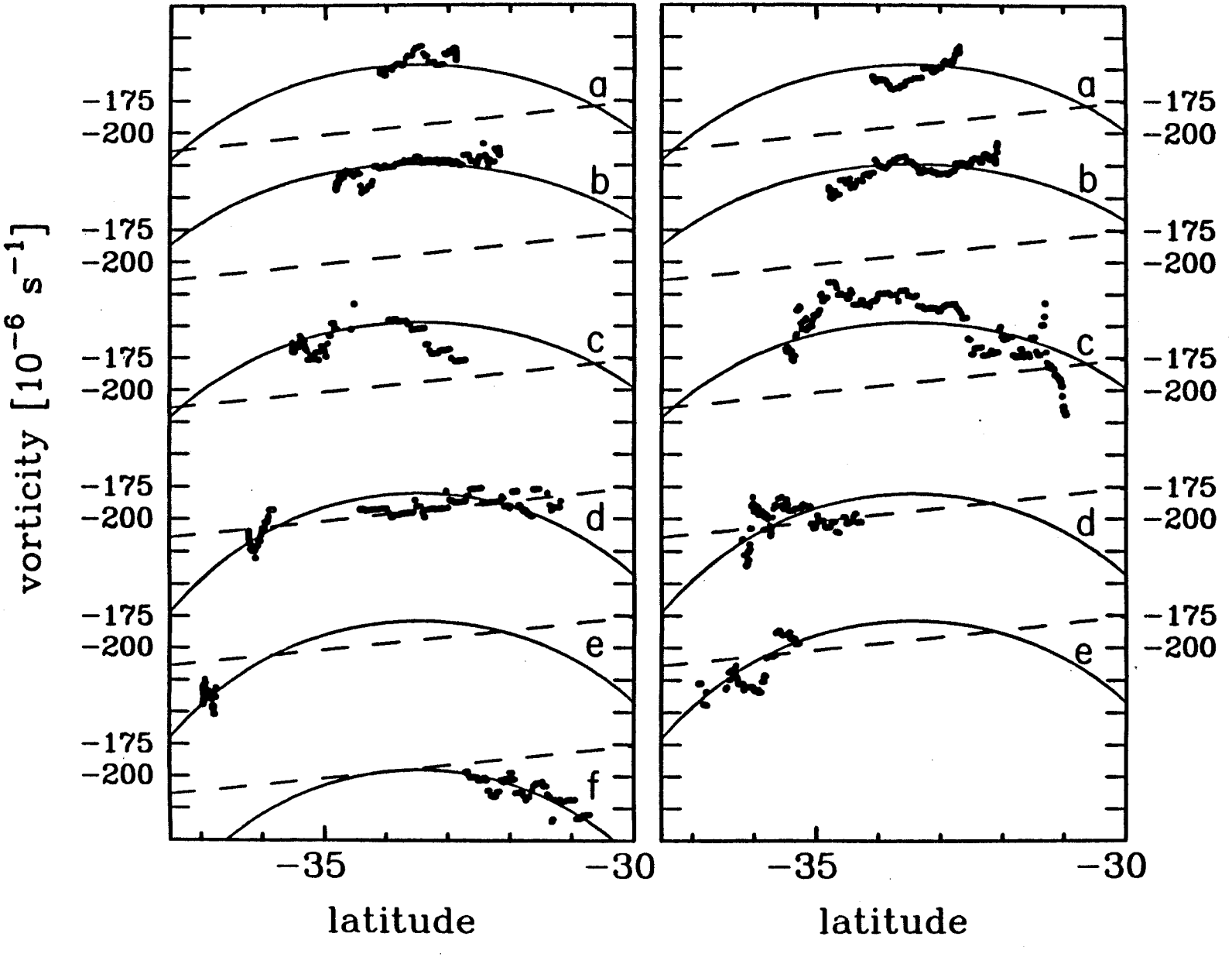
vorticity [10^{-6} s^{-1}]
−175
−200
a
b
c
d
e
f
−35
−30
latitude

ϕ are the same.

The mathematical statement of this conclusion is that $(\zeta + f)$ can be approximately represented by a separable function $G_j\hat{H}(\lambda)$ of trajectory and latitude. Since $(\zeta + f)/H$ depends only on j, it follows that H can also be represented by a separable function $E_j\hat{H}(\lambda)$, with the same latitude dependence $\hat{H}(\lambda)$. Stated differently, the conclusion is that $(\partial \log |\zeta + f|/\partial\lambda)_j$ is approximately independent of longitude, and can therefore be represented both at the center of each vortex and at its east and west ends by the same function, $\partial \log \hat{H}/\partial\lambda$. This is one way to organize the data of Figs. 1.14 and 1.16. A slightly different way, based on a physical model, is discussed in the next section.

The second important conclusion is that the latitudinal variations of thickness are dynamically significant: The slopes $\partial \log \hat{H}/\partial\lambda$ are typically larger than $\partial \log f/\partial\lambda$. Good examples are the poleward parts of GRS trajectories *d–f*, the poleward parts of the Oval BC trajectories *d–e*, and the equatorward parts of the Oval BC trajectories *c* and *f*. This fact means that the effect of thickness variation with latitude is typically greater than the effect of Coriolis parameter variation with latitude — the beta effect.

Third, there are important similarities in the distribution of slopes $\partial \log \hat{H}/\partial\lambda$ vs. λ for the GRS and the Oval BC. The curvature $\partial^2 \log \hat{H}/\partial\lambda^2$ is positive in both cases. Following trajectories, thickness increases sharply with southern latitude (increasing toward the pole faster than $|f|$) on the poleward sides of the GRS and the Oval BC. Thickness increases at about the same rate as $|f|$ ($\partial \log \hat{H}/\partial\lambda \sim \partial \log f/\partial\lambda$) on trajectories that cross the central latitudes of the GRS, and the Oval BC. Thickness is constant along trajectories on the equatorward side of the GRS and increases toward the equator on the equatorward side of the Oval BC. The data are not consistent, for instance, with models in which thickness varies linearly with latitude along trajectories. We will return to this point in the next section.

The fitted curves in Figs. 1.14 and 1.16 were constructed by the method of least squares. For either the GRS or the Oval BC, the value of $(\zeta + f)$ at latitude λ and on trajectory j is assumed to follow

$$\log\left[\frac{(\zeta + f)}{f_o}\right] = \log \hat{H}(\lambda) + C_j = A\lambda^2 + B\lambda + C_j \quad . \tag{1.22}$$

The value of λ and the trajectory j are both functions of the point i at which ζ is measured. For N trajectories there are $N+2$ constants to be determined. These are A and B, which determine $\partial \log \hat{H}/\partial\lambda$ for all trajectories, and the C_j, which determine the ratios of the values of $|\zeta + f|$ on different trajectories at the same λ. The constant f_o does not affect these ratios. For the GRS we choose $f_o = 2\Omega \sin(-22.5°)$, and for the Oval BC we choose $f_o = 2\Omega \sin(-33°)$.

Table 1.2 gives the results of this least-squares analysis. Figures 1.17 and 1.18 show the data in the form $C_j - \log|\zeta + f|$. The smooth curve is the function $-A\lambda^2 - B\lambda$. The zero of the ordinate is arbitrary. The spread is due to several factors: small-scale variations on individual trajectories, lack of agreement between the left and right halves of the same trajectory, and large-scale structure that does not fit the quadratic form (1.22). Generally the spread is small enough so that the curve is well defined. For the GRS, the ratio of the constant A to the formal uncertainty that comes from the least-squares analysis is 7. For the Oval BC the ratio is 2.5. In other words the curvature is statistically significant. Similarly, on the poleward side of the GRS ($\lambda = -28.5°$), the magnitude of the slope $\partial \log \hat{H}/\partial\lambda$ is 13 times its formal uncertainty. On both sides of the Oval BC ($\lambda = -30°$, $\lambda = -36°$), the magnitude of the slope is 2 times its formal uncertainty.

In estimating uncertainty, we assign a separate degree of freedom to each trajectory segment of length $2d$ — the width of the averaging box. This procedure is consistent with our model of the error discussed in Section 1.4, where we showed to a good approximation that the velocity vectors of Figs. 1.2 and 1.4 have uncorre-

TABLE 1.2

Absolute vorticity vs. latitude along trajectories.

Least-squares fit to (1.22) and (1.27):

$$\log\left[(\zeta + f)/f_o\right] = A\lambda^2 + B\lambda + C_j \qquad (1.22)$$

$$\left[(\zeta + f)/f_o\right] - 1 = A\lambda^2 + B\lambda + C_j \qquad (1.27)$$

Parameter	GRS		BC	
(j = trajectory)	(22)	(27)	(22)	(27)
A	11.06	13.16	82.72	82.46
B	5.93	7.61	96.60	96.40
C_a	0.314	0.693	27.93	27.94
C_b	0.343	0.710	27.76	27.81
C_c	0.523	0.865	27.93	27.93
C_d	0.545	0.892	28.14	28.12
C_e	0.546	0.914	28.13	28.13
C_f	0.529	0.913	28.21	28.18
C_g	0.587	0.918		
C_h	0.584	0.907		

Note: λ is planetographic latitude in radians ($\lambda < 0$), $f_o(-22.5°) = -1.35 \times 10^{-4}$ s^{-1} for the GRS, $f_o(-33°) = -1.92 \times 10^{-4}$ s^{-1} for the Oval BC.

FIGURE 1.17 : Results of least-squares fitting to the data of Fig. 1.14. The dots show the data in the form $C_j - \log|\zeta + f|$, the smooth curve is the fit to $-(A\lambda^2 + B\lambda)$, and the dashed curve is $-\log|f|$. The zero of the ordinate is arbitrary. Values of the constants A, B, and C_j as used here and in (1.22) are given in Table 1.2.

FIGURE 1.18 : As in Fig. 1.17 but for the White Oval BC.

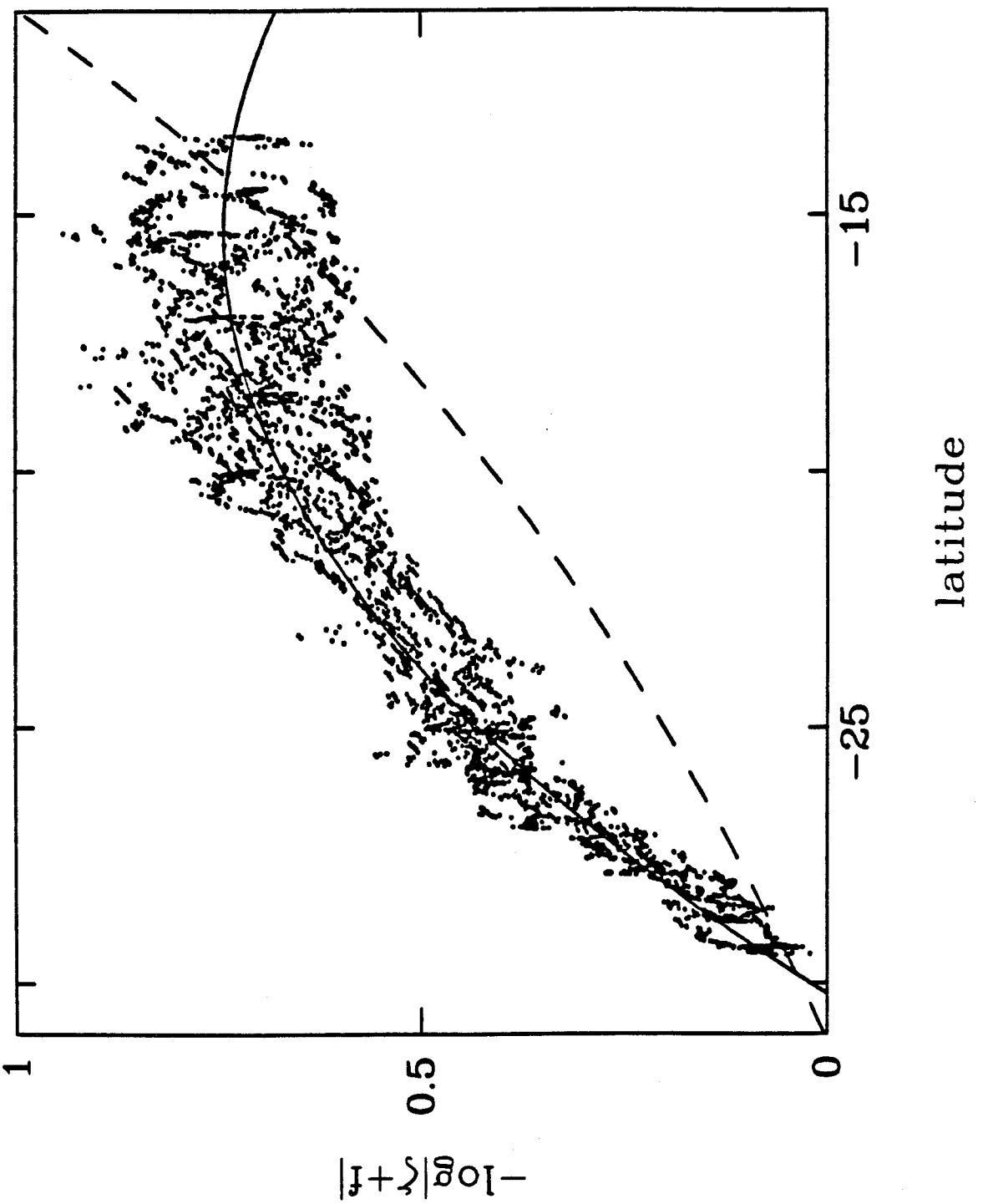
1
0.5
0
−log|ζ+f|
−15
−25
latitude

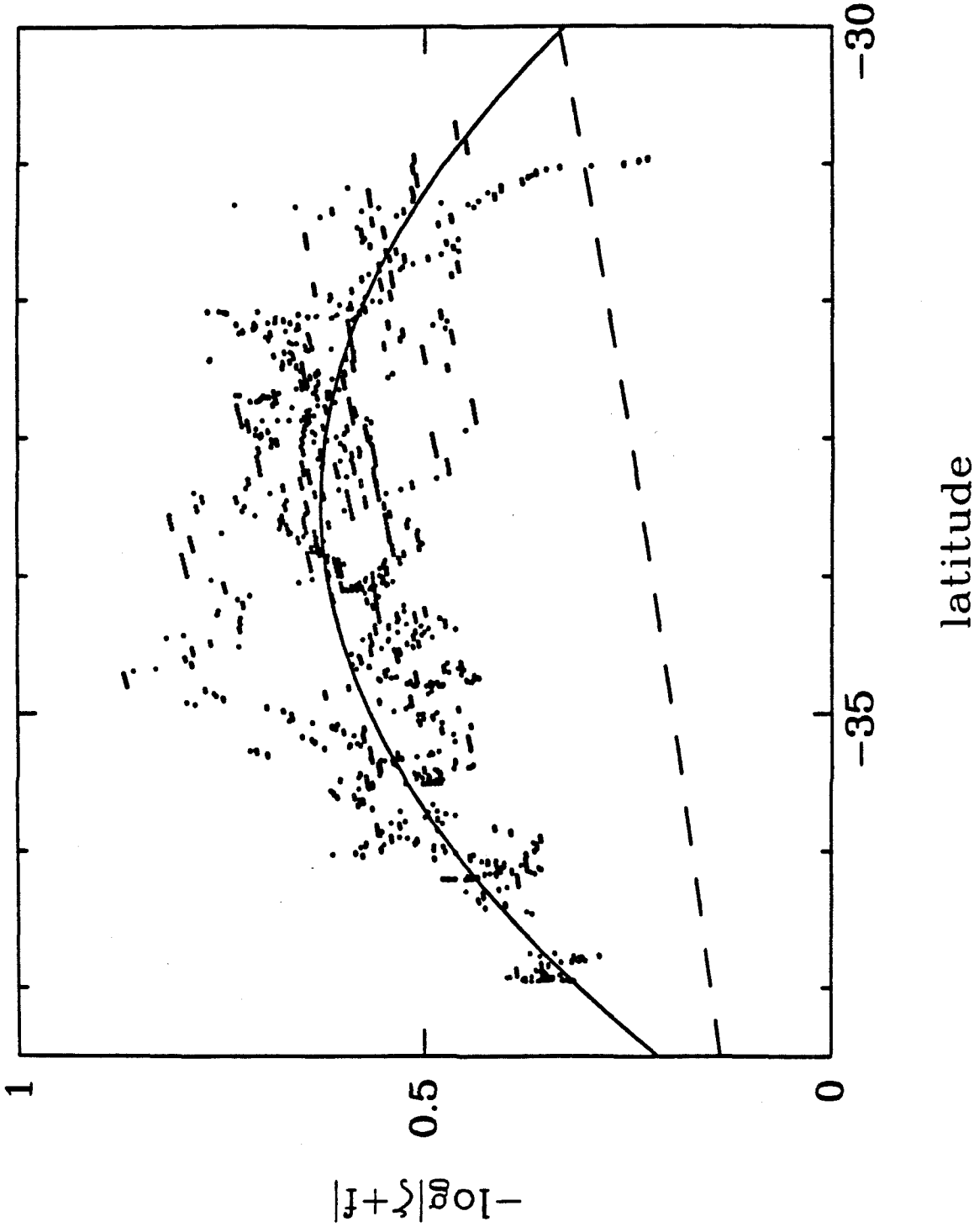
−30
−35
latitude
1
0.5
0
−log|ζ+f|

lated errors parallel to the local velocity. It follows for averaging boxes on the same trajectory that the autocorrelation of the residual of ζ falls linearly to zero as the distance between the box centers increases to $2d$. For averaging boxes on different trajectories, the correlation is small (≤ 0.25) or zero, when the separation between trajectories is either d, $2d$, or greater than $2d$. Since the separations in Figs. 1.13 and 1.15 are of order d, the errors from different trajectories are essentially uncorrelated. The residuals of the measured points in Figs. 1.14 and 1.16 are consistent with this model. That is, the equivalent width of the autocorrelation along a trajectory is of order $2d$, and the correlation from one trajectory to another is small.

Figures 1.14 and 1.16 show the results of the least-squares analysis in a somewhat different form. Here, the solid curves show $f_o \exp(A\lambda^2 + B\lambda + C_j)$. Each of these curves is proportional to the function $\hat{H}(\lambda)$. Although the magnitude of this function is undetermined, its shape is well determined and is an important result of this paper.

1.7 Quasi-Geostrophic Model

In this section we study the implications of our observations in the context of a one-layer, quasi-geostrophic (QG) model. The fluid has a free upper surface and rigid bottom topography that varies with latitude. The latter could represent either a curved solid surface, which is not a possibility for Jupiter's atmosphere, or a deep adiabatic fluid with a latitudinally varying zonal velocity. As we shall see, variable bottom topography is a required feature of the model if we are to fit the observed $(\zeta + f)$ variations. In fact, the bottom must be curved locally downward near the GRS and the Oval BC so as to match the data of Figs. 1.14 and 1.16 at their respective latitudes.

For the large–scale flow that we have observed around the GRS and the Oval BC,

the QG approximation is good only to the nearest 30 to 50 percent. Yet it fails rather uniformly. The three important terms in the vorticity equation — those involving ζ, f, and H — all vary smoothly across the vortices and all contribute about equally to the balance. There is no special balance between 2 out of the 3 terms. We believe the next step after a QG model is a primitive equation model, at least for these large ovals on Jupiter.

Support for the above statements comes from Table 1.2 and Figs. 1.14 and 1.16. The values of $\exp(C_j)$ from (1.22) indicate how much $(\zeta+f)$ varies from one trajectory to another at the same λ. The ratio between the minimum and maximum values of $\exp(C_j)$ is 0.76 for the GRS and 0.64 for the Oval BC. For comparison, the ratio of the minimum and maximum H's on the same trajectory is 0.45 for the GRS (trajectory d) and 0.55 for the Oval BC (trajectory c). And the ratio between the minimum and maximum $|f|$'s on the same trajectory is 0.55 for the GRS and 0.85 for the Oval BC. Not one of these numbers is particularly close to unity as required by the geostrophic approximation. But considering that these are extreme ratios (minimum to maximum), the QG approximation is useful at least in a semi-quantitative sense. The fact that the model has only one layer is an obvious deficiency. Modeling the phenomenon of baroclinic instability requires at least two vertical degrees of freedom, for instance. The model also requires that we neglect vertical shears in the horizontal wind. However, the *Voyager* infrared data (Gierasch *et al.*, 1986) suggest that vertical shears are small in the upper troposphere (a few scale heights for the vertical scale), so the problem may not be serious. The free-surface condition at the top is another deficiency. The rationale is that the pressure variation on a potential temperature surface in the stably stratified upper troposphere is small. In the lower troposphere where pressure is large and the static stability is small, the pressure variation on a potential temperature surface is large. The intervening layer should have a constant-

pressure (stress-free) condition at the upper surface and a variable pressure at the lower surface. These problems in applying layer models to atmospheric flows are well known in terrestrial meteorology and are beyond the scope of this paper. The one-layer QG model with topography is at least a familiar one (e.g., Pedlosky, 1987, Sections 3.12 and 3.13), and has the minimum complexity needed to fit our potential vorticity data.

The QG vorticity equation for a single upper layer supported hydrostatically on a much deeper lower layer is

$$\frac{d}{dt}(\nabla^2\psi + f - k^2\psi + k^2\psi_2) = 0 \quad . \tag{1.23}$$

The dependent variable is the upper-layer streamfunction $\psi(x, y, t)$, with velocities $u = -\partial\psi/\partial y$ and $v = \partial\psi/\partial x$. The equation was derived by Ingersoll and Cuong (1981), who used the notation $\overline{\psi}$ in place of ψ_2. The model differs from standard QG models only in the term $k^2\psi_2$, where $\psi_2(y)$ is the streamfunction of the zonal flow $u_2(y)$ in the lower layer. This term is absent when the lower layer is motionless with respect to the rotating coordinates or when the upper layer is supported by a solid surface, which is horizontal in the rotating system. In general, ψ_2 could be a function of x, y and t, but our data suggest $\psi_2 = \psi_2(y)$. The terms in (1.23) are the QG vorticity $\zeta = \nabla^2\psi$, the Coriolis parameter $f = f_o + \beta y$, a term $-k^2\psi$ from the free-surface condition $P = 0$, and the term $k^2\psi_2$ from the condition that P be continuous across the lower interface. The constant k^2 is given by

$$k^2 \equiv \frac{1}{L_D^2} = \frac{f_o^2}{gH_o}\left(1 - \frac{\rho_1}{\rho_2}\right)^{-1} \quad , \tag{1.24}$$

where L_D is the radius of deformation, g is the gravitational acceleration, H_o is the mean thickness of the upper layer, ρ_1 is its density, and ρ_2 is the density of the lower layer ($\rho_2 > \rho_1$). Because the lower layer is so much thicker than the upper layer, there is no feedback of upper layer motions on the lower layer dynamics. Thus, if $\psi_2(y)$ is initially constant, it will remain so.

In the QG approximation, the thickness variations along trajectories arise exclusively from motions in the deep lower layer. To show this, we use the reference frame of the vortex where the flow is steady. Then (1.23) has a first integral

$$(\nabla^2\psi + f - k^2\psi + k^2\psi_2) = F(\psi) \quad . \tag{1.25}$$

This can be written

$$(\zeta + f) = -k^2\psi_2(y) + G(\psi) \quad , \tag{1.26}$$

where $G(\psi) = F(\psi) + k^2\psi$. Steady trajectories are lines ψ = constant. Therefore, the curves in Figs. 1.14 and 1.16 showing $(\zeta + f)$ vs. latitude on different trajectories are the QG approximation to $-k^2\psi_2$, where ψ_2 is the lower-layer streamfunction in the reference frame of the vortex. The fact that the large–scale derivatives of the $(\zeta + f)$ curves in Figs. 1.14 and 1.16 depend much more on latitude than on longitude implies that ψ_2 is a function of y only, to a good approximation.

Exactly the same argument as the step from (1.25) to (1.26) is made by Pedlosky (1987), Section 3.13. To quote: "Each fluid element preserves its value of ψ and hence experiences no tube stretching due to the upper surface, which could, as far as the dynamics is concerned, be flat. Note that the vortex tubes will be stretched if fluid crosses isolines of η_B." In Pedlosky's notation η_B is a scaled measure of the bottom elevation from a constant reference value. The scaling factor is proportional to f_o, which changes sign at the equator. In the southern hemisphere the bottom elevation varies directly as $-k^2\psi_2$. Equation (1.26) therefore offers a simple physical analogy for Figs. 1.14 and 1.16, which resemble altitude–latitude cross sections of an ocean with variable bottom topography. The top of the ocean is the horizontal line $(\zeta + f) = 0$. The bottom of the ocean is the measured $(\zeta + f)$ curve, which is negative and therefore represents the altitude of the bottom with respect to sea level. Where the measured curve reaches a maximum, as it does once at $\lambda = -16°$ and

again at $\lambda = -33.5°$, the bottom elevation is large and the thickness (depth) is small. As shown in the next section, this washboard topography has an important effect on the dynamics.

Equation (1.26) is the QG analogue of (1.22). To make the analogy as close as possible we rewrite (1.26) in the form

$$\frac{\zeta + f}{f_o} - 1 = A\lambda^2 + B\lambda + C_j \quad . \tag{1.27}$$

Equations (1.22) and (1.27) become equal as $(\zeta + f)$ approaches f_o. The constants A, B, and C_j of (1.27) are determined from the data by the method of least squares. These constants are listed in Table 1.2 for comparison with those of (1.22). Our estimate of $-k^2\psi_2$ is then given by the expression $f_o(A\lambda^2 + B\lambda)$.

According to (1.26), where $(\zeta + f)$ slopes upward to the right (λ or y increasing), the zonal flow in the lower layer is positive ($u_2 = -\partial\psi_2/\partial y$), and vice versa. Figure 1.14 shows that u_2 is eastward (positive) on the poleward side of the GRS and weak or westward (negative) on the equatorward side. Similarly, Fig. 1.16 shows that u_2 is eastward on the poleward side of the Oval BC and westward on the equatorward side. In these respects, the zonal flow in the lower layer resembles that in the upper layer.

One major result of this study is that the lower layer is in differential rotation — zonal velocity varies with latitude. If the rotation of the lower layer were uniform and if the vortex drifted westward, the velocity $u_2 = -\partial\psi_2/\partial y$ would be a positive constant. The $(\zeta + f)$ profiles in Figs. 1.14 and 1.16 would then be straight lines sloping upward to the right. The fact that the observed $(\zeta + f)$ profiles are curved implies that the lower layer is not rotating uniformly.

The magnitude of u_2 is of order $\beta {L_D}^2$, according to Fig. 1.14, which suggests that $-k^2\, d\psi_2/dy$ is of order df/dy. Ingersoll and Cuong (1981) point out that L_D (the same as k^{-1}) could have any value in the range from 500 to 5000 km. The wide

range reflects the uncertainty in $\Delta\theta$, where $\Delta\rho/\rho \sim \Delta\theta/\theta$ is the fractional potential temperature difference over one scale height ($H_0 \sim R_g\theta/g$), R_g is the gas constant, and ${L_D}^2$ is $R_g\Delta\theta/{f_0}^2$ from (1.24). These estimates give u_2 in the range from 1 to 100 $\mathrm{m\,s^{-1}}$, which is not a very useful result. However, the effect of u_2 on the upper-layer dynamics is a well-measured quantity given by the term $k^2\psi_2$ in (1.23).

1.8 Rossby Wakes

The above observational results are generally consistent with the model of Ingersoll and Cuong (1981), who postulated that the lower-layer flow was exactly equal to the upper-layer flow far to the east or west of the vortex. The additional requirement $k^2L^2 > 1$, where L is the radius of curvature of the zonal velocity profile, then made the far field of the vortex decay exponentially to zero (Ingersoll and Cuong, p. 2070, second column). Exponential decay in x and y ensures that the vortex is compact. In contrast, oscillatory behavior in x and y allows the vortex to radiate energy in a standing Rossby wave (Rossby wake) that extends far downstream. Ingersoll and Cuong were looking for stable, compact vortices in their numerical model, so they favored the kind of topography that would give exponential decay. In this paper we will be guided by the data. Given that the solid curves of Figs. 1.14 and 1.16 are QG approximations to $-k^2\psi_2$, we shall examine the implications for vortex structure, using (1.23) and (1.26).

The $k^2\psi_2(y)$ term adds a washboard topography to the usual β–plane dynamics. If we linearize (1.23) about a steady zonal flow $\overline{u}(y)$ in the upper layer, we obtain for the perturbation streamfunction ψ' in the upper layer

$$\nabla^2\psi' + \left(\frac{\beta - \overline{u}_{yy} - k^2u_2}{\overline{u}}\right)\psi' = 0 \quad . \tag{1.28}$$

The flow is assumed to be steady in the reference frame of the vortex. Both $\overline{u}$ and u_2 are measured relative to that frame. Solutions are wavelike or exponential, depending on whether the bracketed term is positive or negative.

According to observations, the $k^2 u_2$ term is just as large as β and as $\overline{u}_{yy}$. From (1.26) and the fact that $u_2 = -\partial\psi_2/\partial y$, the numerator in (1.28) can be written

$$\frac{\partial}{\partial y}(\overline{\zeta} + f) - \frac{\partial}{\partial y}(\hat{\zeta} + f) \equiv \frac{\partial q}{\partial y} \quad . \tag{1.29}$$

Here, $\overline{\zeta} = -\overline{u}_y$ is the vorticity of the zonal flow in the upper layer at large distances from the vortex, and $\hat{\zeta}$ is the vorticity measured along trajectories, the ζ part of $(\zeta + f)$ plotted in Figs. 1.14 and 1.16. According to (1.28), where $\overline{u} > 0$ (eastward flow in the upper layer relative to the vortex), solutions in the far field will be exponential provided $\partial q/\partial y < 0$. Where $\overline{u} < 0$, solutions will be exponential, provided $\partial q/\partial y > 0$.

Figures 1.19 and 1.20 show $(\overline{\zeta} + f)$ and $(\hat{\zeta} + f)$ for the GRS and the Oval BC, respectively. The data of Limaye (1986) were used for $\overline{\zeta}$, although the data of Ingersoll *et al.* (1981) give the same results. Zonal velocities at 15 adjacent latitudes in Limaye's Table 1.1 were fitted to quadratic functions. Vorticity was then computed from (1.5). The fit to (1.27) was used for $\hat{\zeta}$, although (1.22) gives the same results. The vertical lines in Figs. 1.19 and 1.20 show latitudes where $\overline{u}$ changes sign from eastward to westward. At latitudes where $\overline{u} > 0$, (1.28) has exponential solutions, if the heavy curves $(\hat{\zeta} + f)$ slope upward to the right more strongly than the light curves $(\overline{\zeta} + f)$. This condition is satisfied on the poleward side of the Oval BC ($-35° > \lambda > -37°$) and is marginally satisfied on the poleward side of the GRS ($-23.5° > \lambda > -29°$). At latitudes where $\overline{u} < 0$, (1.28) has exponential solutions if the heavy curves $(\hat{\zeta} + f)$ slope downward to the right more strongly than the light curves $(\overline{\zeta} + f)$. This condition is marginally satisfied on the equatorward side of the Oval BC ($-31° > \lambda > -35°$) and is violated on the equatorward side of the GRS ($-16° > \lambda > -23.5°$).

The above statements need some qualification. The light curves exhibit more

FIGURE 1.19 : Comparison of absolute vorticity variations along trajectories (this work) with zonal mean absolute vorticities in the vicinity of the GRS. The heavy curve is $(\hat{\zeta} + f)$ as given by (1.27) and Table 1.2. The light curve is $(\overline{\zeta} + f)$, computed from the high-resolution, zonal velocity profile of Limaye (1986). The vertical dotted lines indicate the zeros of zonal velocity in the GRS frame. The circles with dots indicate zonal velocities out of the page (eastward), and the circle with a cross indicates velocities into the page (westward). The zero of the ordinate for the heavy curve is arbitrary.

FIGURE 1.20 : As in Fig. 1.19 but for the White Oval BC.

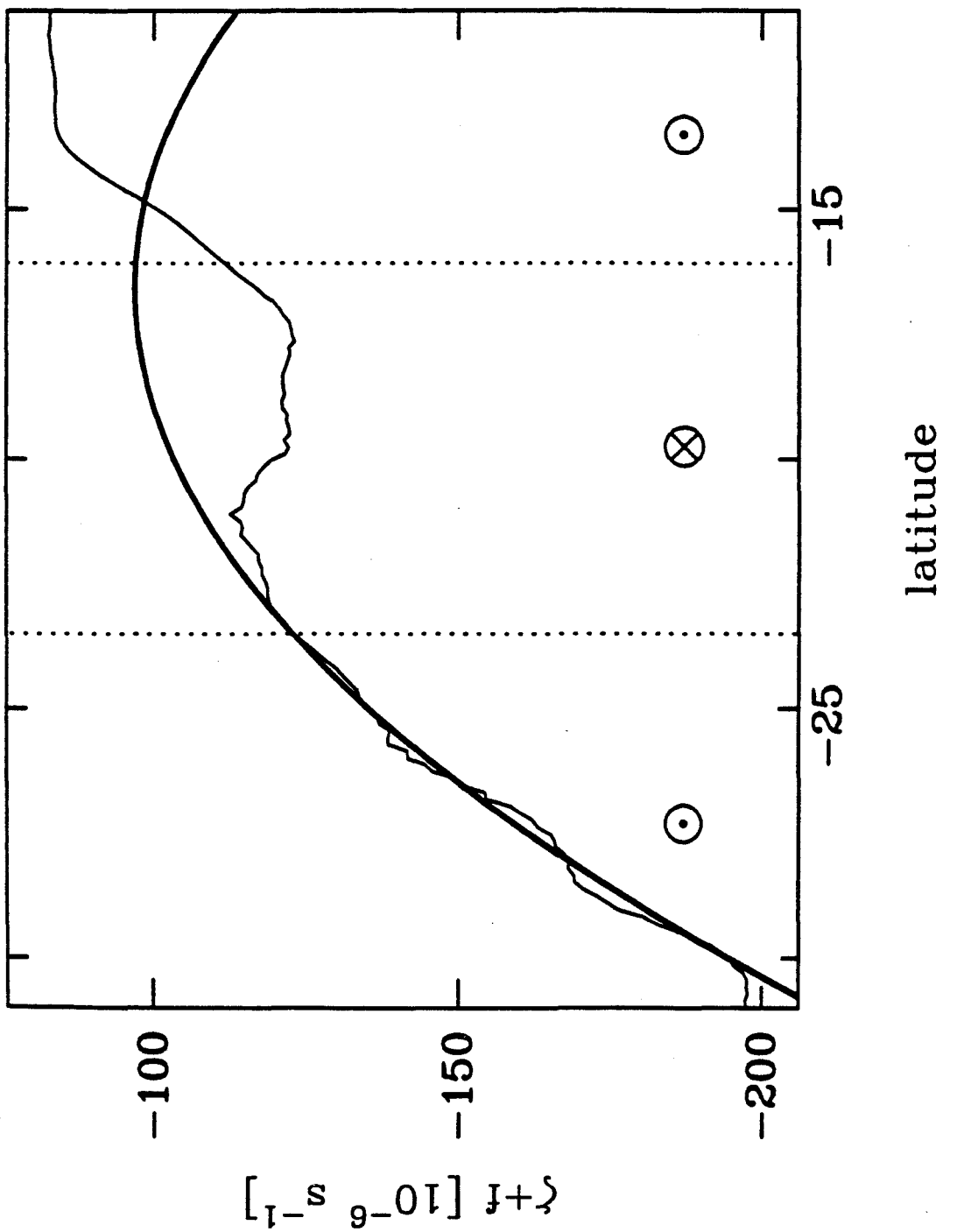
−100
−150
−200
ζ+f [10⁻⁶ s⁻¹]
−15
−25
latitude

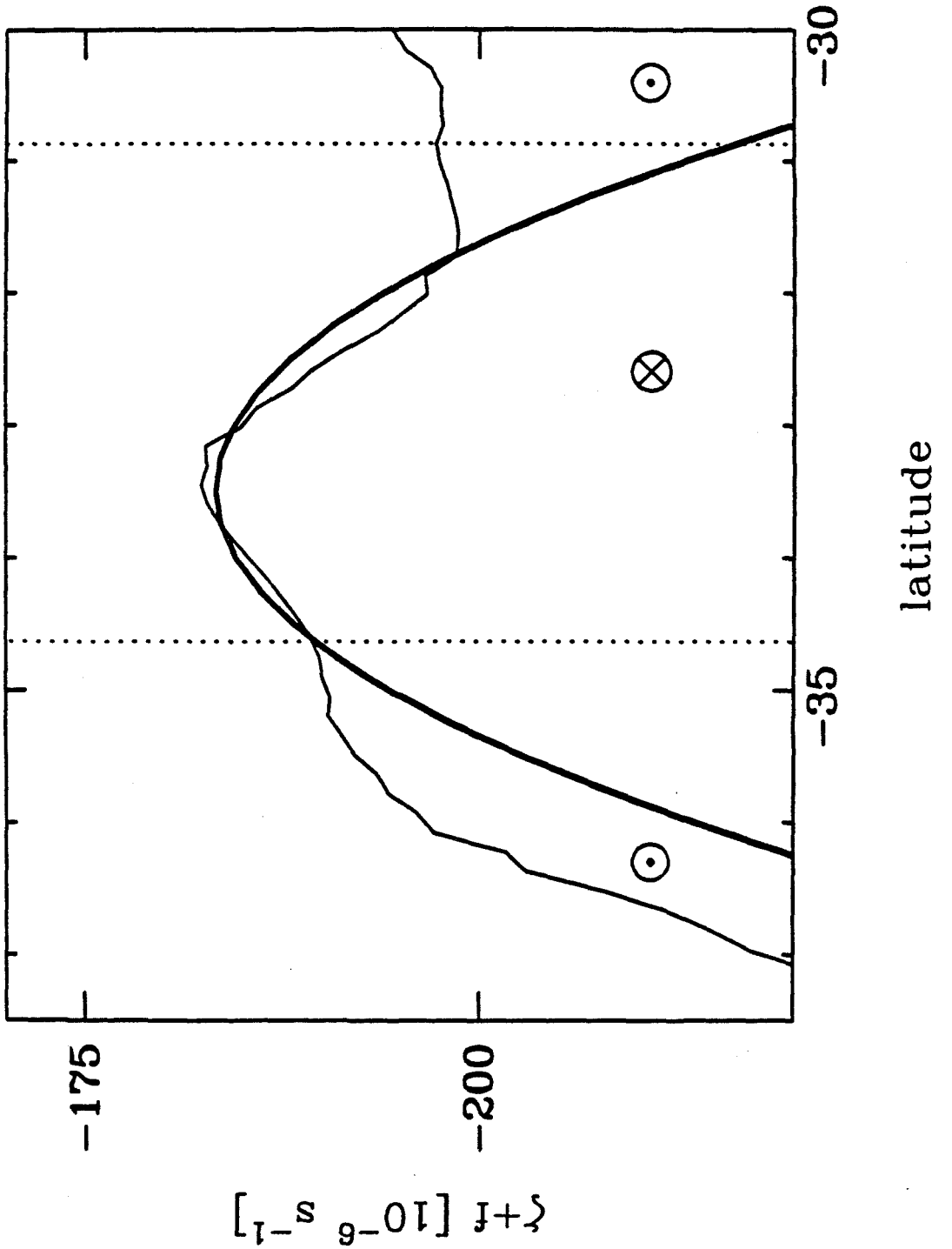
−30
−35
latitude
−175
−200
ζ+f [10⁻⁶ s⁻¹]

detail than the solid curves, largely because the measurement of $(\overline{\zeta} + f)$ allows more detail than that of $(\hat{\zeta} + f)$. Thus, it is possible that a negative slope $[(\zeta + f)/\partial\lambda < 0]$ like that exhibited by the $(\overline{\zeta} + f)$ curve (Fig. 1.19) at $(-17^{\circ} > \lambda > -21^{\circ})$ is hidden in the noise of the fit to the smooth $(\hat{\zeta} + f)$ curve (Fig. 1.17). Comparison with Fig. 1.14 shows, however, that $\partial(\hat{\zeta} + f)/\partial\lambda$ is positive at $(-16^{\circ} > \lambda > -21^{\circ})$ for all trajectories except possibly for the left portion of trajectory h. Whether the exception is significant or not requires more data from the turbulent region to the west and north of the GRS, where the left portion of trajectory h originates.

The observations are consistent with the basic idea of Ingersoll and Cuong that a nonuniform zonal flow in the deep lower layer affects the upper layer dynamics. Some quantitative features of their model are also consistent with observation. The way topography dominates over β on the poleward sides of the GRS and the Oval BC is a good example. With the proper choice of k^2, the zonal flow in the lower layer could be set equal to $\overline{u}$ in this region. However, the agreement is not good on the equatorward sides. For example, the band from $-16°$ to $-23.5°$ is characterized by strong westward flow (relative to the GRS) in the upper layer, as observed in *Voyager* images. The topography we have inferred implies an eastward flow (relative to the GRS) in the lower layer at these latitudes. This is seen in Fig. 1.14 from the smooth curves, which are proportional to $-k^2\psi_2(y)$, according to (1.26). The fact that the curves slope upward to the right $(u_2 = -\partial\psi_2/\partial y > 0)$ in the latitude band $-16° > \lambda > -23.5°$ implies that the deep zonal flow is eastward. This disagreement suggests that the GRS and the Oval BC are not as compact as postulated by Ingersoll and Cuong.

According to the above qualitative analysis of (1.28), the westward flow on the equatorward side of the GRS is the one most likely to have a wake. Certainly, the filamentary regions (FR's) to the west and north of the GRS and other Southern

Hemisphere ovals are wakelike. The FR's are extensive turbulent patches that extend downstream (westward) to distances of ten or more semimajor diameters (Smith *et al.*, 1979a,b; Ingersoll *et al.*, 1979; Mac Low and Ingersoll, 1986). Perhaps they are Rossby wakes, and perhaps they are an important part of the dynamics of the long-lived ovals. If the vortices are rapidly losing energy through the wakes, then there must be an equal source of energy. A more complete analysis with a more accurate model should help answer these questions.

Acknowledgements. We thank Glenn Flierl for helpful suggestions made while one of us (A.I.) was participating in the Summer Study Program in Geophysical Fluid Dynamics at the Woods Hole Oceanographic Institution. We thank Glenn Garneau and Reta Beebe for helping to prepare the data and two anonymous referees for their helpful suggestions. This research was supported by the Planetary Atmospheres Program of NASA and by *Voyager* Project funds.

1.9 References

Beebe, R.F., A.P. Ingersoll, G.E. Hunt, J.L. Mitchell, and J.P. Müller, 1980. Measurements of wind vectors, eddy momentum transports, and energy conversions in Jupiter's atmosphere from Voyager 1 images. *Geophys. Res. Lett.* **7**, 1–4.

Ertel, H., 1942. Ein neuer hydrodynamics cher Wirbelsatz.. *Meteor. Z.*, **59**, 277–281..

Gierasch, P.J., B.J. Conrath, and J.A. Magalhães, 1986. Zonal mean properties of Jupiter's upper troposphere from Voyager infrared observations. *Icarus* **67**, 456–483.

Haltiner, G.J. and R.T. Williams, 1980. *Numerical Prediction and Dynamic Meteorology.* John Wiley and Sons, New York.

Hatzes, A., D.D. Wenkert, A.P. Ingersoll, and G.E. Danielson, 1981. Oscillations and velocity structure of a long–lived cyclonic spot. *J. Geophys. Res.* **86**, 8445–8449.

Holton, J.R., 1979. *An Introduction to Dynamic Meteorology.* Academic Press, New York.

Ingersoll, A.P., R.F. Beebe, S.A. Collins, G.E. Hunt, J.L. Mitchell, P. Müller, B.A. Smith, and R.J. Terrile, 1979. Zonal velocity and texture in the Jovian atmosphere inferred from Voyager images. *Nature* **280**, 773–775.

Ingersoll, A.P. and P.G. Cuong, 1981. Numerical model of long–lived Jovian vortices. *J. Atmos. Sci.* **38**, 2067–2076.

Ingersoll, A.P., R.F. Beebe, J.L. Mitchell, G.W. Garneau, G.M. Yagi, and J.-P. Müller, 1981. Interaction of eddies and mean zonal flow on Jupiter as inferred from Voyager 1 and 2 images. *J. Geophys. Res.* **86**, 8733–8743.

Ingersoll, A.P., R.F. Beebe, B.J. Conrath, and G.E. Hunt, 1984. Structure and dynamics of Saturn's atmosphere. In *Saturn* (T. Gehrels and M.S. Matthews,

eds.) Univ. of Arizona Press, Tucson.

Limaye, S.S., H.E. Revercomb, L.A. Sromovsky, R.J. Krauss, D. Santek, V.E. Suomi, S.A. Collins, and C.C. Avis, 1982. Jovian winds from Voyager 2. Part 1: Zonal mean circulation. *J. Atmos. Sci.* **39**, 1413–1432.

Limaye, S.S., 1986. Jupiter: New estimates of the mean zonal flow at the cloud level. *Icarus* **65**, 335–352.

Mac Low, M.-M. and A.P. Ingersoll, 1986. Merging of vortices in the atmosphere of Jupiter: An analysis of Voyager images. *Icarus* **65**, 353–369.

Mitchell, J.L., R.F. Beebe, A.P. Ingersoll, and G.W. Garneau, 1981. Flow fields within Jupiter's Great Red Spot and White Oval BC. *J. Geophys. Res.* **86**, 8751–8757.

Pedlosky, J., 1987. *Geophysical Fluid Dynamics, Second Edition*. Springer–Verlag, New York.

Smith, B.A. and G.E. Hunt, 1976. Motions and morphology of clouds in the atmosphere of Jupiter. In *Jupiter* (T. Gehrels, Ed.) Univ. of Arizona Press, Tucson.

Smith, B.A., L.A. Soderblom, T.V. Johnson, A.P. Ingersoll, S.A. Collins, E.M. Shoemaker, G.E. Hunt, H. Masursky, M.H. Carr, M.E. Davies, A.F. Cooke II, J. Boyce, G.E. Danielson, T. Owen, C. Sagan, R.F. Beebe, J. Veverka, R.G. Strom, J.F. McCauley, D. Morrison, G.A. Briggs, and V.E. Suomi, 1979a. The Jupiter system through the eyes of Voyager 1. *Science* **204**, 951–972.

Smith, B.A., R. Beebe, J. Boyce, G. Briggs, M. Carr, S.A. Collins, A.F. Cooke II, G.E. Danielson, M.E. Davis, G.E. Hunt, A. Ingersoll, T.V. Johnson, H. Masursky, J. McCauley, D. Morrison, T. Owen, C. Sagan, E.M. Shoemaker, R. Strom, V.E. Suomi, and J. Veverka, 1979b. The Galilean satellites and Jupiter: Voyager 2 imaging science results. *Science* **206**, 927–950.

Sromovsky, L.A., H.E. Revercomb, V.E. Suomi, S.S. Limaye, and R.J. Krauss,

1982. Jovian winds from Voyager 2. Part II: Analysis of eddy transports. *J. Atmos. Sci.* **39**, 1433–1445.

Yagi, G., J. Lorre, and P. Jepsen, 1978. Dynamic feature analysis for Voyager at the Image Processing Laboratory. *Proceedings of the Conference on Atmospheric Environment of Aerospace Systems and Applied Meteorology.* Nov. 15–17, 1978, American Meteorological Society, Boston, Mass.

Paper 2

Jupiter's Great Red Spot as a Shallow Water System

In a few minutes more, there came over the scene another radical alteration. The general surface grew somewhat more smooth, and the whirlpools, one by one, disappeared, while prodigious streaks of foam became apparent where none had been seen before. These streaks, at length, spreading out to a great distance, and entering into combination, took unto themselves the gyratory motion of the subsided vortices, and seemed to form the germ of another more vast. Suddenly—very suddenly—this assumed a distinct and definite existence, in a circle of more than half a mile in diameter. The edge of the whirl was represented by a broad belt of gleaming spray; but no particle of this slipped into the mouth of the terrific funnel, whose interior, as far as the eye could fathom it, was a smooth, shining, and jet-black wall of water, inclined to the horizontal at an angle of some forty-five degrees, speeding dizzily round and round with a swaying and sweltering motion, and sending forth to the winds an appalling voice, half shriek, half roar, such as not even the mighty cataract of Niagara ever lifts up in its agony to Heaven.

—Edgar Allan Poe, *A Descent into the Maelström*

Jupiter's Great Red Spot as a Shallow Water System

Timothy E. Dowling and Andrew P. Ingersoll

Division of Geological and Planetary Sciences

California Institute of Technology

Pasadena, California 91125

Submitted to: *Journal of the Atmospheric Sciences*

October 14, 1988

Contribution number 4717 from the Division of Geological and Planetary Sciences, California Institute of Technology, Pasadena, California 91125.

Abstract

Most models of Jupiter's Great Red Spot (GRS) are cast in terms of the so-called 1-1/2 layer model, where a thin upper weather layer, which contains the vortex, overlies a much deeper layer, which is meant to represent the neutrally stratified deep atmosphere. Any motions in the deep layer are assumed to be zonal and steady, and result in meridional topography at the fluid layer interface. Specifying the deep motions or lack thereof is equivalent to specifying the bottom topography of the upper layer, and hence the far-field potential vorticity. Current models of the GRS start by guessing the deep motions and then proceed to study vortices, using the implied bottom topography. Here, using the GRS cloud-top velocity data, we *derive* the bottom topography up to a constant that depends on the unknown radius of deformation. We employ the same 1-1/2, layer shallow water (SW) equations as in the current models. We start by calculating the Bernoulli streamfunction B from the velocity field, which is observed to be nearly steady in the reference frame of the vortex. We also calculate the kinetic energy per mass K and the absolute vertical vorticity $(\zeta + f)$. The bottom topography gh_2 is related to the observations by $gh_2 = B - K - (\zeta + f)/q$, where the potential vorticity q is the only unknown. We model q as some function $q(B)$ and the bottom topography as some function of latitude. The procedure is to specify $q = q_0$ on $B = B_0$, and then solve by least squares for gh_2 and for q. The results show that the deep atmosphere is in differential motion and that the far-field potential vorticity is not uniform. Numerical SW experiments are performed using both the derived bottom topography and the bottom topography prescribed by current models. The results of three published studies are reproduced in our numerical experiments. Each of these models is successful in maintaining a long-lived, isolated vortex, but only the present model yields $(\zeta + f)$ profiles along streamlines that agree with those observed for the GRS by Dowling and Ingersoll (*J.*

Atmos. Sci., 1988). A model run that starts with the derived bottom topography and observed zonally-averaged, cloud-top winds produces several vorticies. These merge over time to form a single, long-lived vortex, closely resembling the GRS. The system is unstable, leading naturally to the genesis and maintenance of vortices. Without forcing, the upper-layer velocity field tends to smooth out with time. How the cloud-top winds on Jupiter are maintained in an unstable state is a crucial, unanswered question.

2.1 Introduction

The wealth of data returned by the *Voyager* spacecraft encounters of Jupiter in 1979 makes it possible for the first time to study that planet's historically fascinating Great Red Spot (GRS) without specifying *a priori* the motions in the deep atmosphere. The dynamics of the GRS are coupled to the dynamics of the deep atmosphere, and the cloud-top motions in the GRS and other ovals can be used to probe the underlying fluid motions.

Progress in this direction will be made by using a model atmosphere that drastically simplifies the vertical structure. We will consider the so-called 1-1/2 layer model, where a thin upper weather layer, which contains the vortex, overlies a much deeper layer, which is meant to represent the convectively adjusted, neutrally stratified deep atmosphere. The model layers are governed by the shallow water (SW) equations. The SW system is described in detail in Sec 2.2. The lower layer is assumed to be much deeper than the upper layer and is therefore not affected by the upper-layer dynamics (hence the name "1-1/2 layer"). Any motions in the deep layer are assumed to be zonal and steady. This system may be reduced to a 1-layer system with meridionally varying solid bottom topography. Specifying the deep motions or lack thereof is equivalent to specifying the bottom topography, and hence the potential vorticity of the upper layer in the far field, that is, far to the east or west of the vortex.

Most current models of the GRS start by making an assumption about the deep motions, and then proceed to study vortices in a 1-1/2 layer model, using the implied bottom topography. Ingersoll and Cuong (1981, hereafter IC81) assume that the deep motions are equal to the far-field motions in the upper layer. Williams and Yamagata (1984, hereafter WY84) and Williams and Wilson (1988, hereafter WW88) assume that the deep layer is in solid body rotation. Marcus (1988, hereafter M88) assumes that the far-field potential vorticity is constant. The various bottom topographies

prescribed by these models will be discussed in Sec. 2.3. The work on baroclinic eddies and the GRS by Read and Hide (1983, 1984) is not cast in terms of a 1-1/2 layer model and will not be directly addressed here.

Instead of guessing the deep motions, in this work we *derive* the bottom topography, up to a constant that depends on the unknown radius of deformation. We use the *Voyager* cloud-top wind data for the GRS and White Oval BC, and make the same 1-1/2 layer assumptions as in the models above. Our method of inverting the cloud-top wind data to get the bottom topography is described in Sec. 2.3. The present approach differs from that of Dowling and Ingersoll (1988, hereafter DI88), who used the quasi-geostrophic approximation to derive the deep-layer zonal velocity profile. The SW equations used here are more general, and include the quasi-geostrophic approximation as a special case. By assuming that the deep winds are steady and zonal, we make the simplest possible assumption that fits the cloud-top wind data. This assumption includes solid-body rotation of the deep layer as a special case. Our long-range goal is to apply the *Voyager* data to multilayer models like that of Read and Hide. In these cases it may be more difficult to infer the zonal velocity, or the corresponding bottom topography, of the deepest layers.

Once we have deduced the bottom topography for a 1-1/2 layer SW model of the GRS, we study the system numerically. Our SW numerical scheme is outlined in Sec. 2.4. We will refer to the derived bottom topography by the label DI89, and the prescribed bottom topographies of Ingersoll and Cuong, Williams and Yamagata, and Marcus by the labels IC81, WY84, and M88, respectively. (The Williams and Wilson bottom topography is equivalent to WY84.) We initialize our runs with the observed zonally averaged, cloud-top velocity profile as determined by Limaye (1986). The numerical code is set in oblate spherical geometry. In Sec. 2.5 we present three types of numerical experiments: i) model comparisons, ii) longevity, and iii) genesis

of an isolated vortex. To compare models we make parallel runs, starting with an initial vortex, which differ only in bottom topography. The same Lagrangian vorticity analysis performed on the GRS data by DI88 is performed on the model vortices, and the resulting absolute vorticity $(\zeta + f)$ profiles are compared with those for the GRS. Only the DI89 bottom topography yields $(\zeta + f)$ profiles that agree with observations. In many experiments we force the zonal flow towards the observed, cloud-top wind profile on a time scale of 400 days. With the DI89 bottom topography this profile is unstable, and if forced, continuously produces small eddies at the latitude of the GRS. In the longevity experiment, we run a DI89 vortex at full resolution for over ten years. The large vortex maintains itself by absorbing the constant supply of smaller eddies.

In the genesis experiment, we add a small sinusoidal perturbation to the system initialized with the observed zonally-averaged, cloud-top wind profile and DI89 bottom topography. Several small vortices emerge and then coalesce, until a single large vortex remains and persists.

In Sec. 2.6, we state our conclusions and point to future work. One important result from this work is a determination of the deep-layer zonal wind profile underneath the GRS and White Oval BC, up to essentially a multiplicative constant, which depends on the unknown radius of deformation. Another important conclusion is that given a SW system with a zonal velocity field that is continuously forced towards an unstable profile, the emergence and persistence of large, isolated vortices occurs naturally. How the cloud-top winds on Jupiter are maintained in an unstable state then becomes a crucial, unanswered question.

2.2 Shallow Water Model

It is important to keep in mind the detail and complexity of Jupiter's atmosphere when attempting to model objects like the GRS. Figure 2.1 shows a visual image of Jupiter's cloud tops constructed from *Voyager 1* photographs. The GRS is the largest vortex, centered at about longitude $\phi = 72°$, latitude $\lambda = -22°$. An even larger permanent feature is the turbulent patch directly to the northwest of the GRS, an example of a so-called filamentary region (Ingersoll, *et al.*, 1979; Mac Low and Ingersoll, 1986). The lifetime of individual features within this region is short — a few days to a week. No model of the GRS to date shows a filamentary region. To successfully model such a feature, we expect that the deep motions must be accurately represented. Convective activity, which is beyond the capabilities of the SW model studied here, also appears to play a role in the filamentary regions. Another important observation associated with the GRS is the perpetual existence of several small eddies in the same shear flow as the GRS. Over one dozen small eddies can be seen in Fig. 2.1 at about latitude $\lambda = -22°$. These eddies are often seen to merge with the GRS. We will return to this point when studying the time evolution of numerical models of the GRS's shear flow in the case where the flow is unstable. Also seen in Fig. 2.1 are the three White Ovals at about latitude $\lambda = -33°$, and the many other intriguing features of Jupiter's cloud tops. For a complete discussion of the cloud features in Fig. 2.1, see Smith *et al.* (1979 a,b).

We treat the GRS as a shallow feature. *Voyager* infrared observations have yielded temperature fields above the 500 mb level of the cloud tops, which through application of the thermal wind equation imply a decay of wind strength with height above the clouds (Flasar *et al.*, 1981). The thickness of the GRS from the cloud tops upward is on the order of 100 km. The thickness of the GRS below the cloud tops is a major unknown. We assume that it does not penetrate significantly into the neutrally

FIGURE 2.1 : Visual image of Jupiter's cloud tops. This is a cylindrical mosaic made from *Voyager 1* images, labeled by planetographic latitude and System III longitude. (Note that longitude increases westward in *Voyager* images and data, but we will use eastward-increasing longitude in equations and numerical models.) The Great Red Spot (GRS) is the large vortex centered at longitude $\phi = 72°$, latitude $\lambda = -22°$. The GRS's filamentary region is the large turbulent patch directly to the northwest of the GRS. Notice that there are over one dozen smaller vortices in the same shear flow as the GRS. The three White Ovals are centered at longitudes $\phi = 5°$, $85°$, and $170°$, and latitude $\lambda = -33°$. For a complete description of Jupiter's cloud features see Smith *et al.* (1979a, b).

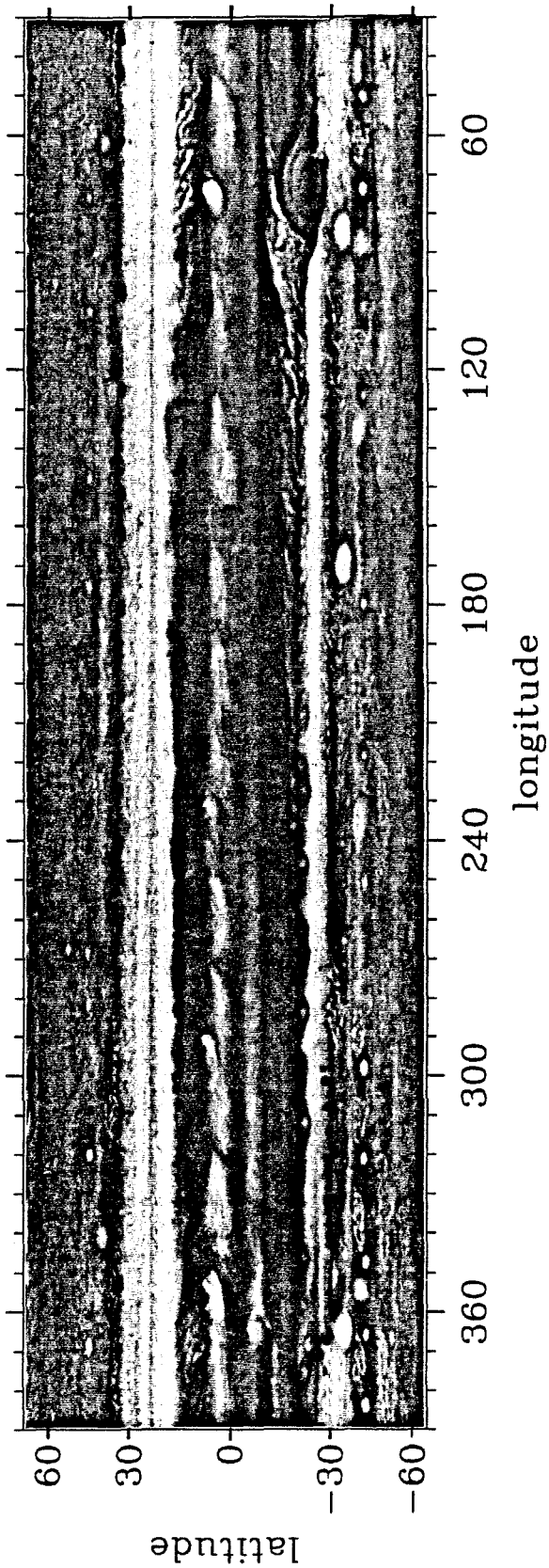
60
30
0
−30
−60
latitude
60
120
180
240
300
360
longitude

stratified deep atmosphere, which begins on the order of 100 km below the cloud tops. For a discussion of the deep interiors of Jovian planets see Stevenson (1982). Since the GRS covers 20,000 km in longitude, we therefore expect about a 100-to-1 ratio in horizontal to vertical dimensions. For more details see the reviews on Jovian atmospheres by Ingersoll *et al.* (1984) and Flasar (1986).

In order to make progress with limited vertical information, we must drastically simplify the vertical structure. Our model consists of a thin, upper weather layer (layer 1), supported hydrostatically by a deep layer (layer 2). The density of each layer is assumed to be constant, with the upper-layer density ρ_1 taken to be less than the lower-layer density ρ_2. By specifying constant density layers, we decouple the thermodynamics from the system, while, it is hoped, retaining much of the important dynamics. The upper layer contains the vortices and all the time-dependent motions. The lower layer represents the neutrally stratified deep atmosphere. Since the lower layer is very deep, changes in the height of the layer interface that are due to upper-layer motions do not significantly change the thickness of the lower layer, and hence have a negligible effect on the deep motions. Any motions in the lower layer are assumed to be zonal and steady. This two-layer system may be reduced to a one-layer system with meridionally varying, solid-bottom topography (Gill, 1982).

The IC81 and M88 studies used the quasi-geostrophic (QG) equations, while the WY84 and WW88 studies used the SW equations. Dowling and Ingersoll (1988) observed that the upper-layer thickness and the Coriolis parameter vary substantially across the GRS, and estimated that the QG approximation is good only to about the nearest 30%. The next step, then, is to use a primitive equation model — the simplest example being the SW equations. Thus, we will model the GRS as a SW system, for which the momentum and continuity equations are:

$$\frac{\partial u}{\partial t} - (\zeta + f)v = -\frac{1}{r}\frac{\partial}{\partial \phi}\{g(h + h_2) + K\}, \tag{2.1}$$

$$\frac{\partial v}{\partial t} + (\zeta + f)u = -\frac{1}{R}\frac{\partial}{\partial \lambda}\{g(h + h_2) + K\}, \tag{2.2}$$

$$\frac{\partial h}{\partial t} + \nabla \cdot (h\mathbf{v}) = 0. \tag{2.3}$$

The dependent variables u, v, and h are the upper-layer eastward and northward horizontal velocities ($\mathbf{v} \equiv (u, v)$), and the thickness of the upper layer, respectively. The independent variables t, ϕ, and λ are the time, longitude (positive eastward), and planetographic latitude, respectively. We use oblate spherical geometry with radii of curvature r for the zonal direction and R for the meridional direction. If we define the equatorial and polar radii of the planet to be R_e and R_p and set $\epsilon \equiv R_e/R_p$, then

$$r(\lambda) = \frac{R_e}{\left(1 + \epsilon^{-2}\tan^2\lambda\right)^{1/2}}, \tag{2.4}$$

$$R(\lambda) = \frac{R_e}{\epsilon^2}\left(\frac{r}{R_e \cos\lambda}\right)^3. \tag{2.5}$$

For Jupiter $R_e = 71\,400$ km and $R_p = 66\,773$ km. Given a steady zonal profile for the deep layer $u_2(\lambda)$, the bottom topography $h_2(\lambda)$ is defined by

$$\frac{1}{R}\frac{\partial}{\partial \lambda} g h_2 = -\left(f + \frac{u_2}{r}\sin\lambda\right) u_2. \tag{2.6}$$

The term $u_2/r \sin\lambda$ in (2.6) is due to the spherical geometry, and is of order 100 times smaller than f. The parameter g is the reduced gravity:

$$g = g_J\left(\frac{\rho_2 - \rho_1}{\rho_2}\right), \tag{2.7}$$

where g_J is the actual gravity at Jupiter's cloud tops, which may be assumed constant in our shallow layer. The vertical component of absolute vorticity $(\zeta + f)$ is composed

of the relative vorticity $\zeta \equiv \hat{\mathrm{k}} \cdot (\nabla \times \mathrm{v})$, and the Coriolis parameter $f \equiv 2\Omega \sin\lambda$, where Ω is the planet's angular speed of rotation ($2\pi/\Omega = 9^h 55^m 29.7^s$). The kinetic energy per unit mass, $\frac{1}{2}(u^2 + v^2)$, is denoted by K.

For many of our numerical experiments we include a forcing/drag term on the right-hand side of (2.1):

$$-\frac{1}{\tau}\left(u - u_J(\lambda)\right), \tag{2.8}$$

where τ is typically 400 days, and $u_J(\lambda)$ is the observed, zonally-averaged, cloud-top velocity profile (Limaye, 1986). This forcing term, also used in WY84, represents a crude attempt at modeling the processes which maintain the observed profile. The value $\tau = 400$ days forces the eastward wind u on a time scale that is much longer than the time scales for dynamical processes such as gravity wave propagation, geostrophic adjustment, merging of vortices, and vortex circulation. Since we will find that forcing an unstable profile leads naturally to the genesis and maintenance of large, isolated vortices, understanding the possible physical processes modeled by this simplistic forcing term becomes an important goal for future work.

In a SW system, the horizontal velocities u and v are constant with height in each layer. It is not clear what amplitude of u and v to take for our upper layer which will best represent the real troposphere of Jupiter above and below the cloud tops. The appropriate u and v for the model layer are some type of vertical average over the velocities in the real atmosphere. Achterberg and Ingersoll (1989) study the connection between Jupiter's atmosphere and simple normal-mode models, and find that the appropriate velocity magnitudes for a single weather layer are within 10% of the real cloud-top magnitudes. This finding contrasts with an earlier suggestion by Allison and Gierasch (1982) that the appropriate velocity magnitudes in the model layer are a factor of 2.7 less than the real cloud-top values. By lowering the velocities in the model, the tendency towards instability is reduced. However, we will find that a

system in which the winds are strong and unstable naturally produces and maintains large, isolated vortices. Moreover, the observed cloud-top wind profile is in hand, and represents a definite layer of the atmosphere. We will therefore use the observed cloud-top winds to initialize our upper layer. An equally ambiguous problem is how to interpret the deep-layer velocity profiles u_2, which are produced by our analysis in Sec. 2.3. Our view is that gh_2 and the corresponding u_2 are important parameters of the SW system, and we are going to infer them from the *Voyager* data.

In our analysis the reduced gravity g appears only in combination with the variables h and h_2, such as the terms $g(h + h_2)$ or gh_2. We therefore do not have to know or specify the value of $(\rho_2 - \rho_1)/\rho_2$ in (2.7). We will refer to $g(h + h_2)$ as the free-surface height, and to gh_2 as the bottom topography. The connection between reduced gravity in the model and static stability on Jupiter is explored by Achterberg and Ingersoll (1989).

A dynamical variable of central importance is the potential vorticity q, defined by

$$q \equiv \frac{(\zeta + f)}{gh}. \tag{2.9}$$

The units of q are $\mathrm{s\,m^{-2}}$, with our definition differing from the usual one by the inclusion of the constant factor g. In the absence of dissipation, potential vorticity is a conserved quantity following the motion (Gill, 1982; Pedlosky, 1987):

$$\left(\frac{\partial}{\partial t} + \mathrm{v} \cdot \nabla\right) q = 0. \tag{2.10}$$

Dowling and Ingersoll (1988) used this fact to determine layer-thickness variations for the GRS and White Oval BC by following $(\zeta + f)$ along streamlines.

In a reference frame that drifts with the GRS, the motions are observed to be nearly steady. In the steady case, there is another conserved variable, the Bernoulli function, $B \equiv \{g(h + h_2) + K\}$. For $\partial/\partial t = 0$, (2.1) and (2.2) may be written

$$(\zeta + f)\,\hat{\mathrm{k}} \times \mathrm{v} = -\nabla B. \tag{2.11}$$

The conservation of B is readily shown by taking the dot product of (2.11) with v.

The Bernoulli function takes on special significance because it may be computed from the velocity field, via (2.11). We have calculated B for the GRS and Oval BC, with the results shown as the solid contours in Fig. 2.2. We use the same velocity data as in DI88, which is derived by tracking clouds in *Voyager* images. To begin, we determine u, v, and ζ on a longitude-latitude grid with spacings $\Delta\phi$, $\Delta\lambda = 0.5°$. These velocity and vorticity fields are calculated, as described in DI88, by least-squares fitting the velocity data inside a local averaging box, where here the averaging box is 3° on a side for both the GRS and Oval BC. We then use the following relaxation technique to compute B. Equation (2.11) is integrated to find B at the grid point (ϕ, λ) from B at each of the four neighboring points $(\phi + \Delta\phi, \lambda)$, $(\phi - \Delta\phi, \lambda)$, $(\phi, \lambda + \Delta\lambda)$, and $(\phi, \lambda - \Delta\lambda)$. These four values of B are averaged and the result is assigned to (ϕ, λ). To facilitate the calculation, the $(\zeta + f)u$ and $(\zeta + f)v$ fields are computed on grids staggered by half a spacing from the B grid. For gridpoints without four neighbors, we average over the contributions of the available neighbors. The procedure is iterated until it converges, and produces very satisfactory results. Since B is conserved following the motion, contours of B are streamlines, and those in Fig. 2.2 compare favorably with the streamlines calculated in DI88 by direct integration of the (u, v) data (compare Fig. 2.2 with Fig. 2.13). Also plotted as dashed contours in Fig. 2.2 is the free-surface height $g(h + h_2) = B - K$. Notice that the effect of subtracting K is not large.

Now that we have the B and $g(h + h_2)$ fields for the GRS and Oval BC, we may proceed to determine gh_2 for these vortices. The next section contains our method for inverting the velocity data to obtain gh_2, as well as the resulting deep winds and far-field potential vorticities, for the GRS and Oval BC.

FIGURE 2.2 : Bernoulli function B and free-surface height $g(h + h_2)$. (a) The solid and dashed contours show B and $g(h+h_2)$, respectively, for the GRS. These are in the vortex reference frame, with the zero of longitude corresponding to System III on 5 July 1979. The contour interval is $2 \times 10^4\, m^2/s^2$, with the innermost (highest) closed contour equal to $16 \times 10^4\, m^2/s^2$. (b) Same as (a) but for the Oval BC. The innermost closed contour is $14 \times 10^4\, m^2/s^2$.

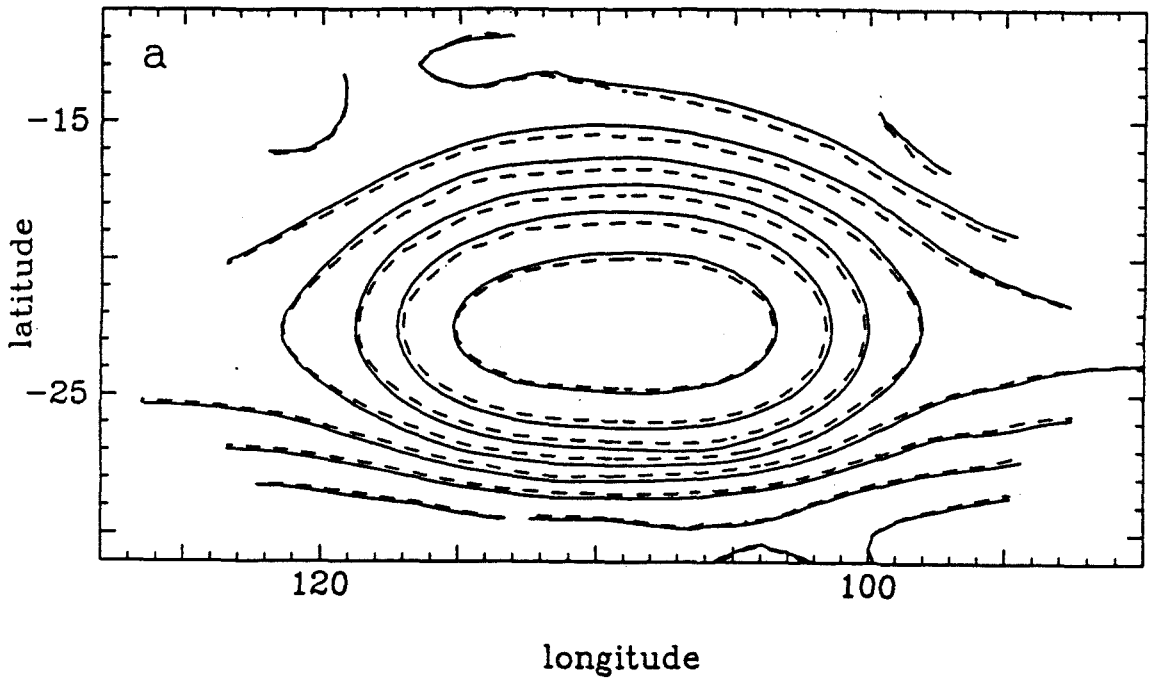
a
-15
-25
latitude
120
100
longitude

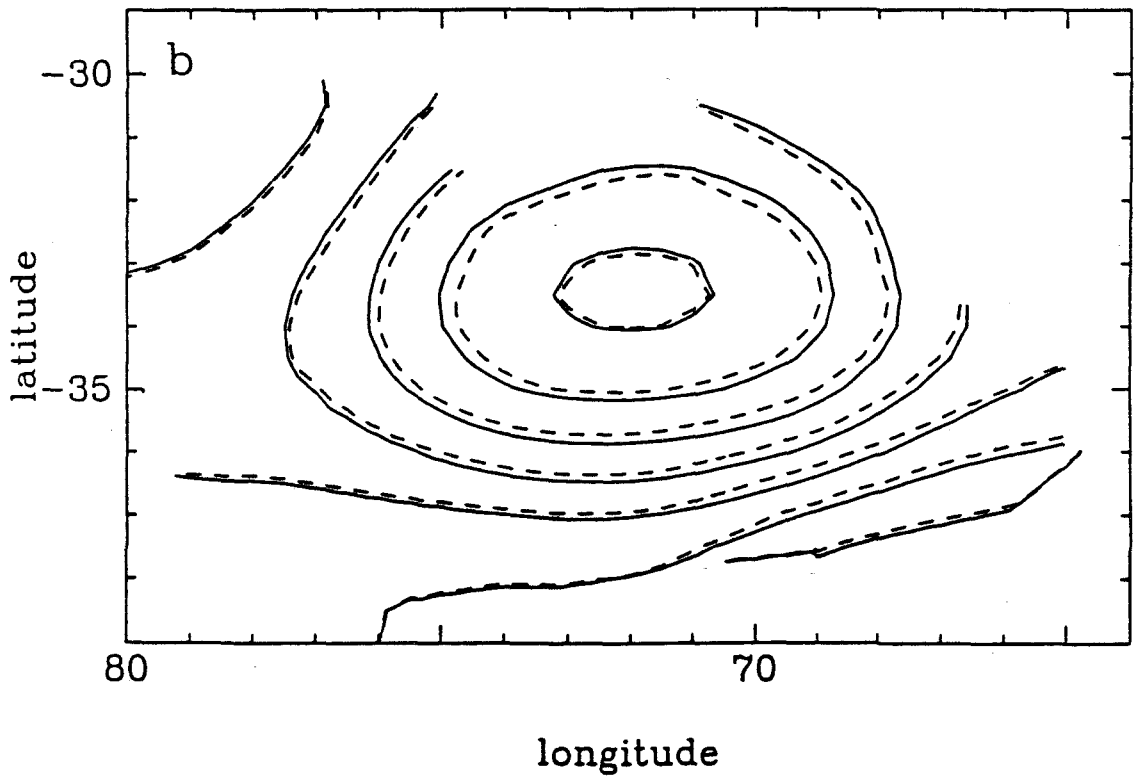
b
-30
-35
latitude
80
70
longitude

2.3 Calculation of Bottom Topography

Using (2.9) and the definition of B, the bottom topography gh_2 may be expressed as:

$$gh_2 = (B - K) - \frac{1}{q}(\zeta + f). \tag{2.12}$$

Since B, K, and $(\zeta + f)$ are observable, the only unknown on the right-hand side of (2.12) is q. On a streamline, both q and B are constant, so we may label streamlines with B and write $q = q(B)$, taking care to allow $q(B)$ to be multivalued when different streamlines have the same B value.

We model the function $1/q(B)$ as piecewise quadratic:

$$1/q(B) = 1/q_0 + (1/q_1)_j\, b + (1/q_2)_j\, b^2, \quad b \equiv (B/B_0 - 1), \tag{2.13}$$

where B_0 marks the largest closed streamline, and the subscript j refers to each region in which $q(B)$ is assumed to be quadratic. For the GRS (Fig 2.2a), $B_0 = 8.3 \times 10^4 m^2/s^2$. We label as N and S the northern and southern open streamline regions, defined by $B \leq B_0$ and λ greater or less than $-23°$, respectively. The critical open streamline that divides the N and S open streamline regions occurs at the latitude $\lambda_0 = -23°$ for the GRS and at $\lambda_0 = -34.5°$ for the Oval BC. These critical streamlines are important because they allow us to connect to the far field in a consistent manner. We find it convenient to divide the closed streamline region, $B > B_0$, into two regions labeled C for "central" and I for "inner." For the GRS the region C is defined by $15.6 \geq B > 8.3 \times 10^4\, m^2/s^2$, and the region I is defined by $B > 15.6 \times 10^4\, m^2/s^2$. This subdivision allows better handling of the crossover into the quiescent inner region of the GRS, where $(\zeta + f)$, and hence q, varies rapidly, but B varies slowly. For the Oval BC, $B_0 = 7.1\, m^2/s^2$; N and S are defined by $B \leq B_0$ and λ greater or less than $-34.5°$, respectively; C is defined by $13.1 \geq B > 7.1 \times 10^4\, m^2/s^2$, and I is defined by $B > 13.1 \times 10^4\, m^2/s^2$.

The form of (2.13) is such that $1/q(B_0) = 1/q_0$. We treat $1/q_0$ or q_0 for the GRS as our one free parameter, and invert the data to obtain the $(1/q_1)_j$ and $(1/q_2)_j$ in (2.13). Although we do not use the quasi-geostrophic approximation in this paper, we can relate q_0 to an effective radius of deformation for the system, L_d. If H denotes a characteristic depth of the upper layer, and f_0 a characteristic Coriolis parameter, then

$$L_d \equiv \frac{(gH)^{1/2}}{|f_0|}. \tag{2.14}$$

The Rossby numbers for the GRS and Oval BC are not greater than 0.36 (Mitchell, *et al.*, 1981), so that $\zeta < f_0$ and hence $q_0 \sim f_0/(gH)$. Thus,

$$L_d \sim \frac{1}{(f_0 q_0)^{1/2}}. \tag{2.15}$$

We will use (2.15) to relate the parameter q_0 to the more familiar parameter L_d.

The bottom topography under each vortex is modeled as a quartic in latitude, i.e.,

$$gh_2 = A_0 + A_1\lambda + A_2\lambda^2 + A_3\lambda^3 + A_4\lambda^4. \tag{2.16}$$

The data require at least a quadratic profile for the bottom topography, as shown in DI88. The quartic gh_2 model allows a cubiclike profile for $u_2(\lambda)$, which is appropriate if the deep winds consist of alternating east-west jets.

We now substitute (2.13) and (2.16) into (2.12) to get

$$B - K - \frac{1}{q_0}(\zeta + f) = A_0 + A_1\lambda + A_2\lambda^2 + A_3\lambda^3 + A_4\lambda^4 + \left\{(1/q_1)_j\, b + (1/q_2)_j\, b^2\right\}(\zeta + f), \tag{2.17}$$

where the left-hand side is the input data and the right- hand side is the model. The input data are arranged on the longitude-latitude grid used to calculate B in Sec. 2.2. Equation (2.17) is linear in the 13 unknown A and $1/q$ coefficients, and we solve it by the method of least squares. Once the value of q_0 is specified for the GRS, a

corresponding value for the Oval BC is fixed, as described below. In Table 2.1 we list results for the coefficients in (2.13) and (2.16), for three such paired values of q_0 for the GRS and Oval BC. Note that the A coefficients apply in the reference frame of each vortex. To change reference frames, replace u_2 defined in the vortex frame with u_2 defined in the System III frame, and use (2.6) to adjust gh_2 accordingly. The drift rates for the GRS and Oval BC relative to the System III reference frame were calculated in DI88 to be -0.258 ± 0.001 deg/day (westward drift) and 0.392 ± 0.007 deg/day (eastward drift), respectively.

Figure 2.3 shows q versus B for the case $q_0 = -1.40 \times 10^{-9}\, s\, m^{-2}$ for the GRS. This value of q_0 translates via (2.15) into an L_d of 2300 km (for $f_0 = -1.35 \times 10^{-4}\, s^{-1}$). The difference in the N and S curves for the GRS (Fig. 2.3a), as opposed to the lack of difference in those curves for the Oval BC (Fig. 2.3b), probably stems from the fact that B is noticeably steeper on the southern side of the GRS than the northern side. For other values of q_0, the solutions for $q(B)$ resemble those shown in Fig. 2.3, but shifted up or down the ordinate.

We tested the sensitivity of our results to the piecewise quadratic model for $q(B)$ by trying various alternatives, including piecewise linear through piecewise quartic functions, and by trying the regions C and I combined and separate. The resulting $q(B)$ depend very little on our model choice. For instance, combining regions C and I and assuming a quartic model for $q(B)$ in this combined region yields virtually the same profile as in Fig. 2.3, including the kink that marks the boundary between C and I. One measure of error is the spread in the results from all these approaches, which we will indicate when we compare GRS models.

Figure 2.4 shows the derived gh_2 and u_2 for the GRS and Oval BC. The dashed curve in Fig. 2.4a is the far-field, free-surface height $g(\bar{h} + h_2)$, calculated by integrating the cloud-top zonal-wind profile. The solid curves show gh_2 for various values

FIGURE 2.3 : Potential vorticity q versus Bernoulli function B. (a) Model results for the GRS. Different functions $q(B)$ are allowed for the northern and southern open streamline regions, denoted by N and S, respectively. The central closed streamline region is split into two pieces, denoted by C and I. The inner region I is defined by $B > 15.6 \times 10^4\, m^2/s^2$, the region C is defined by $15.6 \geq B > 8.3 \times 10^4\, m^2/s^2$, and the regions N and S are defined by $B \leq 8.3 \times 10^4\, m^2/s^2$, with latitude greater or less than $-23°$, respectively. Refer to Fig. 2.2a for a map of B. The function $1/q(B)$ is assumed to be piecewise quadratic in each region. The constant term $1/q_0$ is specified and equals $1/(-1.40 \times 10^{-9}\, s\, m^{-2})$ in this figure. (b) Same as (a) but for the Oval BC. The region I is defined by $B > 13.1 \times 10^4\, m^2/s^s$, the region C is defined by $13.1 \geq B > 7.1 \times 10^4\, m^2/s^2$, and the regions N and S are defined by $B \leq 7.1 \times 10^4\, m^2/s^2$, with latitude greater or less than $-34.5°$, respectively. The specified parameter $1/q_0$ equals $1/(-1.84 \times 10^{-9}\, s\, m^{-2})$.

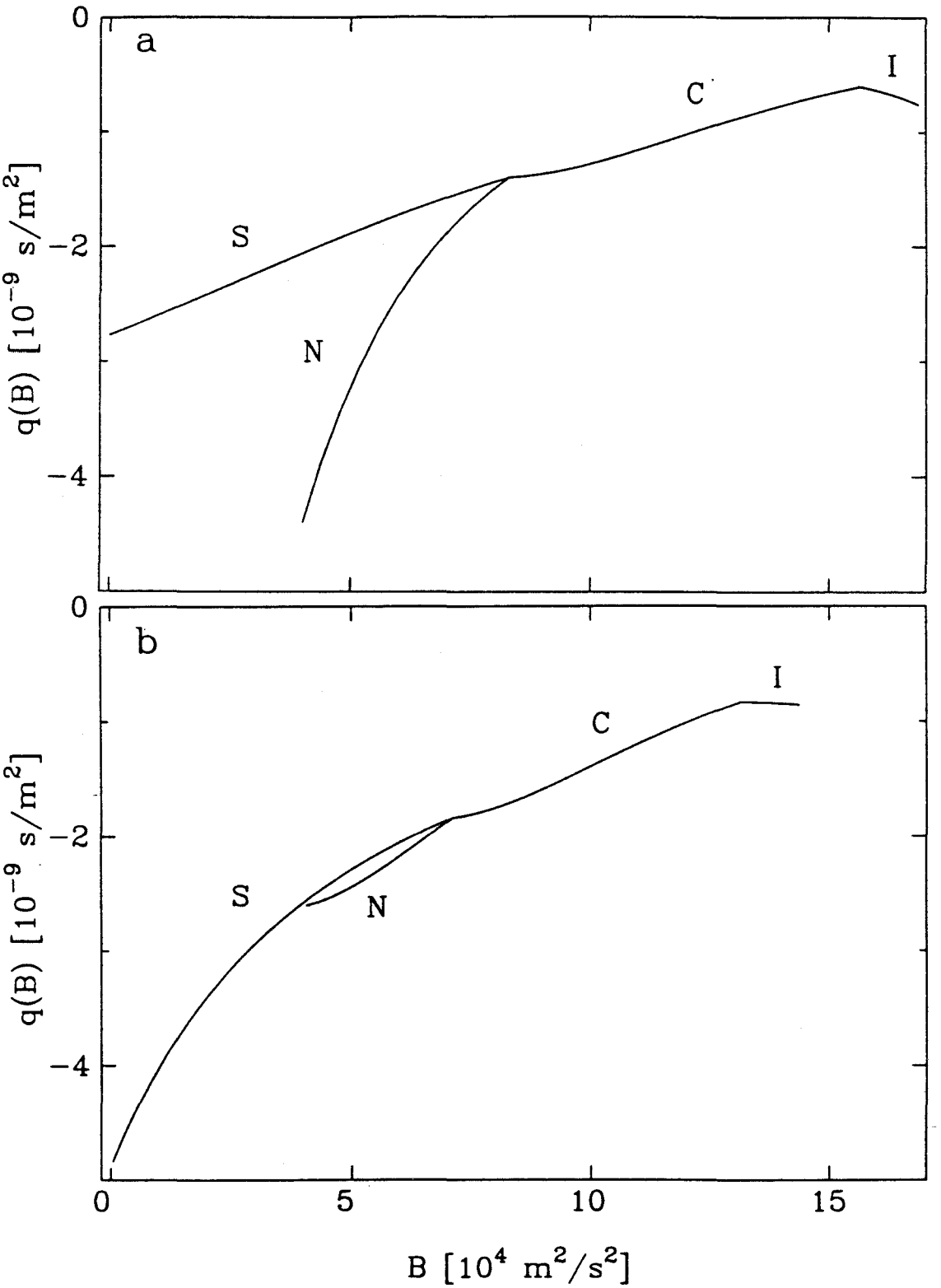
a
b
S
N
C
I
0
−2
−4
0
5
10
15
q(B) [10^−9 s/m^2]
B [10^4 m^2/s^2]

of q_0. To locate the position of the far-field, free-surface height $g(\bar{h} + h_2)$ above the derived bottom topography gh_2, we use the critical open streamline mentioned above, which runs from the far field to the largest closed streamline $B = B_0$. We require $\bar{q}$ at the far-field latitude λ_0 of the critical open streamline to be equal to $q(B_0) = q_0$. This requirement fixes $g\bar{h}$ to be equal to $(\bar{\zeta} + f)/q_0$ at $\lambda = \lambda_0$, thus locating the position of the far-field profile $g(\bar{h} + h_2)$ above gh_2. The error bars on the gh_2 curves in Fig. 2.4a indicate the variation of the data about each model fit, and are two standard deviations in total length. Our procedure for linking the bottom topographies determined from the GRS and Oval BC is as follows. First, we specify q_0 for the GRS, then determine gh_2 in the GRS reference frame, and shift it into the System III reference frame, using (2.6), thus yielding gh_2 over the latitudes $-31°$ to $-11°$. The Oval BC data apply over the latitudes $-39°$ to $-30°$. We vary q_0 for the Oval BC until it gives a gh_2 profile which, in the System III reference frame, matches the gh_2 from the GRS data at latitude $\lambda = -30.5°$. Thus, specifying q_0 for the GRS fixes q_0 for the Oval BC. The gh_2 profiles in Fig. 2.4a are labeled by q_0 for the GRS, in units of $10^{-9}\, s\, m^{-2}$. The connection at $\lambda = -30.5°$ is smoothed by fitting a parabola to the points in the interval $-30.5 \pm 2°$. In Fig 2.4b we show the u_2 profiles calculated from the gh_2 in Fig. 2.4a, using (2.6). (Here, for convenience, we neglect the $u_2/r \sin\lambda$ term in (2.6), which introduces less than 1% error in the u_2 determination.)

The deep layer results are intriguing. In the context of the SW equations, we are seeing the signature of differential motion in the deep atmosphere. We suspect that the shallow depth (small $g\bar{h}$) and relatively flat bottom (small $\partial gh_2/\partial\lambda$) of the upper layer in the latitudes northward of $-20°$ (Fig. 2.4a) are intimately related to the existence of the GRS's filamentary region. Convection, were it possible in a SW system, might correspond to negative upper-layer thickness $g\bar{h}$. Since convective plumes appear to form regularly in the GRS's filamentary region, perhaps the

FIGURE 2.4 : Bottom topography gh_2 and deep-layer velocity u_2. (a) The dashed curve shows the far-field, free-surface height $g(\bar{h} + h_2)$ calculated from the cloud-top, zonal-wind profile of Limaye (1986). The solid curves show different solutions for the bottom topography gh_2, inferred from the data. See the text for a description of the data inversion method. The error bars indicate the variation of the data about each model fit, and are two standard deviations in total length. The curves are labeled by the parameter q_0 in units of $10^{-9}\, s\, m^{-2}$. The bottom topographies under the GRS and Oval BC are assumed to be quartics in latitude, and are spliced together by fitting a parabola to the points in the interval $-30.5 \pm 2°$. The results are presented in the System III reference frame, with the zero of the ordinate defined to be the minimum of the curve $g(\bar{h} + h_2)$. (b) The dashed curve shows the cloud-top wind profile of Limaye. The solid curves show different solutions for the deep-layer velocity u_2, corresponding to the gh_2 presented in (a).

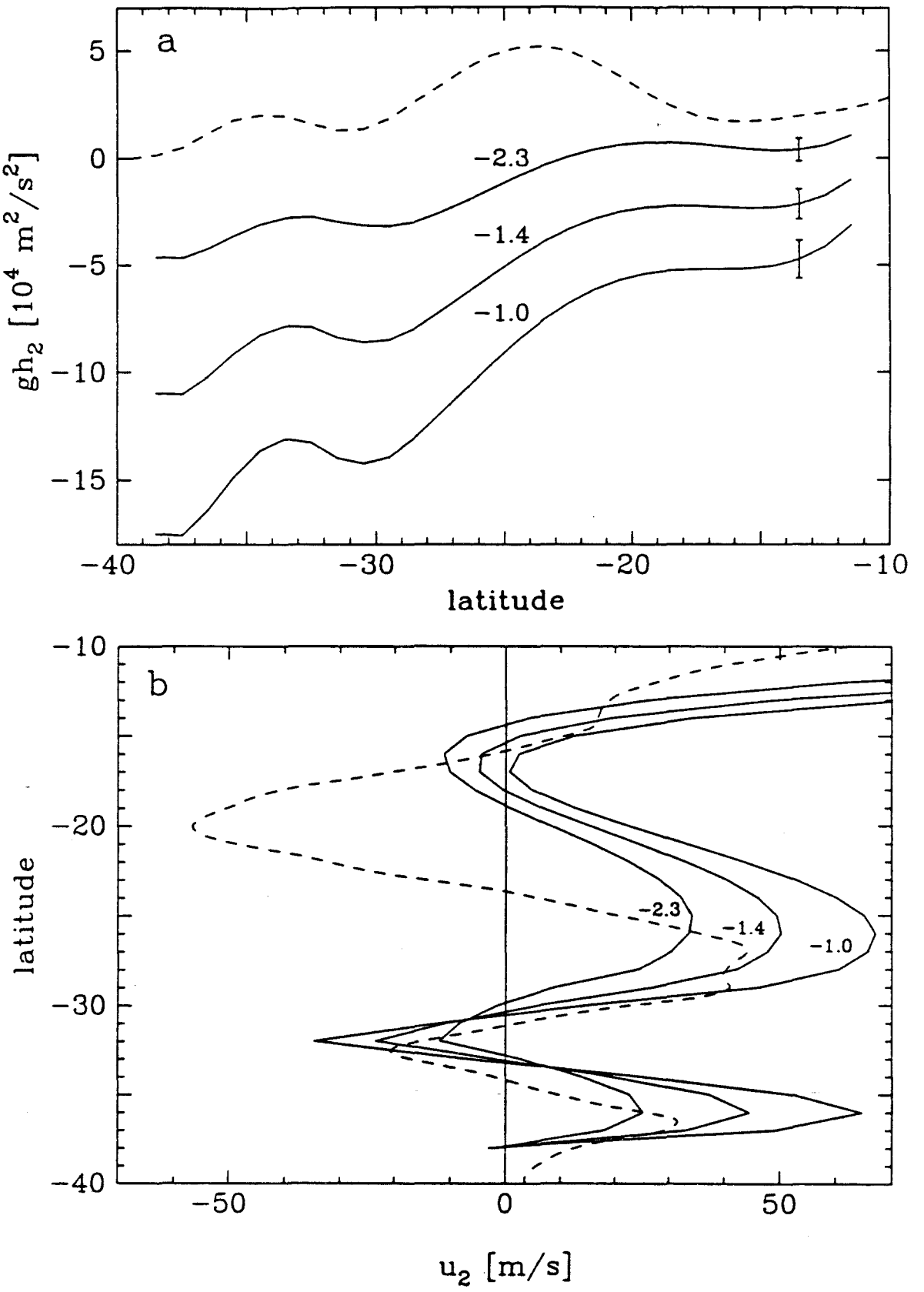
a
5
0
−5
−10
−15
−40
−30
−20
−10
latitude
gh_2 [10^4 m^2/s^2]
−2.3
−1.4
−1.0
b
−10
−20
−30
−40
−50
0
50
latitude
u_2 [m/s]
−2.3
−1.4
−1.0

TABLE 2.1

Table 2.1. Results for SW model coefficients in (2.13) and (2.16).

	GRS	BC	GRS	BC	GRS	BC
q_0	−2.30	−3.70	−1.40	−1.84	−1.00	−1.21
$(1/q_1)_N$	−1.146	−0.525	−1.264	−0.630	−1.384	−0.740
$(1/q_2)_N$	−0.589	−0.390	−0.626	−0.603	−0.664	−0.824
$(1/q_1)_S$	−0.465	−0.355	−0.536	−0.367	−0.608	−0.380
$(1/q_2)_S$	−0.084	−0.045	−0.182	−0.029	−0.282	−0.012
$(1/q_1)_C$	−0.197	−0.165	−0.096	−0.123	0.007	−0.079
$(1/q_2)_C$	−0.864	−0.544	−1.092	−0.755	−1.325	−0.974
$(1/q_1)_I$	−3.232	−1.119	−3.990	−1.564	−4.765	−2.025
$(1/q_2)_I$	2.552	0.562	3.307	0.934	4.078	1.320
A_0	65.30	5138.95	80.28	10352.75	95.60	15752.84
A_1	775.2	35527	968.3	71243	1166	108235
A_2	3460	91629	4240	182901	5036	277435
A_3	6599	104560	7956	207781	9342	314690
A_4	4477	44537	5302	88121	6146	133261

Note: λ in radians, $B_0(\text{GRS}) = 8.3 \times 10^4\, m^2/s^2$, $B_0(\text{BC}) = 7.1 \times 10^4\, m^2/s^2$; gh_2 in vortex reference frame, in units of $10^4\, m^2/s^2$; q in units of $10^{-9}\, s\, m^{-2}$.

appropriate q_0 is one that actually makes $g\bar{h}$ negative there. Negative $g\bar{h}$ occurs for $q_0 < -3.2 \times 10^{-9}\, s\, m^{-2}$, which by (2.14) corresponds to an effective $L_d < 1520$ km (for $f_0 = -1.35 \times 10^{-4}\, s^{-1}$). The biggest difference observed between the derived u_2 and the cloud-top winds (Fig. 2.4b) also occurs in the latitude band of the GRS's filamentary region. Our results imply that wind speeds in the cloud-top westward jet at $\lambda \sim -20°$ decay rapidly with depth. In contrast, the u_2 profiles under the Oval BC are fairly similar to the zonally-averaged cloud-top winds. Clearly, at this point we could use some additional data to pin down q_0, but such an absolute determination of the static stability of Jupiter's lower troposphere may prove difficult (cf., Flasar and Gierasch, 1986).

Once we have gh_2, we may determine the far-field potential vorticity of the system, using (2.9). The Limaye profile of zonal velocity is used to compute the far-field profiles $\bar{\zeta}$ and $g(\bar{h} + h_2)$, and hence the far-field $\bar{q}$ profiles. In Fig. 2.5, the dashed curve shows $\bar{q}$ versus latitude for the case $q_0 = -1.40 \times 10^{-9}\, s\, m^{-2}$ for the GRS. The error bar indicates the variation of the data about the model fit, and is two standard deviations in total length. Instability of the zonal flow is possible where $\bar{q}$ has a local extremum. For a recent analysis of the stability of zonal flows in a SW system, see Ripa (1983). We will examine the stability of this system numerically in Sec. 2.5. The GRS model of Marcus (1988) assumes constant far-field potential vorticity. The large violations of this assumption seen in Fig. 2.5 will show up clearly in the Lagrangian $(\zeta + f)$ analysis of an M88 vortex, discussed in Sec. 2.5. In Fig. 2.5 the solid curves are profiles of q versus latitude through the centers of the GRS and Oval BC. These are computed using the calculated functions $B(\phi, \lambda)$ and $q(B)$ shown in Figs. 2.2 and 2.3, respectively. It is interesting to note that the GRS and Oval BC appear as minimum $|q|$ anomalies, that q in the inner regions of these vortices is relatively flat, and that the drop-off of q to the far-field profile is fairly symmetric on the northern and

southern ends of the vortices. Rhines and Young (1982) discuss the homogenization of potential vorticity in the interior of closed-streamline regions. Marcus (1988), using the velocity profiles of Mitchell *et al.* (1981), reached a conclusion similar to ours, namely, that the potential vorticity in the inner regions of the GRS and Oval BC is approximately uniform.

We now turn to a comparison of the derived (DI89) gh_2 and far-field $\bar{q}$ with those prescribed by current models. For the DI89 case, we use $q_0 = -1.40 \times 10^{-9}\, s\, m^{-2}$ for the GRS, along with the corresponding $q_0 = -1.84 \times 10^{-9}\, s\, m^{-2}$ for the Oval BC. For the other models we take $q_0 = -1.40 \times 10^{-9}\, s\, m^{-2}$ at $\lambda = -23°$, which completely determines gh_2. The IC81 model prescribes u_2 to be equal to the zonally averaged cloud-top winds, which is the same as setting $g\bar{h} = \text{const.} = \{(\bar{\zeta}+f)/q_0\}|_{\lambda=-23°}$. The WY84 model prescribes solid-body rotation for the deep layer; i.e., $u_2 = \text{const.}$ In the System III reference frame the magnetic field of Jupiter, thought to be locked to the deep interior, is stationary by definition. Thus, for the WY84 model we assume that $u_2 = 0$, which implies $gh_2 = \text{const.} = \{g(\bar{h}+h_2) - (\bar{\zeta}+f)/q_0\}|_{\lambda=-23°}$. The M88 model prescribes constant far-field $\bar{q}$, which implies $g\bar{h} = (\bar{\zeta}+f)/q_0$.

In Fig. 2.6a, we plot gh_2 for the four models, DI88, IC81, WY84, and M88. The solid curve is the DI89 bottom topography, with the error bar on the right indicating the maximum variation of this profile over the entire region for the various models of the function $q(B)$ discussed at the beginning of this section. Notice that while some of the prescribed gh_2 agree with the derived gh_2 over certain ranges of latitude, none of them shows qualitative agreement over the entire latitude range observed. In Fig. 2.6b, we show the corresponding far-field potential vorticity profiles. Both the DI89 and WY84 potential vorticity profiles show significant local extrema, implying the possibility of instability for these models. We will run numerical models of the GRS in Sec. 2.5, using the various gh_2 shown in Fig. 2.6a. In Sec. 2.4 below we describe

FIGURE 2.5 : Potential vorticity q versus latitude. The dashed curve shows the far-field potential vorticity $\bar{q}$, calculated from the cloud-top zonal winds and inferred bottom topography (Fig. 2.4). The case presented has $q_0 = -1.40 \times 10^{-9}\, s\, m^{-2}$ for the GRS. The error bar indicates the variation of the data about the model fit, and is two standard deviations in total length. Instability of the flow is possible where $\bar{q}$ is a local extremum. The solid curves show profiles of q vs. λ through the centers of the GRS (right curve) and Oval BC (left curve). These are computed using the calculated functions $B(\phi, \lambda)$ and $q(B)$ shown in Figs. 2.2 and 2.3, respectively.

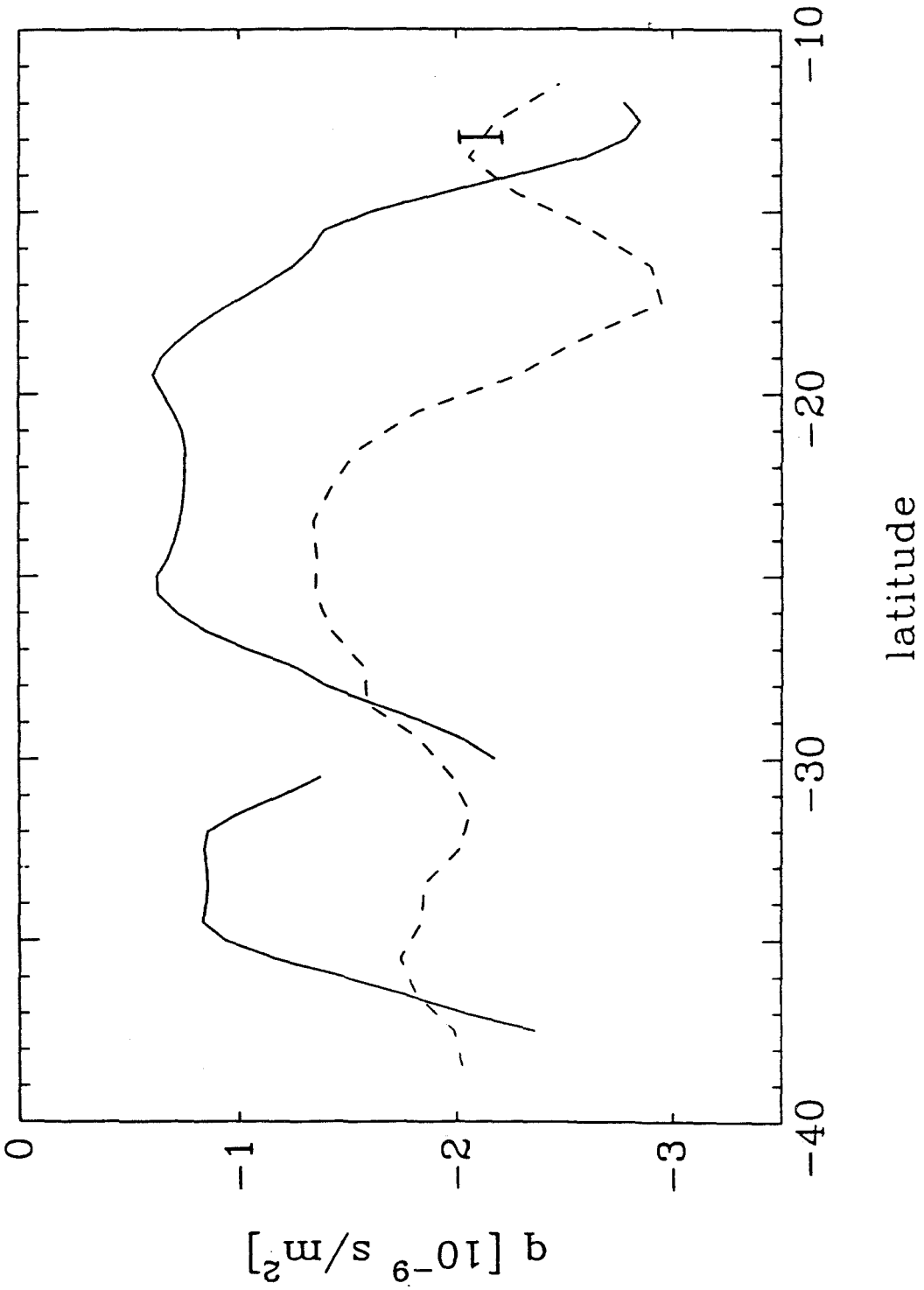
0
-1
-2
-3
-10
-20
-30
-40
latitude
q [10^-9 s/m^2]

our numerical scheme.

2.4 Numerical Scheme

We use the Arakawa and Lamb (1981) potential enstrophy and energy conserving scheme for the SW equations. This finite difference scheme is particularly suited to long-term integrations, especially when bottom topography is present. The Arakawa and Lamb scheme was also used by WW88. Because we want to incorporate observed cloud-top wind data, and to perform the same analysis on our simulations as done for the GRS and Oval BC in DI88, we use full oblate-spherical geometry.

The simulations are carried out on staggered longitude-latitude grids with 1° spacing. Relative to the grid on which vorticity is defined, u is computed on a grid shifted half a spacing northward, v is computed on a grid shifted half a spacing eastward, and gh is computed on a grid shifted half a spacing northward and half a spacing eastward. Since the GRS is about 20° by 10° in size, a 1° grid spacing is found to be quite adequate in resolving GRS-sized vortices. The domain is taken to be $-90°$ to 90° in longitude and $-40°$ to $-5°$ in latitude. The latitude range is sufficient to contain alternating jets to the north and south of the GRS shear zone, and to isolate the region of study from the boundaries. We use a time step of 15 minutes, which is small enough to prevent numerical instability, and provides adequate temporal resolution. Halving this time step has little effect on the simulations. Both WY84 and WW88 used similar domain sizes, and spatial and temporal resolutions.

We use periodic boundary conditions on the eastern and western boundaries. Because of the staggering of the variables, only v and q fall on the northern and southern boundaries, for which we specify $v = 0$, and $q = q_J$. The latter is a computational boundary condition with q_J equal to the potential vorticity calculated

FIGURE 2.6 : Bottom topographies gh_2 and far-field potential vorticity $\bar{q}$ for current models of Jovian vortices. (a) The dashed curve shows the far-field, free-surface height $g(\bar{h} + h_2)$ calculated from the cloud-top, zonal-wind profile of Limaye (1986). The solid curve, denoted by DI89, shows the bottom topography inferred from the data (this work) for the case $q_0 = -1.40 \times 10^{-9}\, s\, m^{-2}$ for the GRS, with the corresponding $q_0 = -1.84 \times 10^{-9}\, s\, m^{-2}$ for the Oval BC. The error bar on the right indicates the maximum variation of this bottom topography solution for various models of the function $q(B)$, as described in the text. The curves denoted by IC81, WY84, and M88 show bottom topographies prescibed by the Jovian vortex models of Ingersoll and Cuong (1981); Williams and Yamagata (1984); and Marcus (1988), respectively. (b) Corresponding far-field potential vorticities $\bar{q}$ for the models shown in (a).

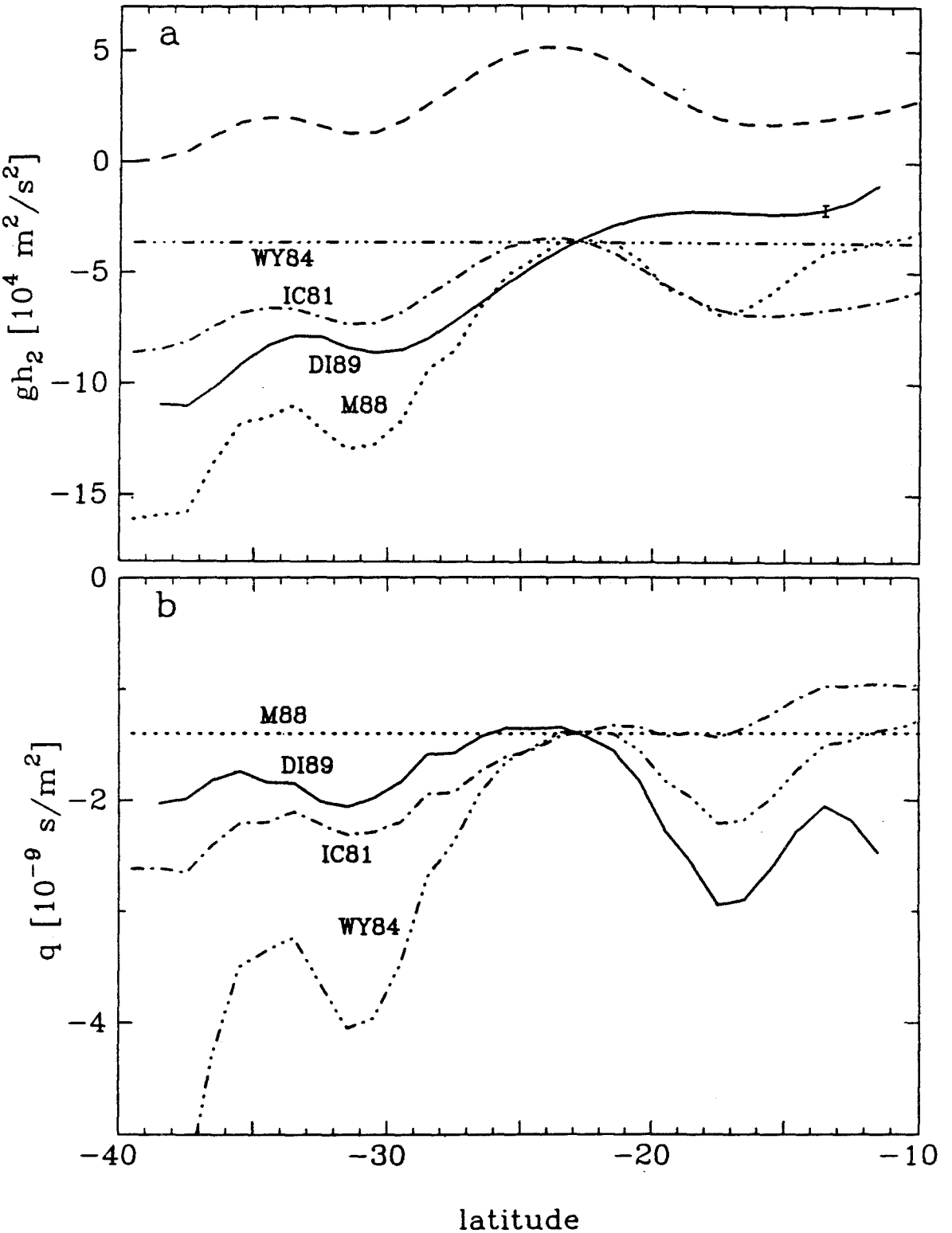
a
b
WY84
IC81
DI89
M88
gh_2 [10^4 m^2/s^2]
q [10^{-9} s/m^2]
5
0
−5
−10
−15
−2
−4
−40
−30
−20
−10
latitude

from the observed, zonally-averaged, cloud-top wind profile u_J and the particular bottom topography of the model.

The time integration is started with an Euler-backward (Matsuno) time step, followed by 11 leap-frog (centered-difference) steps. This sequence is then repeated. The Euler-backward step serves to prevent the odd-even separation of the leap-frog steps, and through its dissipative properties at small scales (Haltiner and Williams, 1980), represents the only source of viscosity in the system. With this scheme we did not find it necessary to use explicit dissipative terms or time smoothing to suppress small-scale noise and to prevent numerical instability. The small loss of total energy to the system from the dissipative Euler-backward time step corresponds to about the loss of the kinetic energy in a $100\,\mathrm{m\,s^{-1}}$ jet every 1000 years.

In many of our experiments, we force the u component of velocity by adding the forcing/drag term (2.8) to the right-hand side of (2.1), as described in Sec. 2.2. (Notice that we do not add a term like $-v/\tau$ to (2.2), which would inhibit meridional motions.) Since this term is parabolic, it should not be centered differenced (Haltiner and Williams, 1980), and we use forward differencing.

To initialize a run, we specify u, v, and gh at time $t = 0$, and the bottom topography gh_2. The bottom topography is specified by the given model, as discussed in Sec. 2.3. The free-surface height $g(h+h_2)$ is always initialized geostrophically from u_J, with the result shown as the dashed curve in Fig. 2.4a. If desired, a disturbance is then added to the $g(h + h_2)$ field, followed by geostrophic initialization of the u and v fields. The gh field is then computed by subtracting gh_2 from $g(h + h_2)$. A run of 250 simulated days (1 day $\equiv$ 24 hours) takes 4 CPU minutes on the San Diego Supercomputer Center's Cray X-MP/48, or 40 CPU hours on our μVax.

In the next section we use this numerical 1-1/2 layer SW scheme to examine the time evolution of the various models of the GRS described in Sec. 2.3. We then

perform the same Lagrangian vorticity analysis on the model vortices as was done for the GRS and White Oval BC in DI88. Next, we use the numerical scheme to examine the longevity and genesis of the present DI89 model of the GRS.

2.5 Numerical Experiments

2.5.1 Model Comparisons

We now examine the effect of changing the bottom topography on a vortex embedded in the observed cloud-top zonal winds of Jupiter. In Fig. 2.7 we show the initial free-surface height $g(h + h_2)$ for the model comparison experiments. This initial state is constructed by adding a bump of GRS-like dimensions to the free-surface height calculated from the observed, cloud-top wind profile, u_J, of Limaye (1986). Figure 2.6a shows the geometry prior to adding the initial vortex for each bottom topography to be considered. In the DI89 case, the numerical domain ($-40°$ to $-5°$ in latitude) is slightly larger than the data coverage ($-39°$ to $-11°$ in latitude). We extend the DI89 topography to the ends of the numerical domain by assuming constant gh in the end regions. The particular manner in which this extension is made is found to have little effect on the simulations. The initial vortex bump is given by:

$$a_1 \exp\left(-\left[\frac{(\phi-\phi_0)^2 + a_2(\lambda-\lambda_0)^2}{{a_3}^2}\right]^2\right), \tag{2.18}$$

where $a_1 = 4 \times 10^4\, m^2/s^2$, $a_2 = 3$, $a_3 = 9°$, $\phi_0 = 0°$, and $\lambda_0 = -21.5°$. We use a squared Gaussian instead of a Gaussian to imitate more closely the real GRS, which, because of its quiescent center, has a relatively flat top (Fig. 2.2a). The parameters in (2.18) were chosen so that the resulting radial velocity and vorticity profiles resemble those of the GRS (Mitchell *et al.*, 1981).

FIGURE 2.7 : Initial free-surface height $g(h + h_2)$ for the model comparison experiments. This initial state is constructed by adding a GRS-like vortex, described in the text, to the free-surface height calculated from the cloud-top zonal winds, and by geostrophically initializing the velocity field. The peak wind in the initial vortex is $91\,\mathrm{m\,s^{-1}}$ (System III). The contour interval for plots in this section is $1.5 \times 10^4\, m^2/s^2$, with the initial minimum $g(h + h_2)$ defined to be the zero contour, occurring at $\lambda = -40°$, and the innermost closed contour here equal to $9 \times 10^4\, m^2/s^2$. The right panel shows the zonally averaged, eastward wind $\bar{u}$ for this configuration.

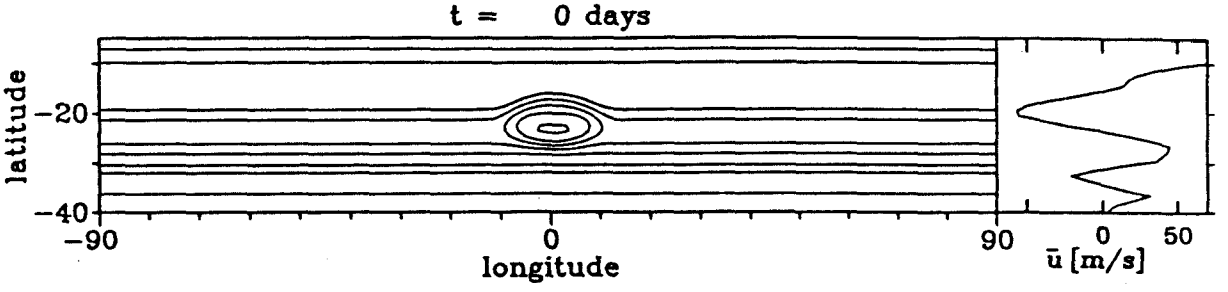
t = 0 days
latitude
−20
−40
−90
0
90
longitude
0
50
ū [m/s]

The first numerical run is for the DI89 bottom topography without the zonal forcing/drag term, i.e., using (2.1) without the additional term (2.8). Initially, the westward jet which flows around the northern side of the vortex creates a pattern suggestive of the filamentary region to the northwest of the GRS. This pattern can be seen in the $t = 20$ days time frame in Fig. 2.8. At this early time the zonal average of the eastward velocity $\bar{u}$, shown in the right panel, is still quite close to the initial profile. However, this is a transitory phase. By $t = 200$ days, $\bar{u}$ has smoothed out noticeably, and small eddies have begun to form in the $g(h+h_2)$ field. This instability of the shear flow is consistent with the existence of extrema in the far-field potential vorticity (Fig. 2.6b). The big vortex settles into a drift rate of about 0.33 deg/day, to be compared with the GRS drift rate of -0.258 ± 0.001 deg/day. The model vortex moves slowly enough so that the apparent drift from frame to frame is the actual drift. The peak wind in the vortex at $t = 1000$ days is $110\,\mathrm{m\,s^{-1}}$. Notice that it has grown in size by $t = 1000$ days, at the expense of the shear zone. The shape of the vortex at $t = 1000$ days is triangular, with a large penetration into the eastward jet on the southern side of the vortex. This triangular shape does not resemble the GRS, and suggests that the zonal winds on Jupiter are stiffened in some way. That the $\bar{u}$ profile smooths out with time also suggests that we should examine a case in which we force the zonal flow.

In Fig. 2.9 we show a DI89 run identical to that in Fig. 2.8 except that now we force the eastward velocity u towards u_J on a time scale $\tau = 400$ days by adding the term (2.8) to the right-hand side of (2.1). At $t = 20$ days the vortex is virtually identical to the previous case, again showing structure to the northwest, which is suggestive of the GRS's filamentary region. By $t = 200$ days, the effects of the zonal forcing/drag term become noticeable. The vortex throughout this run maintains an excellent GRS-like shape, and settles into a drift rate of about 0.22 deg/day. We will

compute absolute vorticity $(\zeta + f)$ profiles along streamlines (i.e., Lagrangian profiles) for this vortex, at $t = 1000$ days, and compare directly with the GRS observations of DI88. The $\bar{u}$ profile at $t = 1000$ days resembles the initial profile somewhat better than in the previous case (Fig. 2.8), but the strength of the westward jet at $\lambda = -20°$ is still reduced by about $10\,\mathrm{m\,s^{-1}}$, and there is no persistent structure analogous to a filamentary region. Getting a permanent filamentary region is probably going to require a model with higher horizontal and vertical spatial resolution, a more physically correct zonal forcing mechanism, and some simulation of convection, in addition to having the proper deep-atmospheric motions.

In Fig. 2.10 we show an IC81 run ($\tau = 400^d$). This run is the same as in Fig. 2.9 except for the change to the IC81 bottom topography. Differences between the DI89 and IC81 vortices can already be seen at $t = 20$ days. The IC81 vortices we have examined all drift westward at high speed, with this one moving at about -3.39 deg/day — over ten times faster than the GRS drift rate. The shear flow does not break up into small eddies, consistent with the lack of significant extrema in the far-field potential vorticity (Fig 2.6b). Without small eddies to feed on, this vortex slowly decays because of the zonal forcing/drag term. Ingersoll and Cuong have shown that the vortex will persist in the inviscid case ($\tau = \infty$). In a dissipative case, the vortex will persist if small eddies are occasionally added to the system, say by convection from the deep atmosphere. We will examine Lagrangian $(\zeta + f)$ profiles for the IC81 vortex at $t = 1000$ days.

In Fig. 2.11 we show a WY84 run ($\tau = 400^d$). This run is the same as in Fig. 2.9 except for the change to WY84 bottom topography. Again, differences can be seen between the WY84 vortex and the previous models as early as $t = 20$ days. Like the DI89 vortex, the WY84 vortex initially shows interesting structure in the flow around it. The shear flow is quite unstable and we found it necessary to run the model out to

FIGURE 2.8 : Free-surface height $g(h + h_2)$ for the DI89 run without zonal forcing ($\tau = \infty$). The initial height field is shown in Fig. 2.7, and the bottom topography gh_2 is shown in Fig. 2.6a. The vortex settles into a drift rate of about 0.33 deg/day in the System III reference frame, to be compared with the GRS drift rate of -0.258 ± 0.001 deg/day (Dowling and Ingersoll, 1988). The model vortex moves slowly enough so that the apparent drift from frame to frame is the actual drift. The peak wind in the vortex at $t = 1000$ days is $110\,\mathrm{m\,s^{-1}}$.

FIGURE 2.9 : DI89 run with zonal forcing ($\tau = 400^d$). Compare with Fig. 2.8. The vortex drift rate is about 0.22 deg/day, with a peak wind at $t = 1000$ days of $85\,\mathrm{m\,s^{-1}}$.

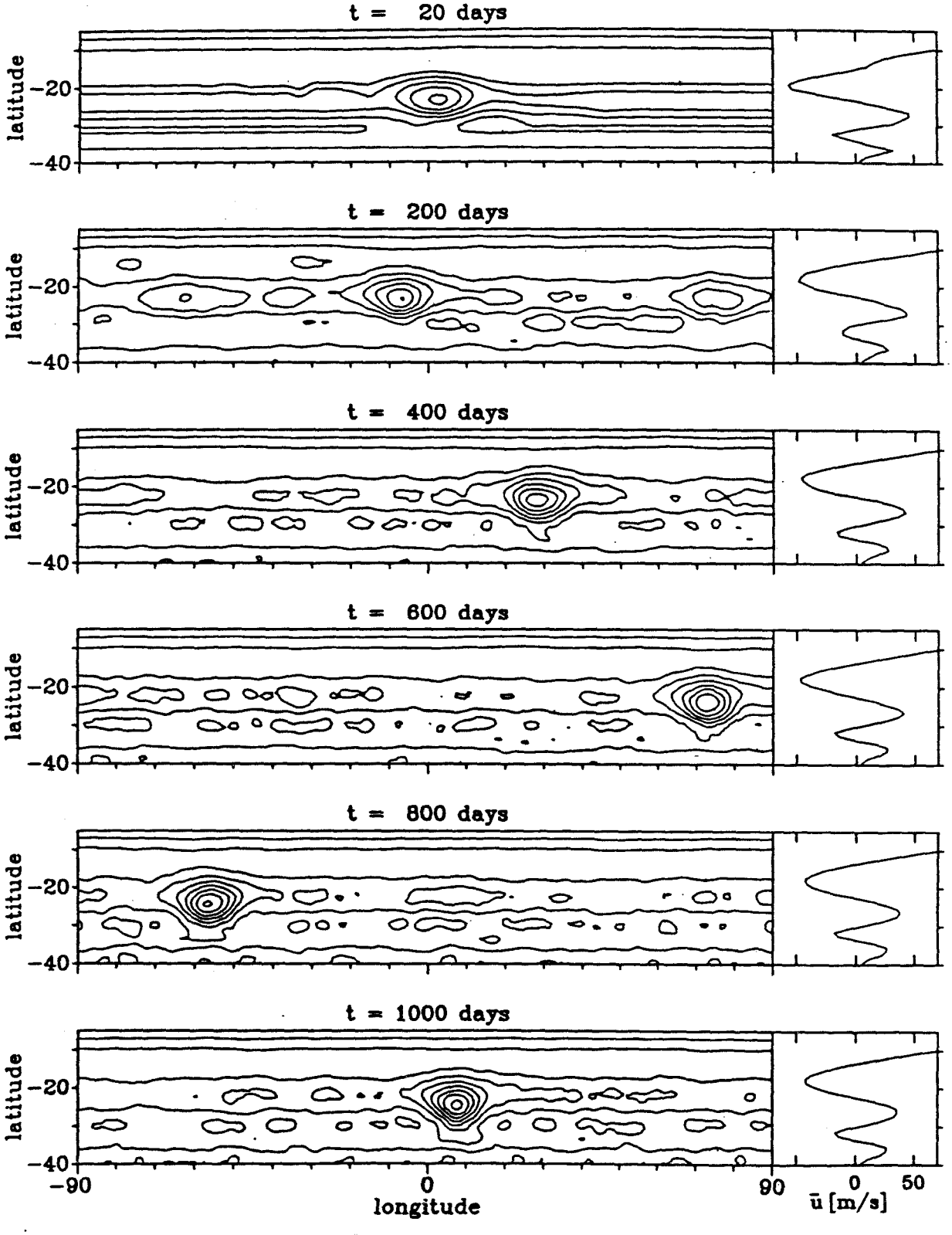
t = 20 days
t = 200 days
t = 400 days
t = 600 days
t = 800 days
t = 1000 days
latitude
-20
-40
-90
0
90
longitude
0
50
ū [m/s]

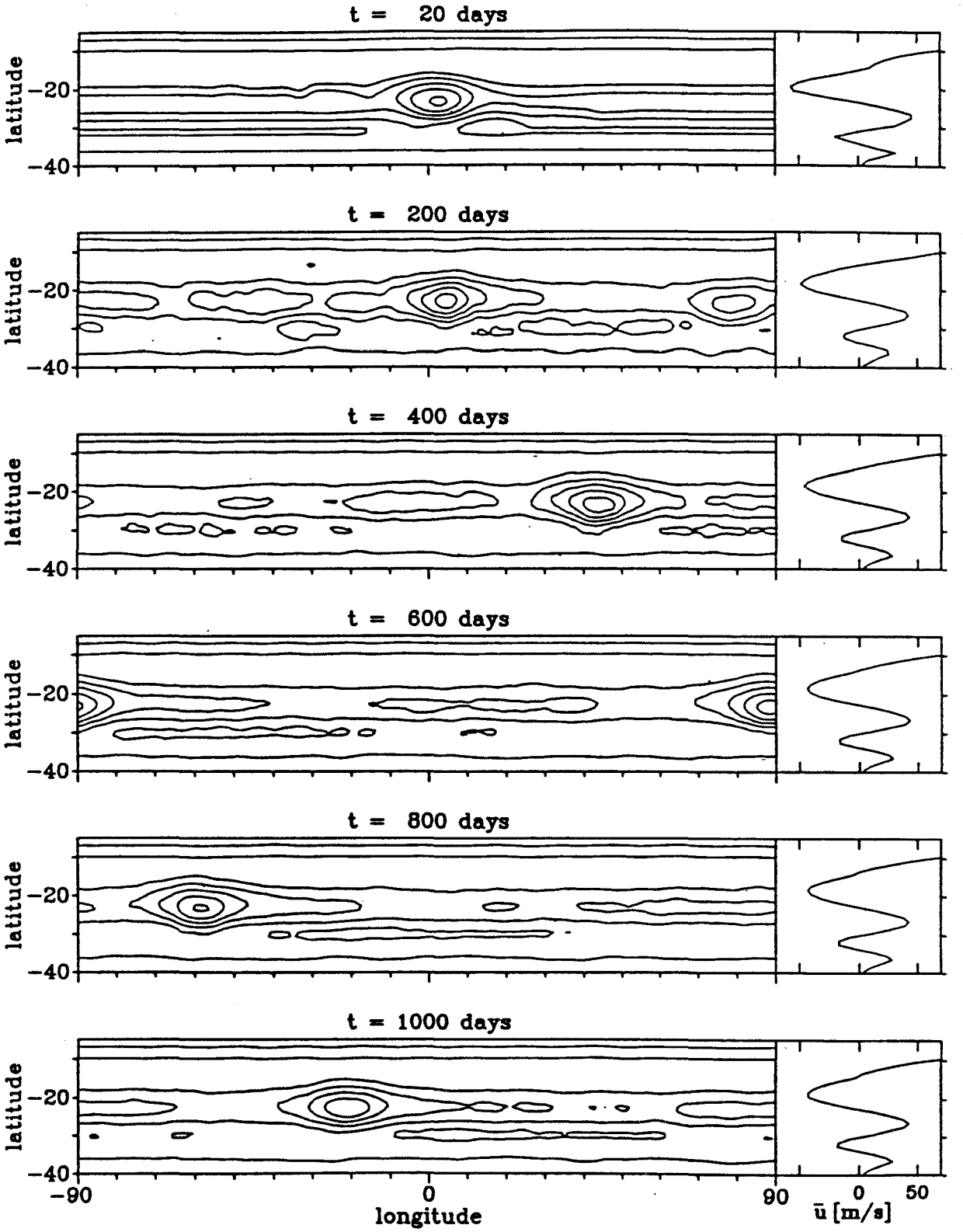
t = 20 days
t = 200 days
t = 400 days
t = 600 days
t = 800 days
t = 1000 days
latitude
-20
-40
-90
0
90
longitude
0
50
ū [m/s]

FIGURE 2.10 : IC81 run ($\tau = 400^d$). This run is the same as in Fig. 2.9 except for the change to the IC81 bottom topography shown in Fig. 2.6a. The vortex drifts at about -3.39 deg/day, and the peak wind at $t = 400$ and 1000 days is 65 and $56\,\mathrm{m\,s^{-1}}$, respectively. The vortex moves quickly enough so that the apparent drift from frame to frame is not the actual drift.

FIGURE 2.11 : WY84 run ($\tau = 400^d$). This run is the same as in Fig. 2.9 except for the change to the WY84 bottom topography shown in Fig. 2.6a. The vortex drifts at about -1.88 deg/day, and the peak wind at $t = 1600$ days is $105\,\mathrm{m\,s^{-1}}$. The vortex moves quickly enough so that the apparent drift from frame to frame is not the actual drift.

FIGURE 2.12 : M88 run ($\tau = 400^d$). This run is the same as in Fig. 2.9 except for the change to the M88 bottom topography shown in Fig. 2.6a. The vortex drifts at about -2.41 deg/day , and the peak wind at $t = 400$ and 1000 days is 91 and $72\,\mathrm{m\,s^{-1}}$, respectively. The vortex moves quickly enough so that the apparent drift from frame to frame is not the actual drift.

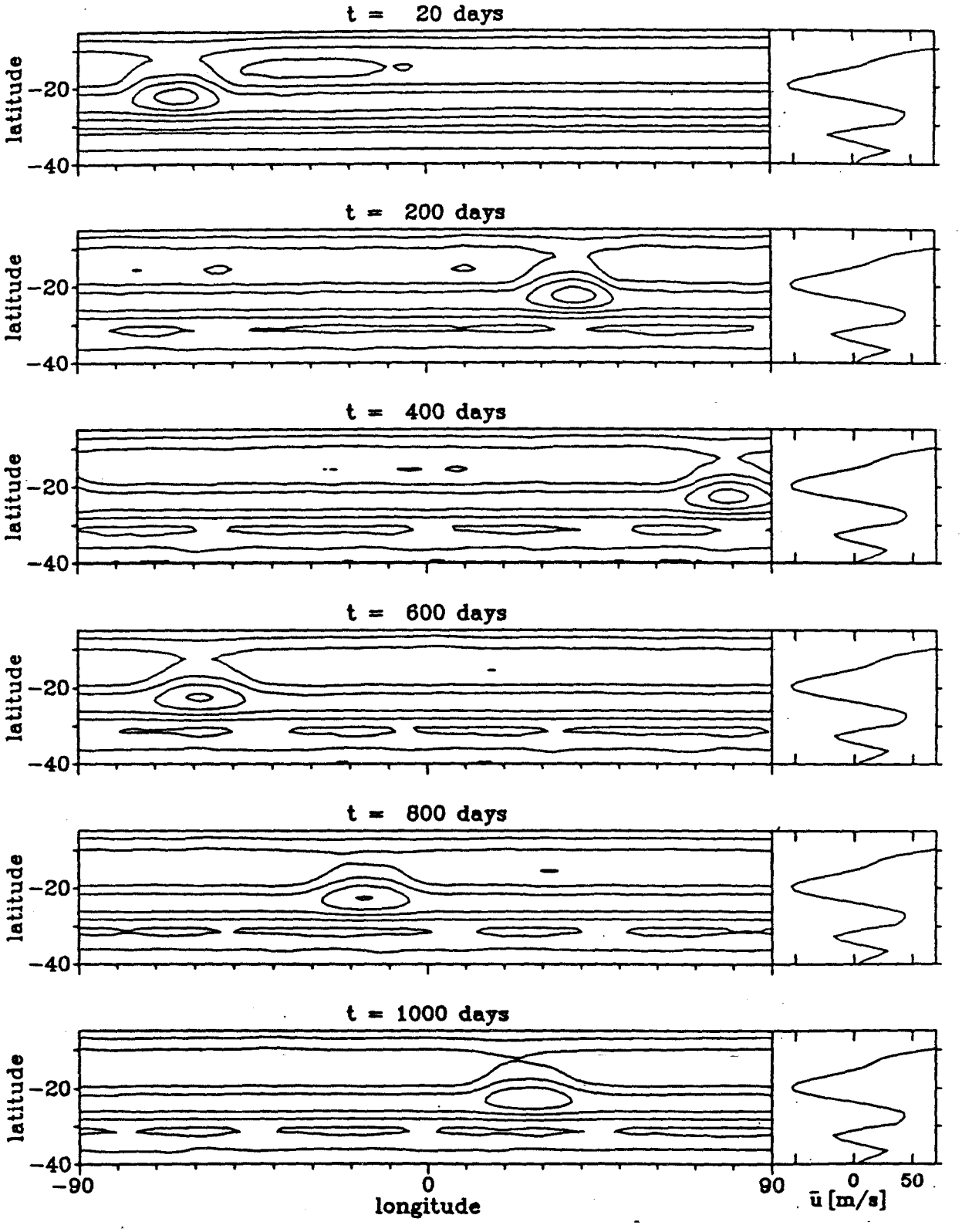
t = 20 days
t = 200 days
t = 400 days
t = 600 days
t = 800 days
t = 1000 days
latitude
-20
-40
-90
0
90
longitude
0
50
ū [m/s]

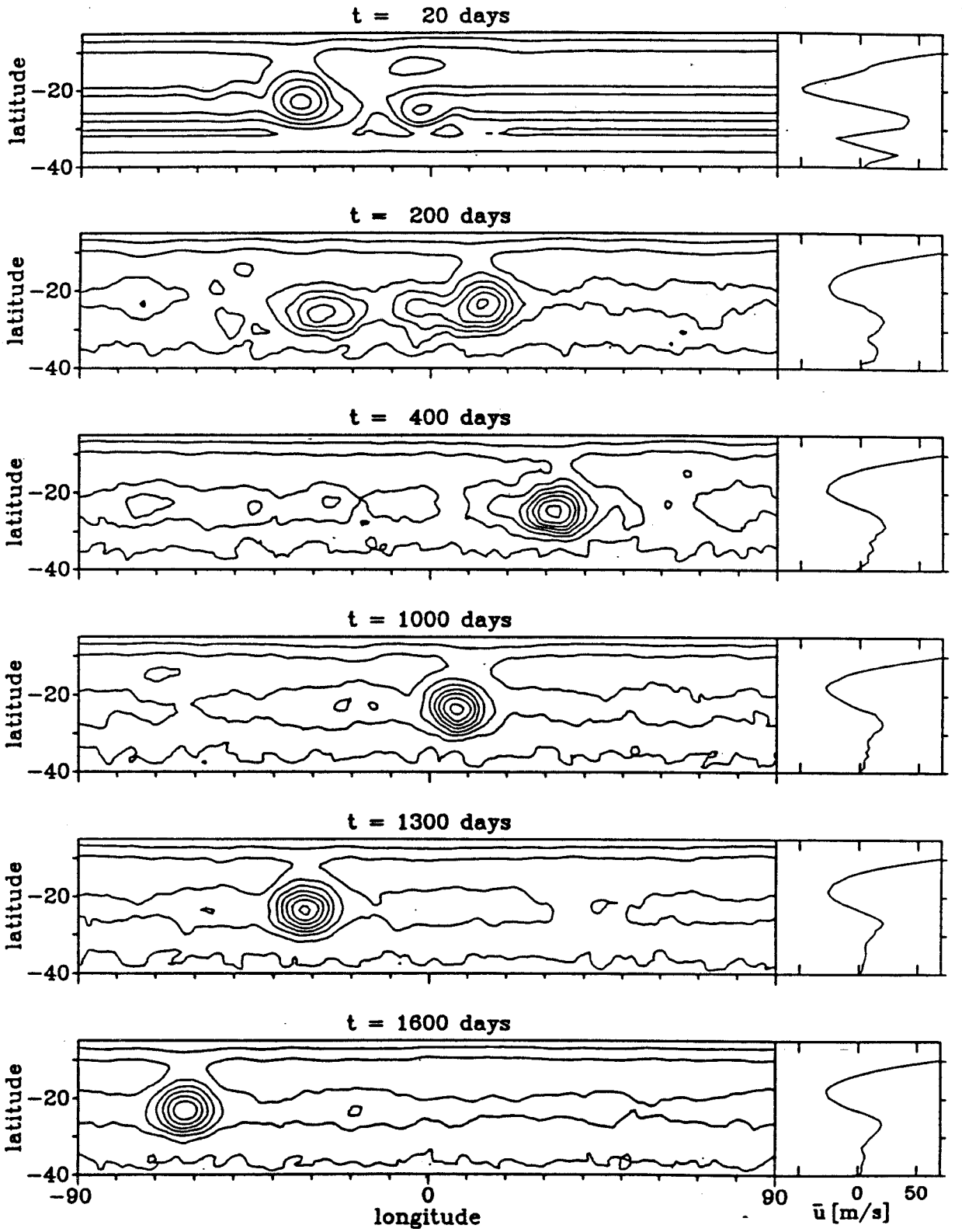
t = 20 days
t = 200 days
t = 400 days
t = 1000 days
t = 1300 days
t = 1600 days
latitude
-20
-40
-90
0
90
longitude
0
50
ū [m/s]

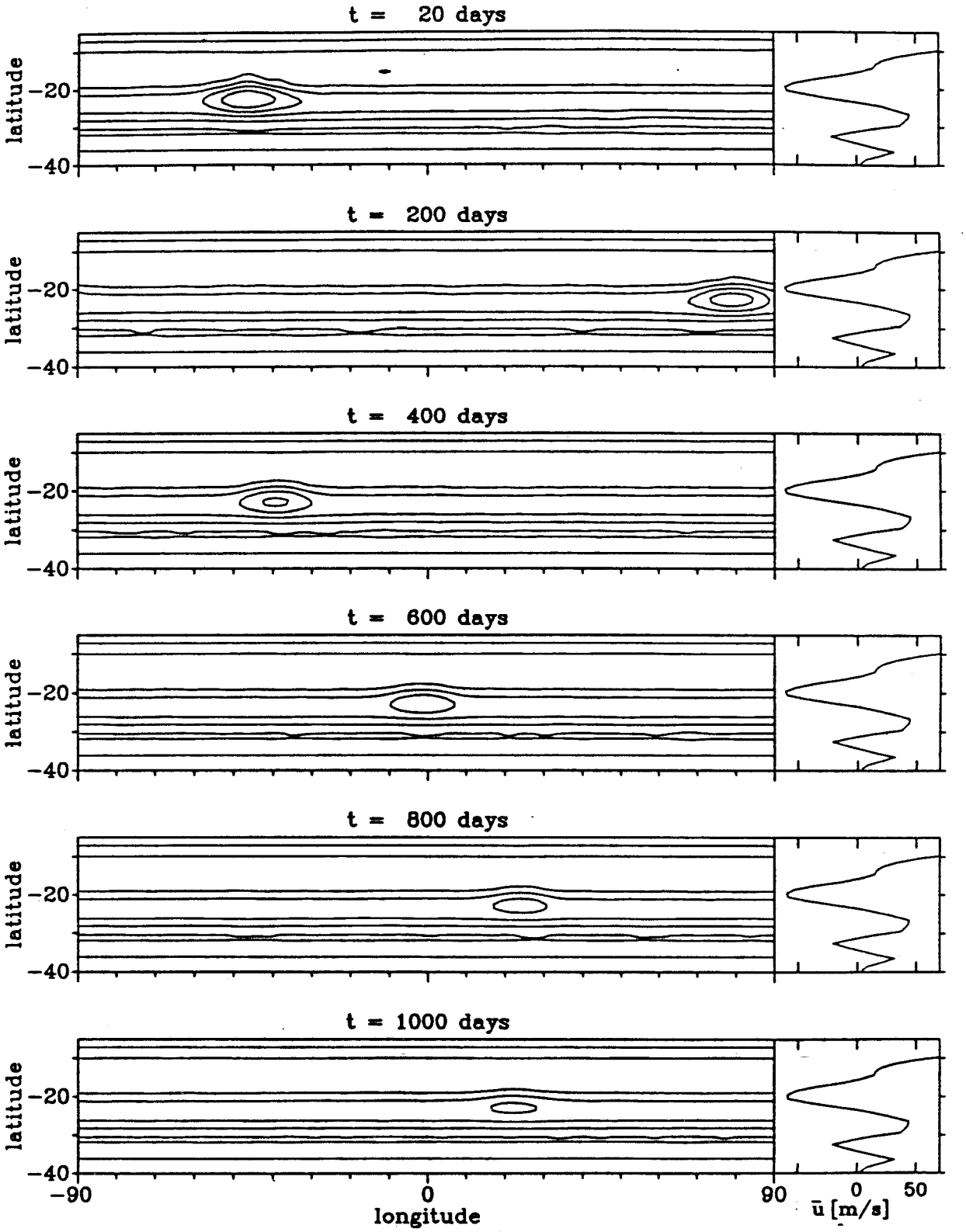
t = 20 days
t = 200 days
t = 400 days
t = 600 days
t = 800 days
t = 1000 days
latitude
-20
-40
-90
0
90
longitude
0
50
ū [m/s]

$t = 1600$ days before it settled into a quasi-steady state. The vortex drifts at about -1.88 deg/day in this experiment, but the drift rate tends to depend on the initial placement of the vortex and can be made closer to the GRS drift rate. The $\bar{u}$ profile at $t = 1600$ days is much weaker than the observed initial profile, and the vortex is correspondingly much stronger. Notice that the zonally-averaged velocity at the latitude of the White Oval ($\lambda = -33°$) is greatly reduced in magnitude, presumably related to the shallowness and instability of the upper layer in that region for this model. We will examine Lagrangian $(\zeta + f)$ profiles of the WY84 vortex at $t = 1600$ days.

In Fig. 2.12 we show a M88 run ($\tau = 400^d$). This run is the same as in Fig. 2.9 except for the change to M88 bottom topography. Since the far-field potential vorticity is uniform by design, the zonal velocity profile is stable. As in the IC81 case, without small eddies to feed on or some other driving force, the M88 vortex decays because of the zonal forcing/drag term. Both the IC81 and M88 models require something external to the present system to maintain their vortices against dissipation, while both the DI89 and WY84 models require zonal forcing to maintain their zonal velocity profiles against instability. We will examine Lagrangian $(\zeta + f)$ profiles for the M88 vortex at $t = 400$ days.

The Lagrangian vorticity results for the GRS from DI88 are reproduced in Fig. 2.13. The top panel shows the selected GRS streamlines used in the analysis, labeled a–h. The bottom panels show absolute vorticity $(\zeta + f)$ profiles, along streamlines, versus latitude λ. These profiles are proportional to the layer thickness gh, since q is constant along streamlines. For a geostrophic system, contours of $g(h + h_2)$ are coincident with streamlines, i.e., $g(h + h_2)$ is constant along streamlines. The GRS and Oval BC are close enough to geostrophic balance in this context for $g(h + h_2)$ to be approximately constant on a streamline, as can be seen in Fig. 2.2. Thus, the

$(\zeta + f)$ profiles are approximately proportional to the bottom topography itself, as determined in the reference frame of the vortex. We therefore expect the $(\zeta + f)$ profiles determined for the model vortices to mimic qualitatively the gh_2 profiles in Fig. 2.6a.

We apply the same algorithm developed for the GRS velocity data in DI88 to the model data. Streamlines are computed by first calculating a least-squares fit to the velocity data which fall inside a 3° by 3° averaging box, and then advecting the center of this averaging box accordingly. A typical profile of potential vorticity q, along a streamline, versus latitude is shown in Fig. 2.14. This profile comes from the largest closed streamline found for the DI89 vortex in Fig. 2.9, at $t = 1000$ days. The noise in q comes from calculation of the ζ term, which requires differentiating the velocity data. The dashed line in Fig. 2.14 shows the mean $\langle q \rangle = -1.60 \times 10^{-9}\, s\, m^{-2}$. The variation about the mean in terms of a standard deviation is $0.1 \times 10^{-9}\, s\, m^{-2}$, which is 2.6% of the total range of q for this time frame. If we were to use the wrong vortex drift rate in the analysis, off by say 0.5 deg/day, and thereby calculate an erroneous streamline, the resulting q profile would be noticeably nonconstant. Since the gh variable is quite smooth, a convenient and accurate way of removing the noise in the ζ variable is to use the relation $(\zeta + f) = q\, gh$, and replace q by the streamline mean $\langle q \rangle$. The $(\zeta + f)$ profiles computed for the model vortices will be presented in this manner.

The results of the Lagrangian vorticity analysis on the model vortices are shown in Fig. 2.15. In panel (a) we show the DI89 case. The solid curve is from the largest closed streamline, which is analogous to the GRS streamline d in Fig. 2.13. Notice that the contributions from the left and right halves of the vortex are virtually indistinguishable. The dotted curves are from streamlines analogous to the GRS streamlines f and h in Fig. 2.13. As discussed above, each of these $(\zeta + f)$ profiles

FIGURE 2.13 : Lagrangian vorticity analysis results for the GRS from Dowling and Ingersoll (1988). The top panel shows the selected GRS streamlines used in the analysis, labeled *a–h*. The dots indicate intervals of 10 hours. The bottom panels show absolute vorticity $(\zeta + f)$, along streamlines, versus latitude λ. The left and right panels correspond to the streamline segments left (west) and right (east) of 109° longitude, respectively. For each streamline there are three pairs of curves, and these curves are offset from the next by $75 \times 10^{-6} s^{-1}$ in the ordinate. The heavy dots are the computed $(\zeta + f)$. The dashed curves are f. The solid curves are a quadratic least-squares fit to the data. These $(\zeta + f)$ profiles are to be compared with those from the same analysis applied to the numerical vortices studied in this section.

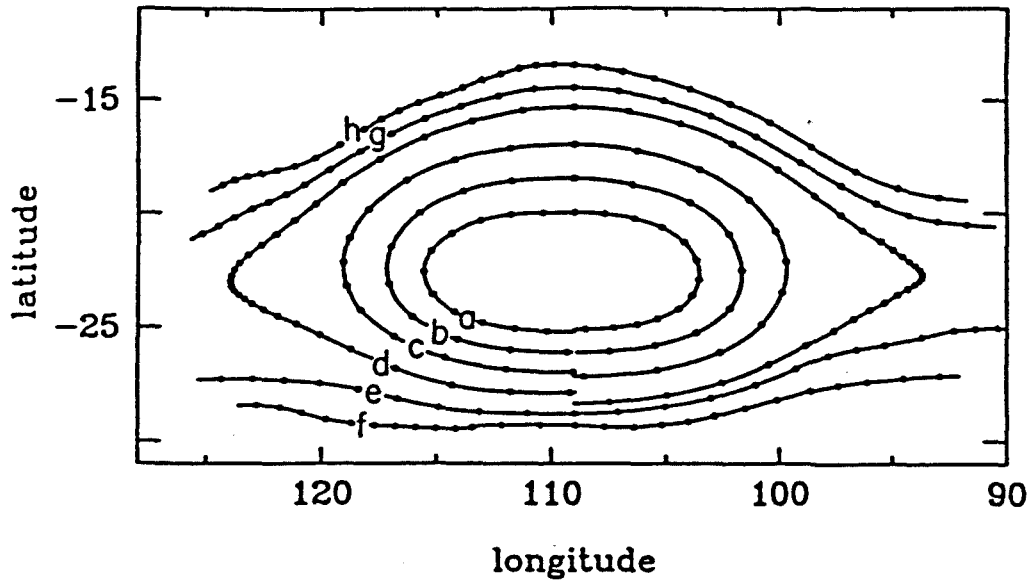
−15
−25
latitude
h
g
a
b
c
d
e
f
120
110
100
90
longitude

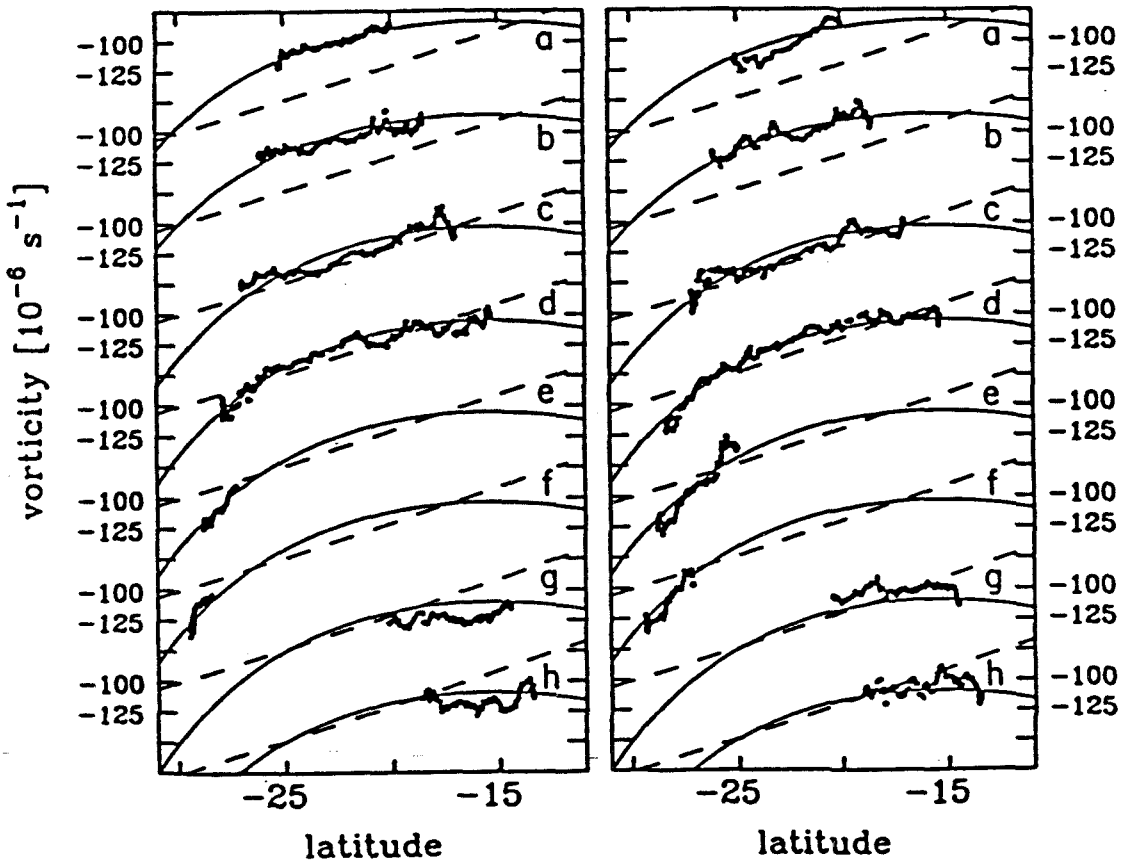
vorticity [10⁻⁶ s⁻¹]
−100
−125
a
b
c
d
e
f
g
h
−25
−15
latitude
−25
−15
latitude

FIGURE 2.14 : Typical profile of potential vorticity q along a streamline versus latitude λ. This profile comes from the largest closed streamline computed for the DI89 vortex in Fig. 2.9, at $t = 1000$ days. The dashed line shows the mean $\langle q \rangle = -1.60 \times 10^{-9}\, s\, m^{-2}$. The variation about the mean in terms of a standard deviation is $0.1 \times 10^{-9}\, s\, m^{-2}$, which is 2.6% of the total range of q for this time frame.

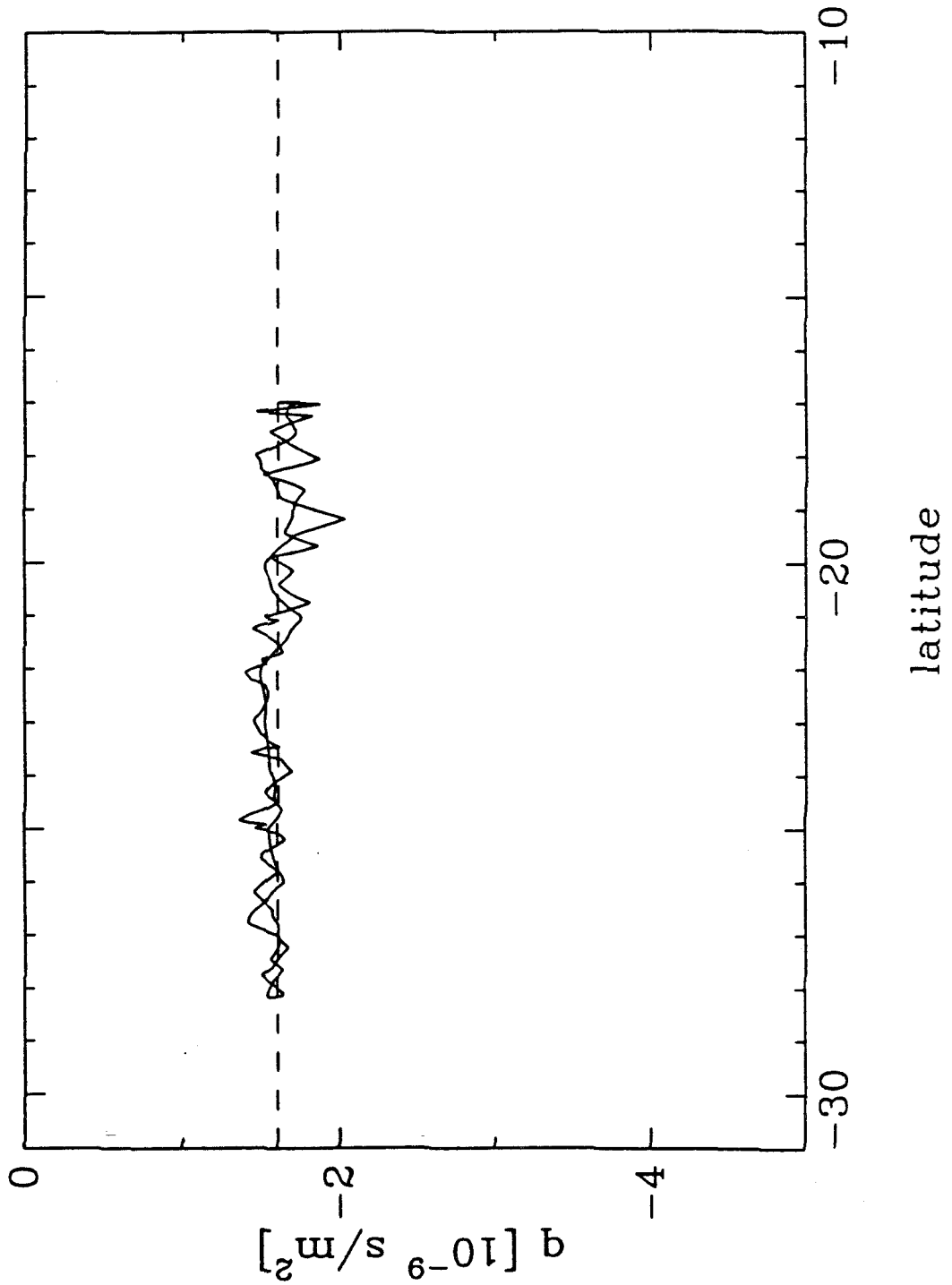
0
-2
-4
q [10^-9 s/m^2]
-10
-20
-30
latitude

mimics qualitatively the DI89 gh_2 profile (Fig 2.6a), with allowance made for the different q and $g(h + h_2)$ values among the different streamlines. The agreement between the DI89 model and the GRS is quite good. The IC81 case is shown in panel (b). In this particular run, the signature of the IC81 bottom topography is muted, but still discernible. The WY84 case is shown in panel (c). The $(\zeta + f)$ profile of a WY84 vortex always comes out straight, with the slope proportional to the velocity of the solid-body deep layer in the vortex reference frame. The M88 case is shown in panel (d). The characteristic dip seen in the M88 gh_2 profile between latitudes $\lambda = -20°$ and $-15°$ always shows up in M88 $(\zeta + f)$ profiles. In contrast, the $(\zeta + f)$ profiles for the GRS or the DI89 model do not show a dip in this region. We conclude from many comparisons of $(\zeta + f)$ profiles that only the present DI89 model is in agreement with the observations for the GRS, which is not surprising since the DI89 model is derived from the data. The significance of the agreement is that Lagrangian $(\zeta + f)$ profiles are a meaningful test of models, and other models of the GRS not examined here must pass the same test.

In the next subsection we briefly review proposed mechanisms for the maintenance against dissipation of Jovian vorticies, and examine the longevity and genesis of a DI89 model vortex.

2.5.2 Longevity and Genesis

The fact that storm systems on Jupiter (and Saturn) last for decades and centuries is fascinating to the earthbound observer, who is used to storm systems that last only weeks or months. The long-lived nature of Jovian vortices has been treated in the past as a special property which, once obtained in a model vortex, tended to be used to justify the assumptions of that model as applied to Jupiter. In particular, the nature of the deep atmospheric motions, or equivalently, the nature of the far-

FIGURE 2.15 : Absolute vorticity $(\zeta + f)$ along streamlines, versus latitude, for the different numerical models. (a) The DI89 run (Fig. 2.9) for $t = 1000$ days. The solid curve is from the largest closed streamline, which is analogous to the GRS streamline d in Fig. 2.13. The dotted curves are from streamlines analogous to the GRS streamlines f and h in Fig. 2.13. (b) The IC81 run (Fig. 2.10) for $t = 1000$ days. (c) The WY84 run (Fig. 2.11) for $t = 1600$ days. (d) The M88 run (Fig. 2.12) for $t = 400$ days.

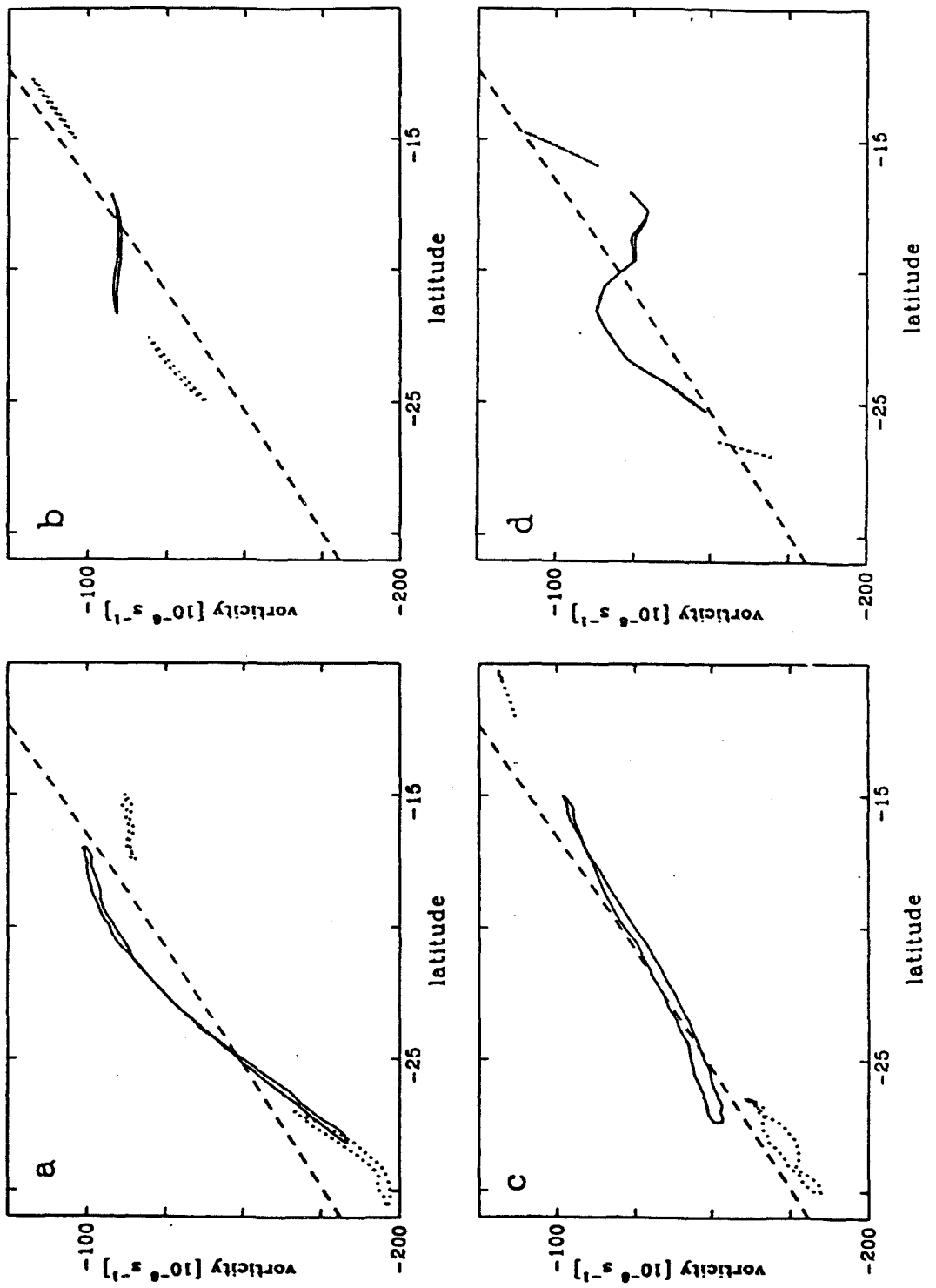
a
b
c
d
vorticity [10⁻⁶ s⁻¹]
latitude
-100
-200
-15
-25

field potential vorticity, was thought to play a special role in isolating cloud-top vortices. However, there are now several very different models of the deep motions in Jupiter's atmosphere, each of which is successful in maintaining large, isolated, long-lived vortices. The manner in which these isolated vortices maintain themselves against destructive processes such as dispersion and Rossby wave propagation seems not to depend on the details of the far-field potential vorticity.

In the case of a real atmosphere, vortices must also be maintained against dissipative forces. There are two major mechanisms currently proposed for maintaining Jovian vortices against dissipation. The baroclinic eddy models of Read and Hide (1983, 1984) rely on weak, steady effects such as nonlinear interactions and diabatic forcing (see Read, 1985, 1986) to balance dissipation. Alternatively, Ingersoll and Cuong (1981) have proposed that large vortices are maintained against dissipation by absorbing smaller vortices, which they suggested are produced by convection.

We propose that the dual problems of genesis of a GRS-like vortex and maintenance of that vortex against dissipation can be solved by finding a mechanism that maintains the cloud-top and deep zonal motions observed in Jupiter's atmosphere. Williams and Wilson (1988) arrived at a similar conclusion for the case of solid-body deep motions, so in general we expect that the necessary component is an unstable upper-layer zonal velocity profile. Given such a mechanism, we demonstrate below that the genesis and maintenance of a GRS-like vortex follows naturally from the derived (DI89) deep-layer zonal velocity profile.

In Fig. 2.16 we show the DI89 run of Fig. 2.9 extended through ten years. The system is in equilibrium, with the zonal forcing/drag term (2.8) maintaining the zonal jets in an unstable state. The jets produce small eddies that are absorbed by the large vortex. This process is inherently time-dependent, and in many ways resembles the complicated, time-dependent interactions observed in Jupiter's atmosphere.

FIGURE 2.16 : Longevity experiment. This is the DI89 run of Fig. 2.9 ($\tau = 400^d$) extended through ten years. The forcing of the unstable velocity profile continuously produces small vortices that are absorbed by the large vortex, thus maintaining it.

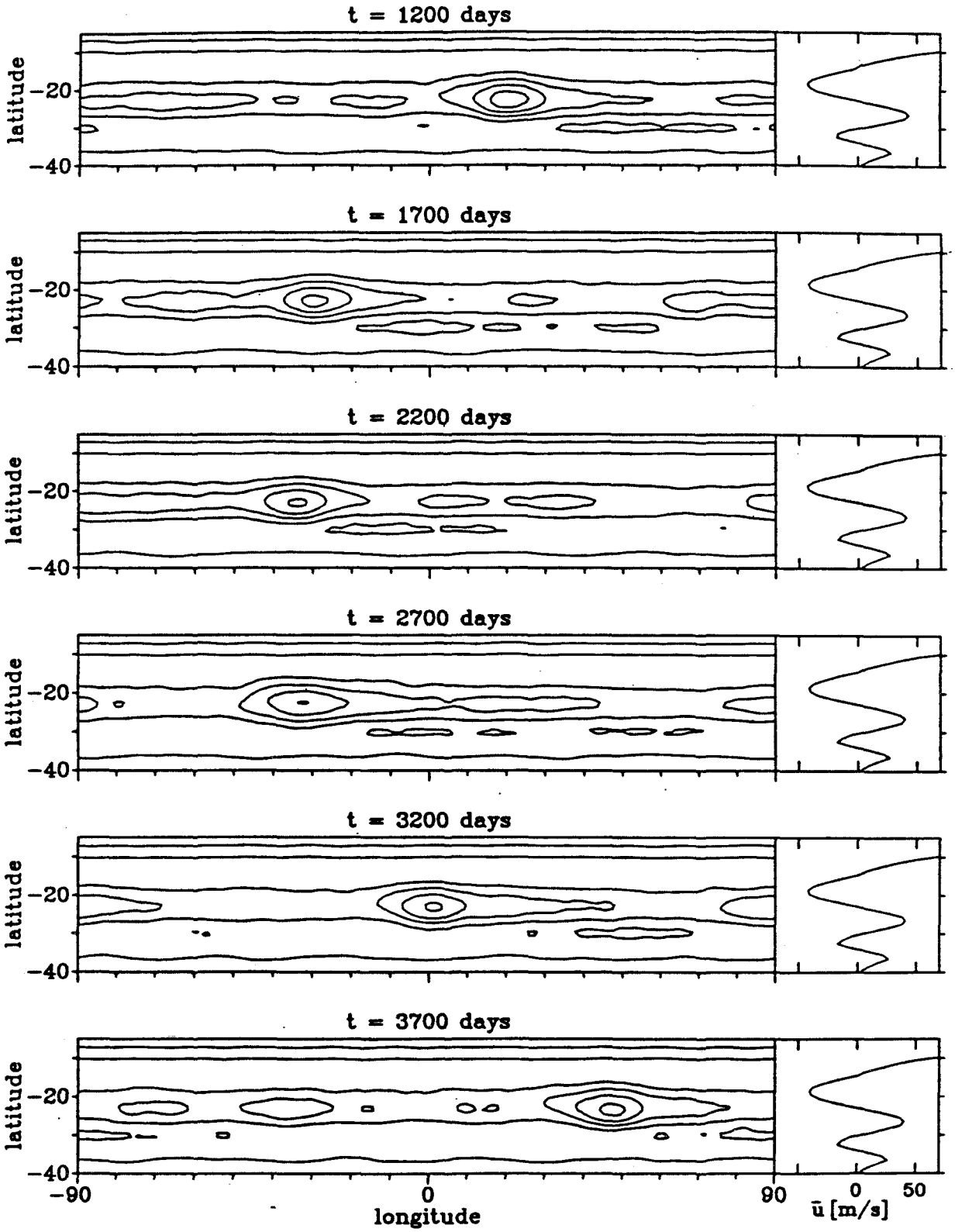
t = 1200 days
t = 1700 days
t = 2200 days
t = 2700 days
t = 3200 days
t = 3700 days
latitude
-20
-40
-90
0
90
longitude
0
50
ū [m/s]

FIGURE 2.17 : Genesis experiment. The initial state is constructed by adding a small sinusoidal perturbation of ten wavelengths, in a $\mathrm{sech}^2(\phi/90°)\sin^{1/2}(-\pi(\lambda + 5°)/35°)$ envelope, to the free-surface height $g(h + h_2)$ calculated from the cloud-top zonal-wind profile (Fig. 2.4). This envelope brings the perturbation of the northward velocity v to zero at the northern and southern boundaries ($\lambda = -5°, -40°$), and adds a slight longitudinal height difference to the initial ten waves. The specified parameter q_0 is $-1.40 \times 10^{-9}\, s\, m^{-2}$ for the GRS. The zonal wind is forced with $\tau = 400^d$. The peak initial perturbation velocity is $1.6\,\mathrm{m\,s^{-1}}$, compared to the $54\,\mathrm{m\,s^{-1}}$ peak initial zonal wind. By $t = 500$ days, there are three large, distinct vortices in the GRS's shear flow. By $t = 750$ days, two of these vortices have merged, and by $t = 1600$ days, only one large vortex remains. This vortex is run through $t = 2000$ days. Even though the initial conditions are vastly different for the run shown here and the run shown in Fig. 2.16, the final forms are quite similar.

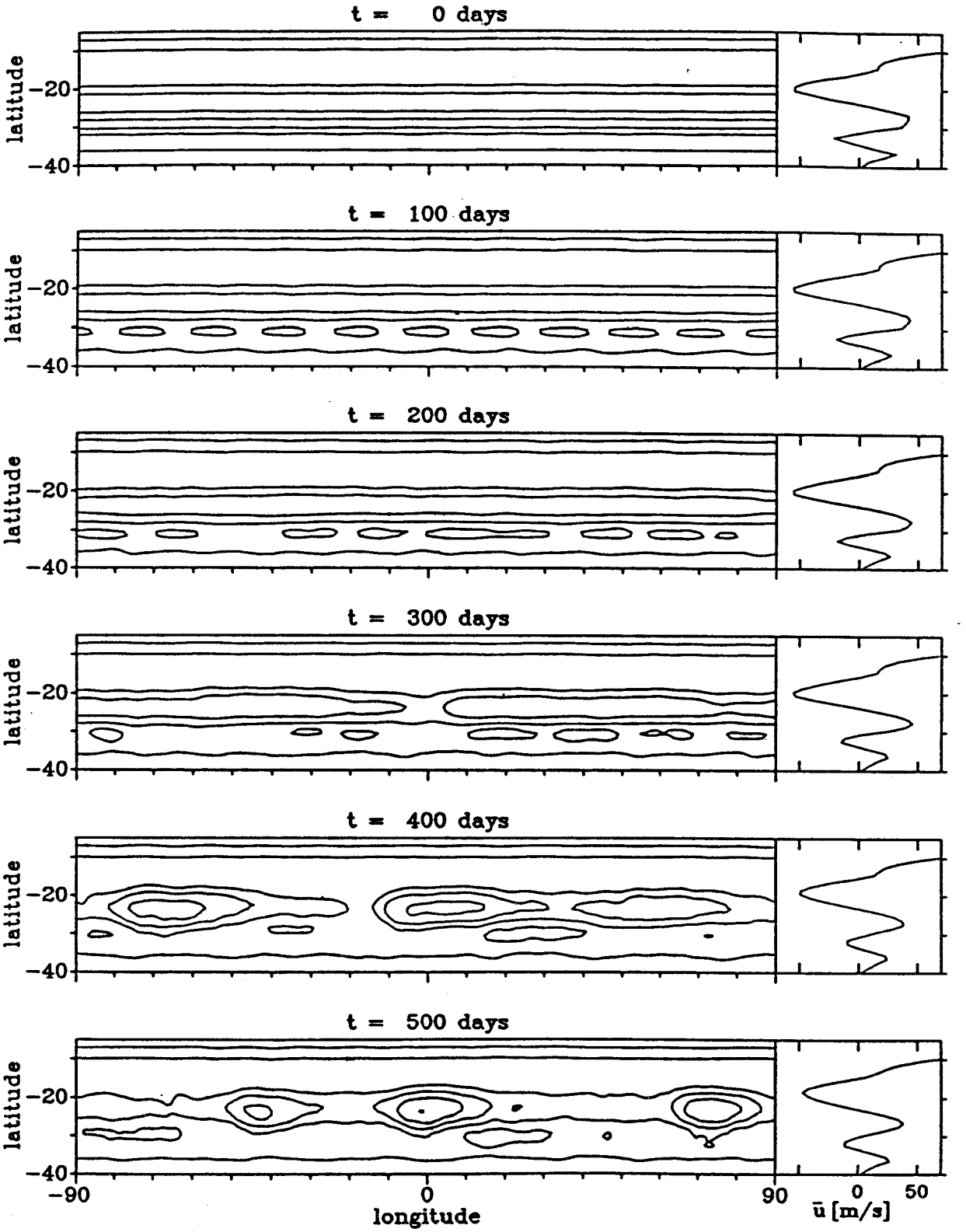
t = 0 days
t = 100 days
t = 200 days
t = 300 days
t = 400 days
t = 500 days
latitude
-20
-40
-90
0
90
longitude
0
50
ū [m/s]

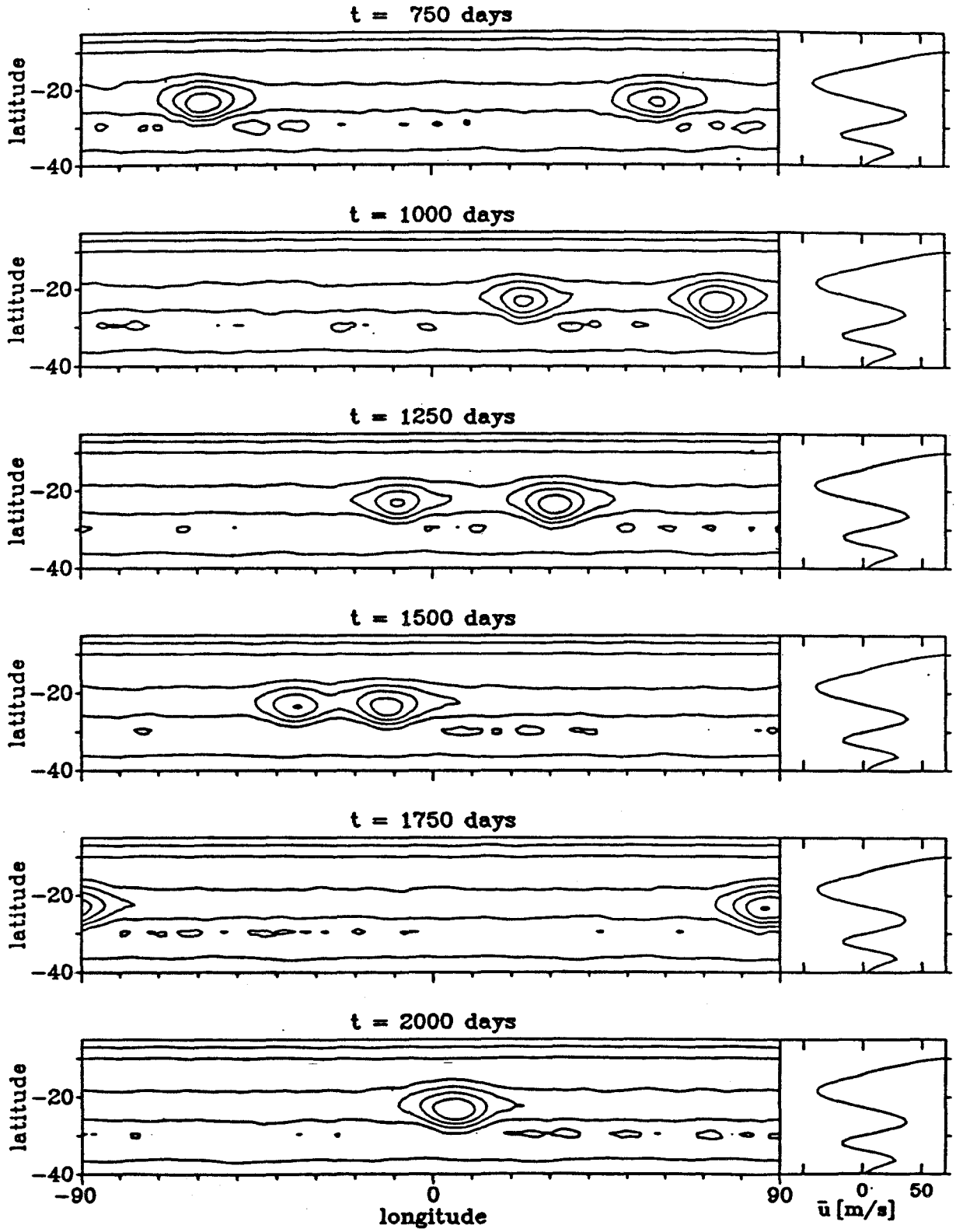
t = 750 days
t = 1000 days
t = 1250 days
t = 1500 days
t = 1750 days
t = 2000 days
latitude
-20
-40
-90
0
90
longitude
0
50
ū [m/s]

In Fig. 2.17 we show the results of a vortex genesis experiment. The initial state is constructed by adding a small sinusoidal perturbation of ten wavelengths over the longitudes $-90°$ to $90°$, in a $\mathrm{sech}^2(\phi/90°)\sin^{1/2}(-\pi(\lambda+5°)/35°)$ envelope, to the free-surface height $g(h+h_2)$, calculated from the cloud-top, zonal-wind profile (Fig. 2.4), followed by geostrophic initialization of the velocity field. This envelope brings the perturbation of the northward velocity v to zero at the northern and southern boundaries ($\lambda = -5°$, $-40°$), and adds a slight height difference in longitude to the initial ten waves. The parameters q_0 and τ are as in Fig. 2.9. The peak initial perturbation velocity is $1.6\,\mathrm{m\,s^{-1}}$, compared to the $54\,\mathrm{m\,s^{-1}}$ peak initial zonal wind. By $t = 100$ days, the disturbance is noticeable in the $g(h+h_2)$ field. By $t = 300$ days the initial perturbation has started an instability in the GRS shear flow, which by $t = 500$ days has resolved into three large, distinct vortices. By $t = 750$ days, two of these vortices have merged, and by $t = 1600$ days, only one large vortex remains. This vortex is run through $t = 2000$ days. Notice that even though the initial conditions are vastly different between the run shown here and the run shown in Fig. 2.16, the final forms are quite similar. We also get the formation of a single large vortex in the shear zone of the GRS if we don't force the zonal flow ($\tau = \infty$), or if we use random noise instead of a sinusoidal perturbation to trigger the instability.

We have demonstrated in this section that the existence of a single, large GRS-like vortex on Jupiter follows naturally from the observed, cloud-top winds and derived, deep atmospheric motions. If the cloud-top winds are kept in an unstable state, the large vortex can be maintained indefinitely against dissipation. This scenario applies to the DI89 and WY84 models, and should be true in general for any other model with an unstable upper-layer zonal-velocity profile.

2.6 Conclusions

We have modeled Jupiter's Great Red Spot (GRS) and deep atmosphere as a 1-1/2 layer shallow water (SW) system. We assume that the deep motions are zonally symmetric and steady, and that the Jovian vortices and time-dependent dynamics are confined to a thin, upper weather layer. The dynamical effects of the deep zonal motions on the upper layer are represented by meridionally varying bottom topography underneath the upper layer. Most current models of the GRS prescribe this bottom topography, based on assumptions about the deep atmosphere. In this work, we *derive* the bottom topography from the high-resolution, cloud-top velocity data for the GRS and White Oval BC, up to a single free parameter, which depends on the unknown radius of deformation. In the process we calculate the Bernoulli streamfunction B, and determine the potential vorticity q as a function of B.

Our results show that there is differential fluid motion in the deep atmosphere below the vortices. In this sense the models of Williams and Yamagata (1984) and Williams and Wilson (1988), which prescribe solid-body motions for the deep atmosphere, are too simple. The derived deep winds do not correspond exactly with the zonally-averaged, cloud- top winds. In this sense the model of Ingersoll and Cuong (1981), which prescribes the deep winds to be equivalent to the far-field winds in the upper layer, is overspecified. The derived far-field potential vorticity is found not to be constant. In this sense the model of Marcus (1988), which prescibes uniform far-field potential vorticity, is also overspecified.

Since we determine the B field and the functions $q(B)$ for the GRS and Oval BC, we are able to examine the potential vorticity fields associated with these vortices. Both vortices represent minimum $|q|$ anomalies, and both show q to be relatively constant inside their closed-streamline regions. The latter observation is consistent with the work of Rhines and Young (1982) on potential vorticity homogenization

inside closed streamline regions.

The filamentary region to the northwest of the GRS has yet to be modeled successfully. We expect that the deep motions must be accurately represented in order to model such a feature. Convective activity may also play a role in filamentary regions. Convection, were it possible in a SW model, might correspond to negative upper-layer thickness. Our results show that the upper layer is thinnest in the latitude range of the GRS's filamentary region, and that the cloud-top winds decay rapidly there with depth.

Using numerical simulations, we have studied the time-dependent behavior of the shallow water, 1-1/2 layer analog of Jupiter's atmosphere. We initialize the upper layer with the observed, zonally-averaged, cloud-top velocity profile. In the first class of numerical experiments, we compare the effect of the derived bottom topography to the bottom topographies prescribed by current models. Each of these models is successful in maintaining a long-lived, isolated vortex, but only the present model, which is based on observations, yields $(\zeta + f)$ profiles along streamlines that agree with those observed for the GRS by Dowling and Ingersoll (1988).

In the second class of numerical experiments, we study the longevity and genesis of a GRS-like vortex, using the observed cloud-top winds and the derived bottom topography. In this simulation small eddies form in the shear zone associated with the GRS. Such instability is consistent with the local extrema observed in the far-field potential vorticity profile for this model. If the upper-layer, eastward velocity u is forced towards the observed profile u_J, the instability is maintained and small eddies appear continuously. These eddies coalesce over a time scale of years into a single, large vortex, which resembles the GRS. This large vortex persists indefinitely against dissipation by absorbing the constant supply of smaller eddies.

We propose that the dual problems of genesis of the GRS and maintenance of that

vortex against dissipation can be solved by finding a mechanism that maintains the observed, zonally-averaged, cloud-top velocity profile and the derived deep motions. Williams and Wilson (1988) arrived at the same conclusion for the case of solid-body deep motions. Both the DI89 and WW88 models have an unstable zonally-averaged upper-layer velocity profile, which is the necessary component for the genesis and maintenance against dissipation of vortices in these models. This does not rule out an additional role in Jupiter's atmosphere for eddies produced by convection. Such eddies might be a source of energy to both the unstable zonal flow and the large vortices.

We have emphasized a 1-1/2 layer interpretation of the data because such a model contains the minimum amount of complexity to explain the observations, and because most current models of the GRS are cast in terms of such a model. In this model the observed variation of $(\zeta + f)$ along streamlines, i.e., the observed vortex-tube stretching, is accounted for by deep zonal motions underneath the vortices. Other sources of vortex-tube stretching are possible. If the Jovian troposphere and its vortices are modeled with two or more layers instead of just one weather layer, it is conceivable that $(\zeta + f)$ variations may arise because of vortex-tube stretching which occurs locally near the cloud-top level, instead of being distributed over the entire weather layer. Nevertheless, any such alternate model of the GRS must be able to reproduce the observed Lagrangian $(\zeta + f)$ profiles, and hence account for the vortex-tube stretching occurring in the cloud-top flow. The DI89 model, since it is based on observations, is the first to pass this test.

Acknowledgements. The numerical experiments in this paper were done on the San Diego Supercomputer Center's Cray X-MP/48 computer. This research was supported by the Planetary Atmospheres Program of NASA and by *Voyager* Project funds.

2.7 References

Achterberg, R. K. and A. P. Ingersoll, 1989. A normal-mode approach to Jovian atmospheric dynamics. Submitted to *J. Atmos. Sci.*.

Allison, M. D., and P. J. Gierasch, 1982. Jovian atmospheric dynamics: Global-scale motion and shear instability for a thin, nearly adiabatic upper weather layer. *Bull. Amer. Astron. Soc.* **14**, 722.

Arakawa, A., and V. R. Lamb, 1981. A potential enstrophy and energy conserving scheme for the shallow water equations. *Mon. Wea. Rev.* **109**, 18–36.

Dowling, T. E. and A. P. Ingersoll, 1988. Potential vorticity and layer thickness variations in the flow around Jupiter's Great Red Spot and White Oval BC. *J. Atmos. Sci.* **45**, 1380–1396.

Flasar, F. M., B. J. Conrath, J. A. Pirraglia, P. C. Clark, R. G. French, and P. J. Gierasch, 1981. Thermal structure and dynamics of the Jovian atmosphere. 1. The Great Red Spot. *J. Geophys. Res.* **86**, 8759–8767.

Flasar, F. M., 1986. Global dynamics and thermal structure of Jupiter's atmosphere. *Icarus* **65**, 280–303.

Flasar, F. M. and P. J. Gierasch, 1986. Mesoscale waves as a probe of Jupiter's deep atmosphere. *J. Atmos. Sci.* **43**, 2683–2707.

Gill, A. E., 1982. *Atmosphere-Ocean Dynamics.* Academic Press, New York.

Haltiner, G. J., and R. T. Williams, 1980. *Numerical Prediction and Dynamic Meteorology.* Wiley and Sons, New York.

Ingersoll, A. P., 1988. Models of Jovian vortices. *Nature* **331**, 654–655.

Ingersoll, A. P., R. F. Beebe, S. A. Collins, G. E. Hunt, J. L. Mitchell, P. Muller, B. A. Smith, and R. J. Terrile, 1979. Zonal velocity and texture in the Jovian atmosphere inferred from Voyager images. *Nature* 280, 773–775.

Ingersoll, A. P., R. F. Beebe, B. J. Conrath and G. E. Hunt, 1984. Structure and

dynamics of Saturn's atmosphere. In *Saturn* (T. Gehrels and M. S. Matthews, eds.) pp. 195–238. University of Arizona Press, Tucson.

Ingersoll, A. P. and P. G. Cuong, 1981. Numerical model of long-lived Jovian vortices. *J. Atmos. Sci.* **38**, 2067–2076.

Limaye, S. S., 1986. Jupiter: new estimates of the mean zonal flow at the cloud level. *Icarus* **65**, 335–352.

Mac Low, M.-M., and A. P. Ingersoll, 1986. Merging of vortices in the atmosphere of Jupiter: An analysis of Voyager images. *Icarus* **65**, 353-369.

Marcus, P. S., 1988. A numerical simulation of the Great Red Spot of Jupiter. *Nature* **331**, 693–696.

Mitchell, J. L., R. F. Beebe, A. P. Ingersoll and G.W. Garneau, 1981. Flow fields within Jupiter's Great Red Spot and White Oval BC. *J. Geophys. Res.* **86**, 8751–8757.

Pedlosky, J., 1987. *Geophysical Fluid Dynamics, Second Edition.* Springer-Verlag, New York.

Read, P. L., 1985. Finite-amplitude, neutral baroclinic eddies and mean flows in an internally heated rotating fluid: 1. Numerical simulations and quasi-geostrophic 'free modes.' *Dyn. Atmos. Oceans* **9**, 135– 207.

Read, P. L., 1986. Stable, baroclinic eddies on Jupiter and Saturn: A laboratory analog and some observational tests. *Icarus* **65**, 304-334.

Read, P. L. and R. Hide, 1983. Long-lived eddies in the laboratory and in the atmospheres of Jupiter and Saturn. *Nature* **302**, 126– 129.

Read, P. L. and R. Hide, 1984. An isolated baroclinic eddy as a laboratory analogue of the Great Red Spot on Jupiter? *Nature* **308**, 45–49.

Rhines, P. B. and W. R. Young, 1982. Homogenization of potential vorticity in planetary gyres. *J. Fluid Mech.* **122**, 347–367.

Ripa, P., 1983. General stability conditions for zonal flows in a one-layer model on the β-plane or the sphere. *J. Fluid Mech.* **126**, 463-489.

Smith, B. A., L. A. Soderblom, T. V. Johnson, A. P. Ingersoll, S. A. Collins, E. M. Shoemaker, G. E. Hunt, H. Masursky, M. H. Carr, M. E. Davies, A. F. Cook II, J. Boyce, G. E. Danielson, T. Owen, C. Sagan, R. F. Beebe, J. Veverka, R. G. Strom, J. F. McCauley, D. Morrison, G. A. Briggs, and V. E. Suomi, 1979a. The Jupiter system through the eyes of Voyager 1. *Science* **204**, 951–972.

Smith, B. A., R. Beebe, J. Boyce, G. Briggs, M. Carr, S. A. Collins, A. F. Cook II, G. E. Danielson, M. E. Davies, G. E. Hunt, A. P. Ingersoll, T. V. Johnson, H. Masursky, J. McCauley, D. Morrison, T. Owen, C. Sagan, E. M. Shoemaker, R. Strom, V. E. Suomi, and J. Veverka, 1979b. The Galilean satellites and Jupiter: Voyager 2 imaging science results. *Science* **206**, 927–950.

Stevenson, D. J., 1982. Interiors of the giant planets. *Ann. Rev. Earth Planet. Sci.* **10**, 257–295.

Williams, G. P. and R. J. Wilson, 1988. The stability and genesis of Rossby vortices. *J. Atmos. Sci.* **45**, 207–241.

Williams, G. P. and T. Yamagata, 1984. Geostrophic regimes, intermediate solitary vortices and Jovian eddies. *J. Atmos. Sci.* **41**, 453- -478.